Topographical mapping of isoform-selectivity determinants for J-channel-binding inhibitors of sphingosine kinases 1 and 2

David R. Adams,[‡] Salha Tawati,[†] Giacomo Berretta,[†] Paula Lopez Rivas,[†] Jessica Baiget,[†] Zhong Jiang,[‡] Aisha Alsfouk,[†] Simon P. Mackay,[†] Nigel J. Pyne,[†] and Susan Pyne,[*,†]

[†]Strathclyde Institute of Pharmacy and Biomedical Sciences, University of Strathclyde, Glasgow G4 0RE, UK

[‡]School of Engineering & Physical Sciences, Heriot-Watt University, Edinburgh EH14 4AS, UK

ABSTRACT

Sphingosine kinase enzymes (SK1 and SK2) catalyse the conversion of sphingosine into sphingosine 1-phosphate and play a key role in lipid signaling and cellular responses. Mapping of isoform amino acid sequence differences for SK2 onto the recently available crystal structures of SK1 suggests that subtle structural differences exist in the foot of the lipid-binding 'J-channel' in SK2, the structure of which has yet to be defined by structural biology techniques. We have probed these isoform differences with a ligand series derived from the potent SK1-selective inhibitor, PF-543. Here we show how it is possible, even with relatively conservative changes in compound structure, to systematically tune the activity profile of a ligand from *ca*. 100-fold SK1-selective inhibition, through equipotent SK1/SK2 inhibition, to reversed 100-fold SK2 selectivity, with retention of nanomolar potency.

INTRODUCTION

Sphingosine 1-phosphate (S1P) is a key signalling lipid derived from sphingosine (Sph) by the action of sphingosine kinases (SK1 and SK2). S1P is transported to the extracellular environment, where it functions as a ligand for a family of five S1P-specific G protein coupled receptors ($S1P_{1-5}$), but it also acts on specific intracellular target proteins, such as histone deacetylases 1/2 (HDAC1/2).[1, 2] Irreversible cleavage of S1P is catalysed by S1P lyase, producing (*E*)-2-hexadecenal and phosphoethanolamine,[3] but S1P is also reversibly dephosphorylated by S1P phosphatase to regenerate Sph,[4-6] levels of which are additionally influenced by flux through the ceramide (Cer) synthesis pathway.[7] The effects of S1P on cell function favour proliferation, migration, differentiation and survival and are generally opposed by Cer, which induces apoptosis, senescence and growth arrest.[8, 9] As a consequence the concept of the 'sphingolipid rheostat' was proposed,[10, 11] in which the inter-conversion of Cer *via* Sph to S1P controls cellular fate (recently reviewed[12, 13]). Altered S1P signalling has been associated with numerous pathophysiologies, including cancer, cardiovascular disease, neurodegenerative conditions, diabetes and inflammatory disease.[14] The possibility of manipulating the sphingolipid rheostat for therapeutic purposes has therefore provided a rationale for exploring the development of SK inhibitors and their potential to reduce S1P formation and signalling and to raise pro-apoptotic Cer levels.

The SK1 and SK2 enzymes are encoded by distinct genes and differ in their subcellular localisation, biochemical properties and functions; there are three N-terminal variants of SK1 and two N-terminal variants of SK2.[15, 16] A number of classes of SK inhibitors have emerged in the last two decades, including the recent discovery of an ATP-competitive SK inhibitor chemotype that decreases cellular S1P levels, elevates Sph/Cer, induces apoptosis, and that inhibits cell proliferation and colony formation.[17] Most work to date, however, has focused on the development

of Sph-competitive inhibitors. This includes the development of inhibitors selective for SK1 that exhibit nanomolar potency, such as PF-543 (**1**),[18] Genzyme-51 (**2**)[19] and Amgen-23 (**3**),[20] Chart 1. PF-543 reduces sickling of red blood cells[21] *in vitro* and *in vivo* and attenuates post-infarction cardiac remodeling.[22] We have also demonstrated[23] that PF-543 protects against cardiomyocyte apoptosis and reduces cardiac maladaptive hypertrophy in a mouse model of pulmonary hypertension.

Chart 1. Lipid substrate (Sph), product (S1P) and established inhibitors for SK1 and SK2.

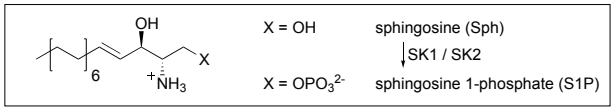

		K_i (IC_{50}) / nM [a]	
		SK1	SK2
SK1-selective inhibitors			
1 PF-543 [d]	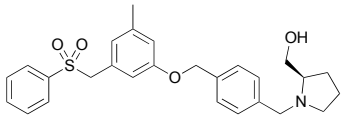	(28) [b]	(>5,000) [b]
2 Genzyme-51	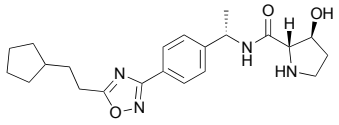	(58)	ND [c]
3 Amgen-23 [d]	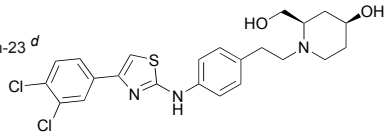	(20)	(1,600)
SK2-selective inhibitors			
4 ABC294640	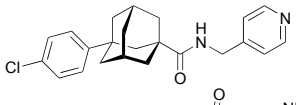	no inhibition at 100 μM	9,800
5 K145	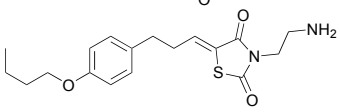	no inhibition at 10 μM	6,400
6 SLR080811	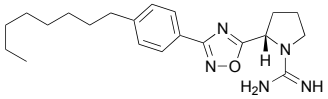	12,000	1,300
7 ROMe	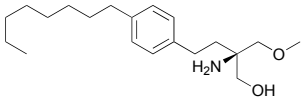	no inhibition at 100 μM	16,000
8 Pfizer-27c	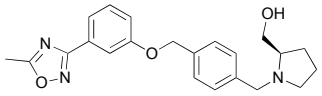	(25)	(2.4)
9 VT-20dd	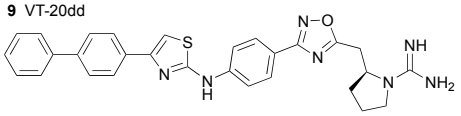	9,000	90
Other inhibitors			
10 SKi [d]	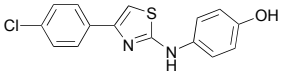	16,000	6,700

[a]For references see text. [b]This study. [c]No data. [d]Co-crystal structure available with SK1.

Early prototype Sph-competitive SK2-selective inhibitors include ABC294640 (**4**),[24] K145 (**5**),[25] SLR0808110 (**6**)[26] and (*R*)-FTY720 methyl ether (ROMe; **7**),[27] Chart 1. Of these compounds, ABC294640, which induces cell death *via* apoptotic and autophagic pathways,[24,28] has been tested in several disease models for cancer,[24] rheumatoid arthritis[29] and ulcerative colitis.[30] The compound has proceeded to phase I/II clinical studies targeting multiple oncology and inflammatory indications. However, ABC294640 also indirectly targets dihydroceramide desaturase and induces the proteasomal degradation of SK1 in prostate cancer cells and in HEK293T cells.[31-33] ROMe, an SK2-selective inhibitor (K_i 14 μM) with no activity against SK1 at 100 μM, inhibits DNA synthesis in breast cancer cells and induces autophagic death of T-cell acute lymphoblastic leukemic cells.[27, 34] Very recently two reports have disclosed examples of more potent SK inhibitors, Pfizer-27c (**8**)[35] and VT-20dd (**9**),[36] with selectivity for SK2. Despite these developments and a growing interest in the (patho)physiological roles of SK2, a clear structural rationale for the development of high potency SK2-specific inhibitors has yet to emerge.

No SK2 crystal structures are available as yet to support structure-based design of SK2-selective inhibitors, but amino acid sequence alignment suggests a high degree of homology to SK1, the structure of which has recently been solved by X-ray crystallography.[37,20,38] SK1 exhibits a bidomain architecture comprising an ATP-binding N-terminal domain (NTD) and a C-terminal domain (CTD) that hosts the Sph binding site, Figure 1. The CTD folds as a two-layer β-sandwich with three extended inter-strand loops packing across one face to generate the Sph binding site as a J-shaped cavity, termed the 'J-channel'. One of the three 'lipid binding loops', LBL-1, consists of two reverse-paired helices (α7 and α8) that may gate substrate entry and product egress by a hinged motion.[39] Residues in LBL-1 and in the second loop, LBL-2, define much of the contact surface for the polar head group and central region of the lipid. The third loop, LBL-3, folds with

an additional helix (α9), running antiparallel along α8, and provides enclosure for the lipid tail. To date, SK1 co-crystal structures have been acquired with three inhibitors bound in the J-channel, namely with SKi (**10**; also known as SKI-II),[37] with Amgen-23 (**3**),[20] and most recently with PF-543 (**1**).[38] We have used the latter structure as a starting point to explore differences in the foot of the J-channel of SK1 and SK2. Here we report our results from a ligand-based structure activity relationship (SAR) study that highlights key determinants for switching between SK1-selective and SK2-selective inhibition.

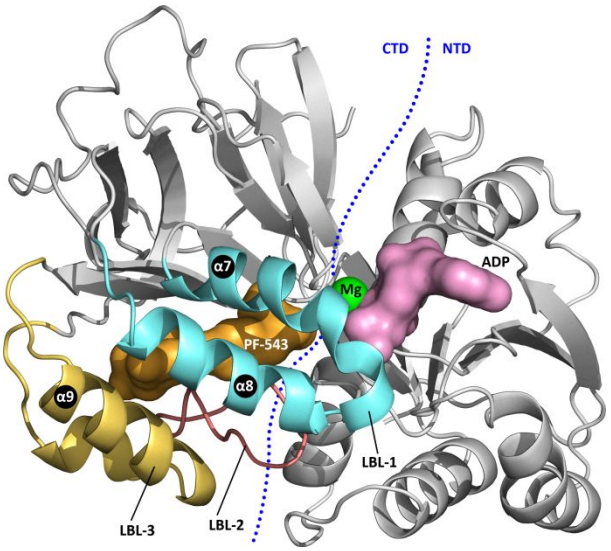

Figure 1. The structure of SK1 is shown with bound PF-543 (**1**; orange surface) (PDB: 4V24).[38] PF-543 occupies the substrate Sph binding site, formed by the packing of three lipid binding loops (LBL-1 to LBL-3) against a β -sandwich core. The nucleotide binding site is shown by superimposition of Mg-ADP (green sphere/rose surface) from its separate co-crystal structure (3VZD) with SK1.[37]

RESULTS AND DISCUSSION

Design rationale for ligand selectivity switching. Of the 20 or so residues that contribute to the J-channel in SK1, SK2 differs at only 3 points in the direct hydrophobic contact surface of the binding site—namely in Ile174, Met272 and Phe288 of SK1, corresponding respectively to Val304, Leu517 and Cys533 in SK2 (Figure 2, orange). Phe288 stoppers the toe of the SK1 J-channel, and its substitution by Cys533 in SK2 may result in a longer J-channel and potentially also confer greater surface plasticity in that region of SK2 due to loosened packing against adjacent hydrophobic residues. Ile174 and Met272 contribute to the throat of the J-channel and, in the SK1/PF-543 co-crystal structure, are seen to form part of the flanking surface on either side of the inhibitor's *p*-xylylene subunit; their replacement by Val and Leu may make this region of the J-channel slightly wider in SK2 than in SK1. Ile174 additionally contributes surface on one edge of the PF-543 terminal subunit, with contact distances of 3.6 and 3.4 Å between its Cδ methyl carbon and the PF-543 phenyl *ortho* and *meta* carbons respectively. A leucine (Leu261; Figure 2, yellow), that is packed against Ile174 in SK1, also contributes to the contact surface around the edge of the PF-543 terminal phenyl and, although conserved in SK2 (as Leu506), may differ in its conformational profile due to the replacement of the adjacent Ile174 in SK1 by Val304 in SK2. Together, these considerations suggest that the J-channel toe might be expanded in SK2 on a contact surface mapping to the *para*-position of the terminal phenyl of SK1-bound PF-543 (Figure 2, green arrow).

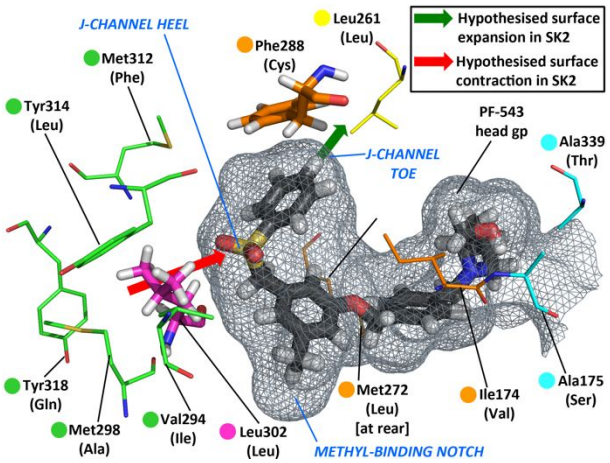

Figure 2. J-channel surface detail (mesh) from the PF-543/SK1 co-crystal (PDB: 4V24),[38] highlighting key isoform residue differences that likely impact on the J-channel structure of SK2. SK1 residue numbering is shown; cognate SK2 residues, where different, are in parenthesis. (Residue color notation: see text.)

In principle, an expanded surface in SK2 at the J-channel toe might contribute to reduced affinity for PF-543 and hence, at least in part, to the established SK1-over-SK2 selectivity of this inhibitor (Chart 1). However, SK2 also differs from SK1 in several other residues that, whilst not contributing directly to the ligand contact surface, are likely to indirectly affect the J-channel structure. Thus, a set of residues in LBL-3 of SK1 (Val294, Met298, Met312, Tyr314, Tyr318; Figure 2, green) differs in SK2 (as Ile539, Ala543, Phe557, Leu559 and Gln563 respectively). Inspection of the SK1/PF-543 co-crystal structure suggests that these differences may impact on the conformation of a conserved leucine (Leu302 in SK1; Figure 2, magenta), which contributes to the contact surface for the sulfonyl group of PF-543. We hypothesized that the cognate residue (Leu547) in SK2 might be driven inwards to narrow the J-channel at that point. If so, surface encroachment in the J-channel heel of SK2 might then interdict comfortable accommodation of

the sulfonyl oxygens of PF-543 and also contribute to the observed SK1-selectivity of this inhibitor.

Two further residue differences, Ala175 and Ala339 in SK1 (corresponding to Ser305 and Thr584 in SK2), might also potentially be relevant to isoform discrimination by ligands targeting the J-channel. These residues (Figure 2, cyan) lie proximal to the 2-(hydroxymethyl)pyrrolidine 'head group' of PF-543, and their variation in SK2 might affect a network of polar interactions that engages the PF-543 head group or/and slightly reposition LBL-1 with respect to the β-sandwich core, which could then impact on the surface of a notch in the J-channel that accommodates the PF-543 methyl group (Figure 2). However, it is known[38] that the hydroxyl group of SK1-bound PF-543 precisely maps to the position of the Sph-3-OH and, given that Sph serves as a substrate for *both* SK1 and SK2, it is likely that the 'head group' hydrogen bonding features in SK2 should also support the binding of the PF-543 2-(hydroxymethyl)pyrrolidine subunit. Thus, in seeking to identify determinants for SK2-selective inhibition, we focused attention on a series of PF-543 analogues that retained the 2-(hydroxymethyl)pyrrolidine head group but embodied alterations to the tail targeted to the enclosed J-channel foot, predicted by our analysis to offer scope for isoform-discriminating interactions with ligands. Accordingly, we prepared a concise compound test set to evaluate whether SK2-inhibitory activity might be enhanced by alleviating steric demand in the sulfonyl linker and/or by deletion of the PF-543 methyl group. We also sought to test the hypothesis that optimisation of ligand fit to the J-channel toe in SK2 might confer selectivity over SK1.

Synthesis of probe compound set. In order to assess the contribution of the methyl group to the SK1 selectivity of PF-543, we prepared the normethyl analogue (**18**; Scheme 1) for evaluation. The compound was prepared from *m*-methoxybenzyl bromide (**11**) by reaction with

sodium benzenesulfinate followed by boron tribromide mediated cleavage of the aryl methyl ether in **12** to afford phenol **14**. The latter was then alkylated with 4-(bromomethyl)benzaldehyde and the resulting aldehyde (**16**) subjected to reductive amination with (*R*)-(–)-prolinol.

Scheme 1. Synthesis of probe compounds 18 and 19.[a]

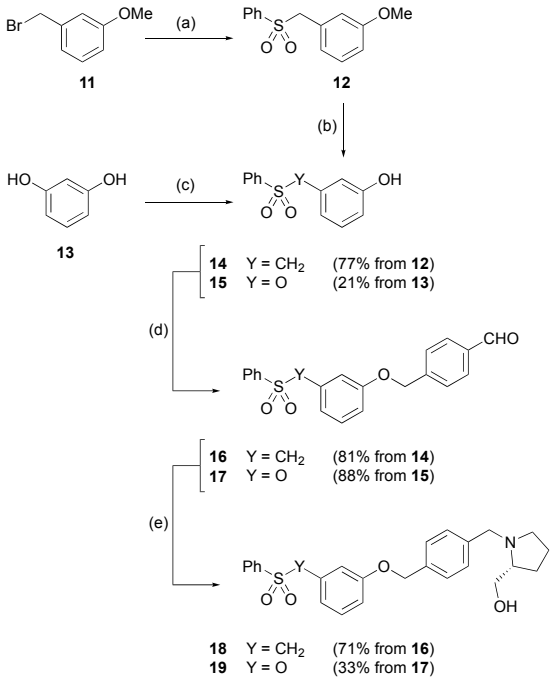

[a]Reagents and conditions: (a) $NaSO_2Ph$, Aliquat® 336, 85 °C (47%); (b) BBr_3, CH_2Cl_2, –78 °C (77%); (c) phenylsulfonyl chloride K_2CO_3 / MeCN (21%); (d) 4-(bromomethyl)benzaldehyde, K_2CO_3, MeCN, 60 °C; (e) (*R*)-2-(hydroxymethyl)pyrrolidine, $NaBH(OAc)_3$, DCE.

A collection of compounds was then prepared in order to evaluate the contribution of the $–SO_2-CH_2–$ tail linker to inhibitory performance and selectivity. Analogues were designed to test the impact of replacing the PF-543 sulfonyl group by methylene, but we also included an isosteric sulfonate (**19**) to probe the impact of subtle changes in ligand bond angle preferences. Sulfonate **19** was prepared by initial sulfonylation of resorcinol (**13**) followed by alkylation of the resulting

phenol (**15**) with 4-(bromomethyl)benzaldehyde and reductive amination with (*R*)-(–)-prolinol, Scheme 1.

The ethylene-linked analogue (**23**, Scheme 2) was prepared to assess the impact of reducing steric demand in the locus occupied by the PF-543 sulfonyl group. For reasons of synthetic convenience, this and other sulfonyl deletion analogues were prepared for comparative evaluation against **18** without the methyl group in place on the central arene ring. Synthesis of **23** was undertaken from acetylene **20**, prepared by ambient temperature Sonogashira coupling of 3-iodophenol[40] with phenylacetylene. The acetylene was hydrogenated to afford phenol **21**, which was alkylated with 4-(bromomethyl)benzaldehyde to afford **22**. Reductive amination of the latter with (*R*)-(–)-prolinol afforded **23**.

Scheme 2. Synthesis of probe compound 23.[a]

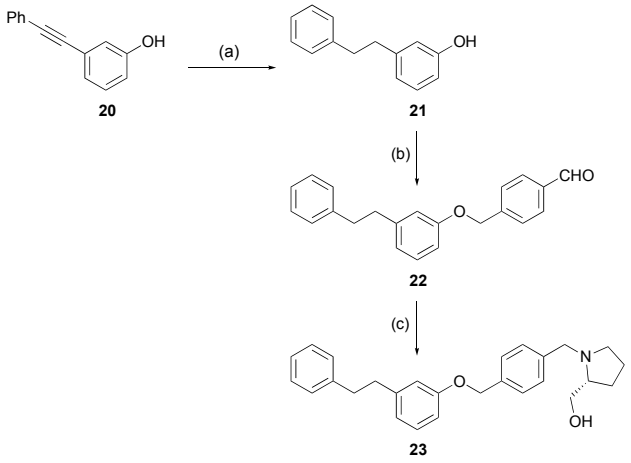

[a]Reagents and conditions: (a) H_2, Pd/C, EtOH (95%); (b) 4-(bromomethyl)benzaldehyde, K_2CO_3, MeCN, 20 °C, 16 h (87%); (c) (*R*)-2-(hydroxymethyl)pyrrolidine, $NaBH(OAc)_3$, DCE (82%).

An ether-linked variant (**49**) of **23** was prepared according to Scheme 3. Thus, resorcinol (**13**) was alkylated with benzyl bromide and the resulting phenol (**25**) transformed into **49** by the

two-step alkylation/reductive amination procedure applied in Schemes 1 and 2 for compounds **18**, **19** and **23**. A subset of six halogenated analogues (**50**–**55**, Scheme 3) was then expanded to facilitate systematic exploration of the space in the J-channel foot. Two further analogues were included in the ether-linked test set to explore the impact of steric demand in the critical toe region of the J-channel—namely, methyl ether **56** and nitrile **57**, with bent and linear two-atom extensions from the *para*-position of the tail arene. The sulfide counterpart (**58**) of the ether-linked parent (**49**) was prepared in a similar manner starting from benzenethiol (**24**). The *para*-fluorophenyl and *para*-chlorophenyl analogues (**59** and **60**) of this latter compound were made by a similar strategy. Sulfides **58**–**60** were included to test the impact of incorporating a heteroatom in the linker with greater steric demand and differing bond angle preferences, which might impact on positioning of the ligand's terminal *para*-site in the critical J-channel toe region.

Scheme 3. Synthesis of probe compounds 49–60.[a]

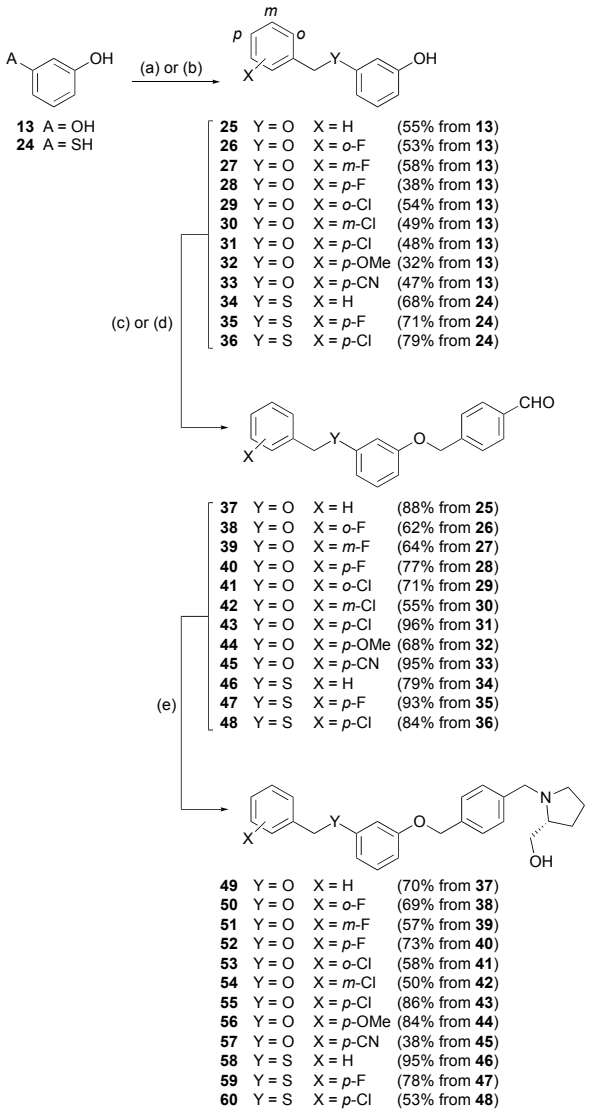

[a]Reagents and conditions: (a) **25**–**33**: (substituted)benzyl bromide (or 4-chlorobenzyl chloride in the case of **31**), K_2CO_3, acetone, 65 °C, 5 h; (b) **34**–**36**: (substituted)benzyl bromide (or 4-chlorobenzyl chloride in the case of **36**), K_2CO_3, MeCN, 20 °C, 16 h; (c) **37**–**45**: NaH, DMF, then 4-(bromomethyl)benzaldehyde, 16 h, 20 °C; (d) **46**–**48**: 4-(bromomethyl)benzaldehyde, K_2CO_3, MeCN, 20 °C, 16 h; (e) (*R*)-2-(hydroxymethyl)pyrrolidine, $NaBH(OAc)_3$, THF (for **49**–**57**) or DCE (for **48**–**60**).

SK-inhibitory performance and selectivity of probe compound set. Compounds were evaluated for inhibition of purified SK1 and SK2 using a radiometric assay, as detailed in our earlier work.[41] In brief, the procedure uses [γ -^{32}P]ATP and measures incorporation of the radiolabelled phosphate into the S1P product. SK1 and SK2 were assayed, respectively, at 3 and 10 μM Sph substrate concentration. These concentrations correspond to the K_m values of SK1[42-44] and SK2[27] and, therefore, allow direct comparison of the sensitivity of the two enzymes at 50% saturation with Sph. Assays were performed with ATP at 250 μM concentration, well above the K_m value for the nucleotide, to ensure saturation with ATP. Activity data are summarised in Chart 2.

Chart 2. SK1 and SK2 inhibitory activity for probe compound set derived from PF-543 (1).[a]

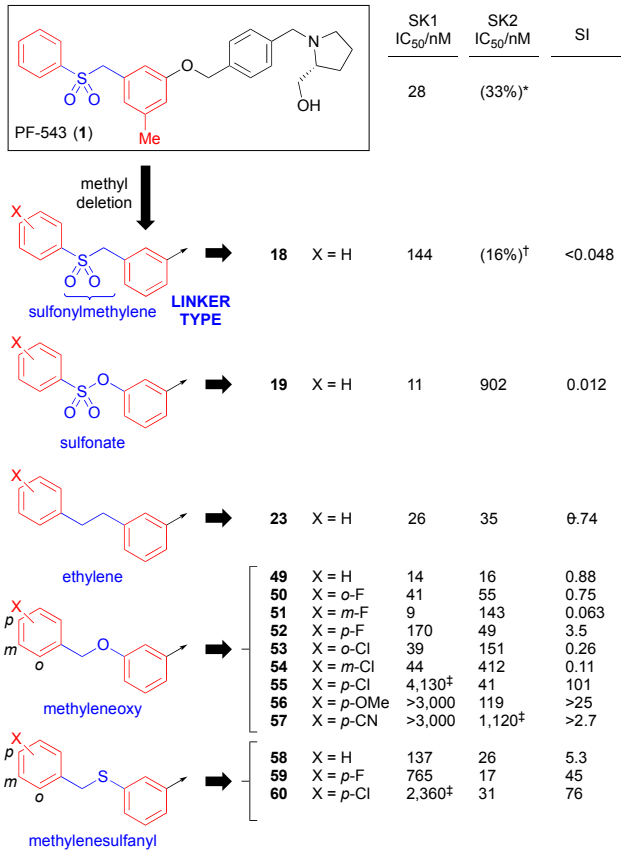

		SK1 IC_{50}/nM	SK2 IC_{50}/nM	SI
PF-543 (**1**)		28	(33%)*	
18	X = H	144	(16%)†	<0.048
19	X = H	11	902	0.012
23	X = H	26	35	0.74
49	X = H	14	16	0.88
50	X = *o*-F	41	55	0.75
51	X = *m*-F	9	143	0.063
52	X = *p*-F	170	49	3.5
53	X = *o*-Cl	39	151	0.26
54	X = *m*-Cl	44	412	0.11
55	X = *p*-Cl	4,130‡	41	101
56	X = *p*-OMe	>3,000	119	>25
57	X = *p*-CN	>3,000	1,120‡	>2.7
58	X = H	137	26	5.3
59	X = *p*-F	765	17	45
60	X = *p*-Cl	2,360‡	31	76

* % enzyme inhibition at 5 μM test concentration

† % enzyme inhibition at 3 μM test concentration

‡ Estimated IC_{50} from partial concentration response curve (1 nM – 3 μM range)

[a] SK1 activity was assayed using 3 μM Sph and 250 μM ATP. SK2 activity was assayed using 10 μM Sph and 250 μM ATP. Data are reported as IC_{50} values (or % enzyme inhibition) *vs* control determined in triplicate assays. NE: no inhibitory effect at maximal test concentration of 3 μM. SI denotes selectivity index as IC_{50} (SK1) / IC_{50} (SK2).

We have previously obtained[41] an IC_{50} of 28 nM for inhibition of SK1 by PF-543 in our assay, considerably higher than the K_i value of 3.6 nM reported by Schnute *et al.*[18], with the caveat that the latter determination was performed under conditions where ATP was not saturating and

therefore subject to two-substrate kinetics. As reported, however, PF-543 was highly selective for inhibition of SK1, giving only 33% inhibition of SK2 at 5 μM and 72% at 50 μM.

Our analysis (*vide supra*) suggested that the most likely explanation for the SK1-over-SK2 selectivity of PF-543 is due to surface encroachment in the SK2 J-channel heel targeted by the inhibitor's sulfonyl group (Figure 2, red arrow). However, at the outset of our studies we could not eliminate the possibility that structural differences in the sub-pocket that accommodates the PF-543 methyl group (Figure 2, 'notch') might also be a contributory factor. We therefore evaluated the normethyl analogue (**18**) of PF-543. This compound showed a modest (5-fold) loss in SK1-inhibitory potency compared to PF-543, consistent with a slight reduction in favourable surface contact with that isoform. However, the gain in SK2 inhibition that might have been expected for relief of an unfavourable surface compression against the methyl, was not observed. Indeed, only slight inhibition of SK2 (16%) was detectable at the maximal test concentration of 3 μM in our current studies, suggesting that the PF-543 methyl group is not a strong determinant of selectivity. During the course of our studies Schnute *et al*. disclosed[35] further details of their development of PF-543, including comparative activity data for normethyl analogue **18** using a different assay system. In this study the methyl group was also shown to contribute only marginally to the strong SK1-selectivity of PF-543; its deletion led to a change in selectivity by less than a factor of 2.

Interestingly the sulfonate analogue (**19**) was 13-fold more potent against SK1 than its counterpart (**18**) with the sulfonylmethylene linker. A corresponding increase in inhibitory potency was also seen against SK2, with a quantifiable IC_{50} of 902 nM determined. Replacement of the sulfonyl group in **18** with a second methylene in **23** led to a modest 5.5-fold improvement in potency against SK1 but a pronounced enhancement in potency against SK2 so that the compound was almost equipotent against both isoforms (IC_{50} 26 and 35 nM for SK1 and SK2 respectively).

Taken together, these results suggest that the heel of the SK1 J-channel might be a tight fit for the sulfonylmethylene linker in PF-543 and **18** and supported our hypothesis that in SK2 the J-channel heel may be tighter still, encroaching sufficiently on the sulfonyl oxygens so as to be a key determinant for isoform discrimination. Thus, in SK2 higher compression is postulated along a trajectory (Axis-1 in Figure 3) between the head group and sulfonyl oxygens of the ligand, with the head group locked in place by a highly organised network of polar interactions involving features that normally serve to position the substrate for phosphorylation. These 'headlock' features include a structural water and an aspartic acid on helix-α7 (Asp178 in SK1, conserved as Asp308 in SK2) that have been shown to form three tight hydrogen bonds with charge stabilisation to the hydroxypyrrolidinium subunit of PF-543 in its SK1 co-crystal structure.[38]

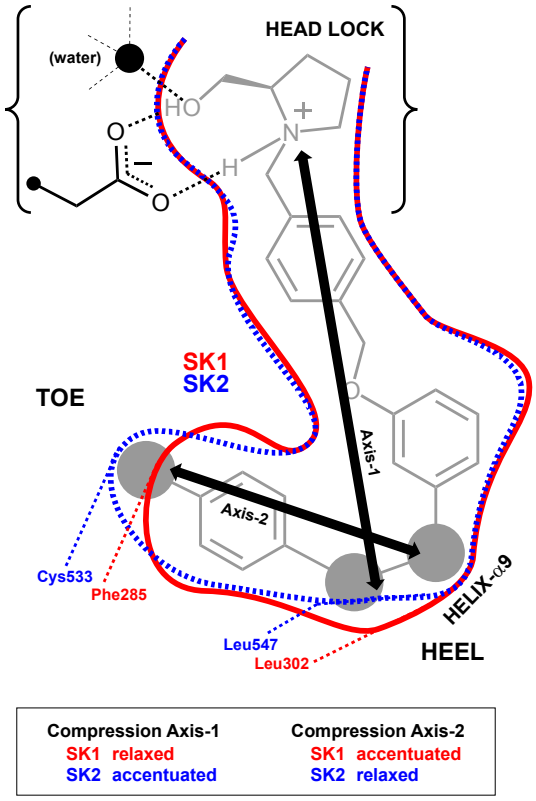

Figure 3. Key compression axes postulated to influence ligand binding to the J-channels of SK1 and SK2.

The methyleneoxy-linked analogue (**49**) also exhibited near equipotent inhibitory activity against the two isoforms, but with a marginal increase in overall potency relative to the ethylene-linked compound (**23**). Thus, **49** exhibited IC_{50} values of 14 and 16 nM against SK1 and SK2 respectively. However, replacement of the oxygen by a larger sulfur atom in compound **58** caused a 10-fold loss in potency against SK1 with only a slight loss (< 2-fold) against SK2, thereby resulting in a compound with reversed selectivity (albeit modest) in favour of SK2 (IC_{50} values of 137 and 26 nM against SK1 and SK2 respectively). This was an important finding because it supported our second hypothesis, namely that the J-channel toe is likely expanded in SK2 or/and exhibits greater plasticity. Thus, compression along an axis linking the large sulfur atom and *para* position of the phenyl ring in **58** (Axis-2 in Figure 3) might be less severe in SK2 than in SK1. Indeed, analysis of our PF-543/SK1 co-crystal structure[38] (Figure 2) had suggested a remarkably close fit for the phenylsulfonylmethylene tail unit of PF-543 in the SK1 J-channel, with the *para*-CH packed against Phe288 and the methylene of the linker wedged against helix-α9. Conceivably, alleviation of compression between these two points (and associated ligand strain) might contribute to the enhanced inhibitory potency of sulfonate **19** over the sulfonylmethylene-linked analogue (**18**).

We next sought to exploit the hypothesised tighter compression axis between toe and heel in SK1 (Axis-2 in Figure 3) still further by installation of a substituent in the terminal phenyl ring of **49** and **58**, with a particular focus on the *para*-position to see whether compounds with even greater selectivity for SK2 could be achieved. Given the potential differences in J-channel surface allied to the replacement of Ile174 in SK1 by Val304 in SK2, however, we also wished to examine the impact of substitution at the *ortho*- and *meta*-positions. For that reason, we evaluated fluorides **50**–**52** and chlorides **53**–**55** derived from methyleneoxy-linked parent **49**. The standout feature

with this compound set was indeed a pronounced loss in SK1-inhibitory potency for the *para*-fluoro and *para*-chloro analogues (**52** and **55**), which showed *ca*. 12-fold and 295-fold increases in IC_{50} relative to **49** respectively. Some loss in potency against SK2 was also observed for these compounds ($\leq$ 3-fold relative to parent **49**), but SK1 was preferentially penalised, leading to highly selective, nanomolar-potent SK2 inhibition in the case of chloride **55** (see concentration response curves in Figure 4). Curiously the *para*-fluoro analogue (**52**; SK2 IC_{50} 49 nM) showed equivalent or even rather more loss in SK2 potency relative to parent **49** (SK2 IC_{50} 16 nM) than its chloride counterpart (**55**; SK2 IC_{50} 41 nM). This outcome may reflect a requirement for some induced fit to accommodate the halogen in SK2. Thus, the cost associated with side chain perturbation caused by binding of the ligand might be offset by greater surface contact for the chloride over the fluoride.

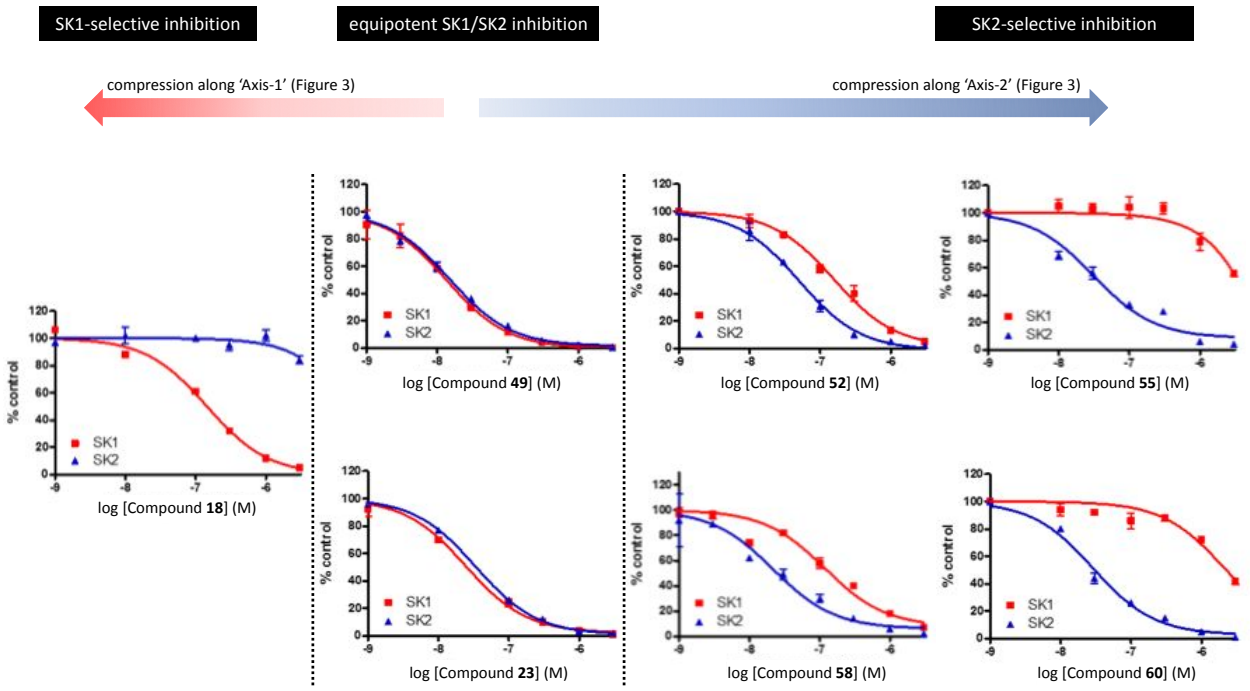

Figure 4. Selected SK1 and SK2 concentration response curves for PF-543-derived J-channel probes, highlighting the reversal of behaviour from SK1-selective inhibition (left) to SK2-selective

inhibition (right) with ligand features that induce compression along Axis-1 and Axis-2 of Figure 3 respectively. (Assay conditions: see legend to Chart 2.)

In the case of the methylenesulfanyl-linked analogue (**58**), the effects of *para*-fluoro and *para*-chloro substitution (**59**/**60**) broadly mirror those seen in the methyleneoxy-linked series (**52**/**55**), where inhibition of SK1 but not SK2 is significantly penalised (Chart 2). Although differences in the size and bond angle preferences of the sulfide and ether linkages may subtly modulate terminal halogen fit to the J-channel toe and ligand strain, in both cases the presence of the larger chlorine atom afforded greatest isoform discrimination, with selectivity for inhibition of SK2 over SK1 in the range of 75-fold to 100-fold for **60** and **55**. Introduction of bulkier or/and more polar *para*-substituents may be counterproductive for SK2 inhibitory performance however. Thus, in the methyleneoxy-linked series introduction of a methoxy group (compound **56**, SK2 IC_{50} 119 nM) led to a 7-fold loss in SK2 inhibitory potency relative to parent **49** and a linear nitrile extension (compound **57**, SK2 IC_{50} 1.12 μM) caused a 70-fold loss in activity. Whilst this fall off in inhibitory potency may reflect a limit to the capacity of the SK2 J-channel toe, changes in dipole and lipophilicity of the terminal subunit may also be factor in the activity fall off. Thus, a nitrile group is sometimes exploited as a bioisostere for the halogen in (hetero)aromatic chlorides, conferring a significant reduction in lipophilicity and, therefore, increased lipophilic ligand efficiency.[45, 46]

In contrast to substitution at the *para*-position, the SK1-inhibitory activity of **49** is more tolerant of halogenation at the *ortho*- and *meta*-positions on the terminal arene (Chart 2, compounds **50**, **51**, **53** and **54**). Here only modest activity loss (*ca*. 3-fold) is observed (**50**/**53**/**54**), whilst *meta*-fluorination even marginally enhances activity (**51**, SK1 IC_{50} 9 nM) relative to parent

49 (SK1 IC_{50} 14 nM). Interestingly SK2 is less tolerant of substitutions at the *ortho*- and *meta*-positions, particularly at the latter site, where fluorination (**51**, SK2 IC_{50} 143 nM) and chlorination (**54**, SK2 IC_{50} 412 nM) produce respectively 9-fold and 26-fold activity loss *versus* parent **49** (SK2 IC_{50} 16 nM). These results suggest that the SK2 J-channel foot, whilst extended compared to SK1, is tighter in width, at least between certain points.

Structural inferences for the SK2 J-channel. Crystal structures of SK1 have only recently emerged (since 2013), whilst no structures are currently available for SK2. To facilitate qualitative rationalization of the isoform selectivity profiles of the ligands, we constructed an homology model for SK2 based on the crystal structure (4V24) of the large SK1 splice variant (SK1b, sometimes also called SK1c) with bound PF-543 that we had recently determined at 1.8 Å resolution.[38] In brief, an initial model was generated using the default automated routines of the SWISS-MODEL server[47-50] and this was refined using the Small Molecule Drug Discovery software suite from Schrödinger, LLC. In particular, LBL-2 was remodelled from the structure of the corresponding loop in the *Enterococcus faecalis* diacylglycerol kinase family protein, as defined in the crystal structure 4WER (DOI: 10.2210/pdb4wer/pdb). The rationale for this adjustment was that the C-terminal end of LBL-2 in SK2 (524-RFDDGL-529) has sequence features that are more closely related to prokaryotic diacylglycerol kinases than to SK1 (Figure S1 in Adams *et al*[39]).

Our activity data for the normethyl analogue (**18**) of PF-543 suggested that the central ring methyl group in PF-543 is not a key SK2-discriminating feature and determinant of the high SK1-inhibitory selectivity exhibited by PF-543. Nevertheless, we did find that energy minimisation of our ligand probe set docked into the SK2 model, as illustrated for **60** in Figure 5A, tended to result in contraction of the J-channel notch that hosts the PF-543 methyl. This notch is formed at the

interface between helices-α8 and -α9 of the two flap-like LBL-1 and LBL-3 loops respectively (*cf.* Figure 1). As such, size and surface contouring of the notch may be sensitive to subtle changes in the seating of the two helices as well as to accessible conformational volumes of local residues. Indeed, inspection of an overlay of all protein chains from the currently available crystal structures revealed significant differences in the notch surface even across different SK1 structures, thus suggesting a degree of plasticity in this region of the J-channel (Figure 5B and 5C). A particularly important residue in this regard is Leu299 in SK1, which is located on helix-α9 and conserved in SK2 as Leu544 (marked in Figure 5). This residue exhibits some conformational variance across SK1 crystal structures and would expand the notch region in the SK2 model illustrated in Figure 5 to accommodate the PF-543 methyl group with only modest movement.

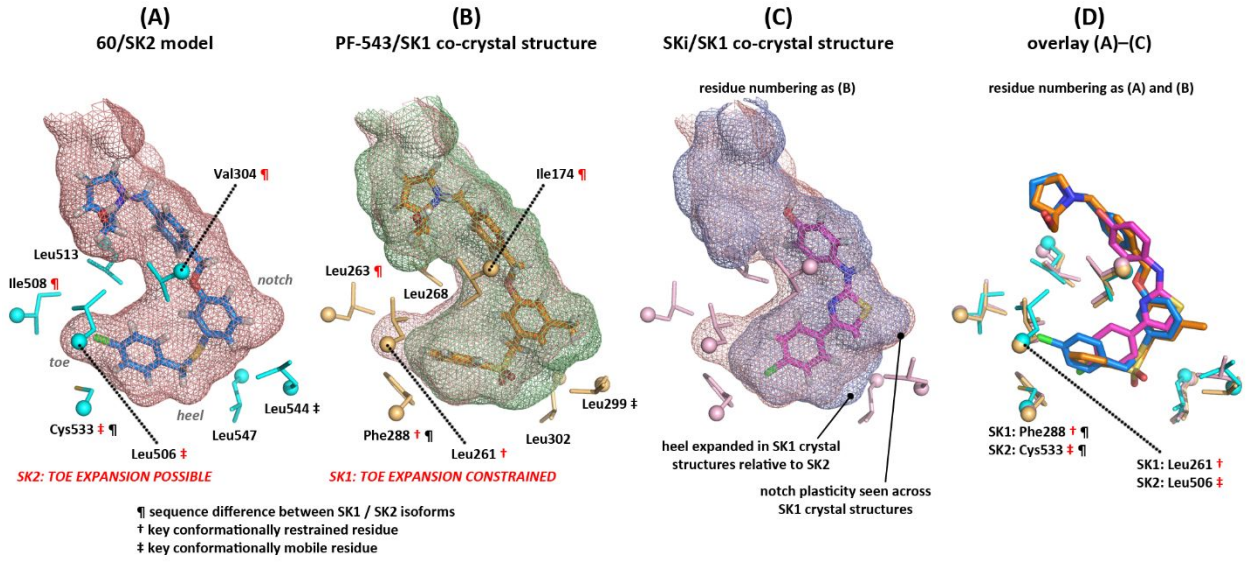

Figure 5. Comparison of modelled binding mode for SK2-selective inhibitor **60** with SK1 co-crystal structures of PF-543 (**1**) and SKi (**10**). *Panel (A):* **60** (blue stick) docked into SK2 model (red mesh), highlighting key contact residues (cyan stick) and expanded SK2 J-channel toe surface. *Panel (B):* PF-543 (**1**; orange stick) is shown from its co-crystal structure (4V24) with SK1 (green

mesh) and the SK2 model surface (red mesh) overlaid from (A); SK1 contact residues are shown (light orange stick) and the constrained SK1 J-channel toe surface is evident. *Panel (C):* As (B), but showing co-crystal structure (3VZD) of SKi (**10**, magenta stick) with SK1 (blue mesh and pink stick key contact residues) superimposed onto the SK2 model (red mesh) from panel (A); the heel region adjacent to SK1 Leu302 is consistently less compressed in SK1 structures (relative to the SK2 model), whilst the notch surface exhibits some plasticity. *Panel (D):* overlay of (A)–(C) minus the J-channel surface; the chlorine atom of **60** is accommodated in SK2 between Cys533 and Leu506, with rotation of the latter possible whilst the cognate SK1 residue (Leu261) is constrained by the packing of adjacent residues.

Although the notch region exhibits significant plasticity, inspection of the SK1 J-channel across different crystal structures revealed that the protein surface is quite tightly defined (irrespective of ligand occupancy) both around the J-channel heel that contacts the PF-543 sulfonyl group and around the toe that interfaces with the end of the PF-543 terminal phenyl subunit. Our data indicate that sulfonyl replacement by methylene in compounds **23** and **49** enhances SK1-inhibitory potency compared to the sulfonylmethylene-linked parent (**18**), which suggests that the sulfonylmethylene linker is already a little oversized for an optimal fit of the tail of the ligand to the SK1 J-channel. Thus, only a modest additional contraction in the SK2 J-channel at this point could generate a strongly unfavourable compressive effect for compounds such as PF-543 and its normethyl analogue (**18**) to account for their SK1 selectivity. The SK2 model supported the proposal that the SK2 J-channel may be contracted in the heel region, in particular due to inwards movement of Leu547 (corresponding to Leu302 in SK1), Figure 6A. However, the model also suggested that the basis for such movement may be a consequence, at least in part, of differences

in the LBL-2/LBL-3 interfaces of the isoforms and not merely due to local residue differences immediately surrounding the leucine, as we had first conceived (Figure 2). In particular, Leu547 is located on helix-α9 in LBL-3, and the C-terminal end of this helix engages the hairpin-like tip of LBL-2 (Figure 6a). The model suggested that residue differences in LBL-2 might promote an inward movement at the C-terminus of helix-α9, thereby exerting leverage on the J-channel heel through Leu547. As the key heel compression contact is against the Cβ atom of Leu547, rather than the end of the side chain, the leverage cannot be alleviated by side chain rotation. However, compounds with reduced steric demand in the heel (**23** and **49**) can be accommodated in both SK1 and SK2 (illustrated for **49** in Figure 6B and 6C).

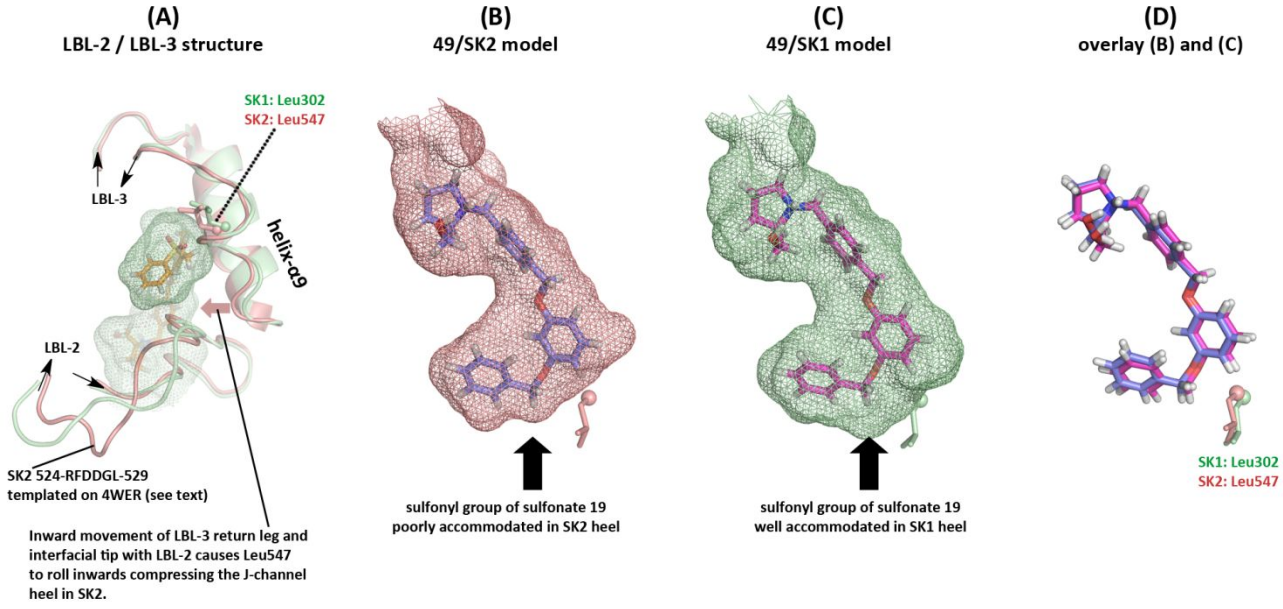

Figure 6. The J-channel heel is a key determinant of isoform discrimination by SK inhibitors. *Panel (A):* LBL-2 and LBL-3 are shown from the co-crystal structure (4V24) of PF-543 (orange stick) with SK1 (green ribbon); the corresponding elements from our SK2 homology model (red ribbon) are overlaid, illustrating inward movement in LBL-3 leading to heel compression in SK2 by Leu547. *Panel (B):* Potent unselective inhibitor **49** (blue stick) is shown modelled into the SK2

J-channel (red mesh); the J-channel heel surface is driven significantly inwards relative to SK1 so that the presence of a sulfonyl group in the ligand (**49** → **19**, 56-fold activity loss) is poorly tolerated by SK2. *Panel (C):* Inhibitor **49** (magenta stick) is again shown, here modelled into the SK1 J-channel (green mesh); the SK1 J-channel heel surface exhibits less compression and accommodates a sterically more demanding sulfonyl containing linker more readily (**49** → **19**, no activity loss; **23** → **18**, 5-fold activity loss). *Panel (D):* overlay of (B) and (C) minus the J-channel surface.

The model also suggested that the strong SK2 selectivity of the *para*-halo derivatives of **49**/**58** is indeed likely due to J-channel toe surface expansion, but that this may not be solely due to the single amino acid substitution of Phe288 in SK1 by Cys533 in SK2 (Figure 2). Indeed, in the absence of halogen substituents on the ligand, the energy minimised SK2 model complexes showed little apparent expansion in the toe surface compared to SK1, as illustrated for **49** docked to SK2 and SK1 (Figure 6B and 6C respectively). The key to accommodation of the *para*-halo atom appears to be perturbation in the conformation of an adjacent leucine (Leu506 in SK2, conserved in SK1 as Leu261) that packs against the cysteine. The combination of Cys533 and Leu506 generates the toe surface in SK2 (Figure 5), with movement of the latter predicted to allow expansion to accommodate the chlorine of **55**/**60**. The leucine additionally packs against two other non-conserved residues—Val304 (Ile174 in SK1) and Ile508 (Leu263 in SK1)—and our model suggests that loosened packing with these residues and the cysteine may confer greater plasticity in the toe of the SK2 J-channel than in SK1. Thus, ligand binding in SK2 may involve an element of induced fit in the J-channel toe, potentially with an associated energy cost that is more or less offset depending on the effectiveness of surface contact between the ligand and the expanded toe.

In contrast, the toe of the SK1 J-channel is likely to be more rigid and introduction of *para*-substitution in the ligand is predicted to generate an unfavourable compression between the J-channel toe and helix-α9, as illustrated in Figure 7 for chloride **60**. Despite the enhanced plasticity and capacity indicated for the SK2 J-channel toe, our results nevertheless indicate significant limitations on the size of the *para*-substituent that can be accommodated in SK2. Thus, the axis of the *para*-substituent is predicted to orientate directly at the Cβ atom of Ile508 presented from the SK2 CTD β-sandwich core, Figure 5A. In the case of chloride **60**, a distance of *ca*. 4.3 Å is predicted between Ile508 Cβ and the chlorine atom, and this spatial constraint likely contributes to the sharp drop in inhibitory potency against SK2 seen with the introduction of a *para*-cyano group in **57**.

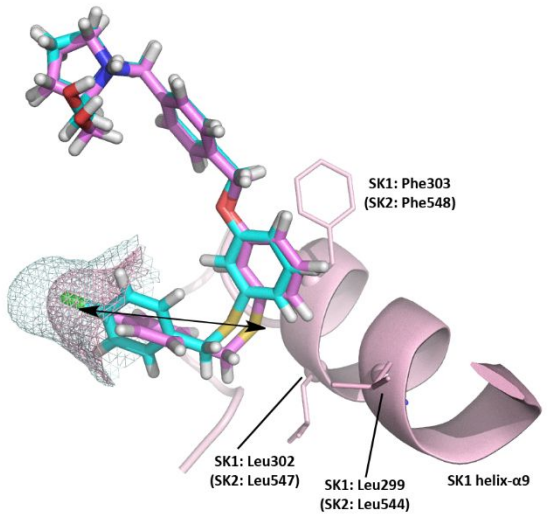

Figure 7. The J-channel toe is a second key determinant for isoform discrimination by SK inhibitors. A comparison of modelled binding modes for the SK2-selective inhibitor (**60**) is shown here, with the SK2-docked inhibitor (cyan stick) superimposed onto the SK1-docked inhibitor (magenta stick). With reduced plasticity in the SK1 J-channel toe (pink mesh), the sulfur atom of **60** is predicted to be tightly wedged against the backbone of helix-α9 (pink ribbon). This generates

an unfavourable compression axis (black arrow, corresponding to 'Axis-2' of Figure 3) that preferentially penalizes binding to SK1. In SK2 the greater plasticity of the J-channel toe (cyan mesh) is predicted to allow accommodation of **60** with less compression.

During the course of our work, Childress *et al*[36] described a series of pyrrolidine carboximidamide SK inhibitors with a spectrum of SK1- and SK2-inhibitory selectivity. The highest SK2-selectivity was seen with compound **9**, which is notable for its extended tail structure. With the guanidinium head group engaging key acidic residues in the mouth of the J-channel, the aminothiazole subunit in **9** would be expected to overlay the middle arene subunit of our ligands, whilst the oxadiazole ring of **9** would lie in plane and partially map onto the *p*-xylylene subunit (Figure 8B/C). However, an intriguing feature with such a binding mode is that the rod like biphenyl tail of **9** could only be accommodated if there is a significant expansion in the toe of the J-channel, and this on the other side of Cys533 to that occupied by the chlorine in **55**/**60**. There are two key residue substitutions that may make this possible for SK2 but not readily achievable for SK1: one is the replacement of SK1 Phe288 by Cys533 in SK2; the second is the exchange of SK1 Met312 for Phe557 in SK2. In the absence of compound **9** the latter residue, which is surface exposed on LBL-3, is predicted to fold inwards towards the adjacent cysteine (in partial surrogacy for the Phe288 residue of SK1). Rotation of these two side chains alone (Cys533/Phe557) was sufficient to open an extended pocket in our model and accommodate the terminal phenyl group of **9** with a reasonably relaxed biphenyl torsion (37°) and favourable packing interactions against Cys533, Phe557 and other aromatic residues (Tyr, His). This postulated binding mode for **9**, in effect, amounts to tunnelling between LBL-2 and LBL-3 in SK2. In SK1 the more rigid J-channel toe is stoppered by Phe288, for which a rotation analogous to that required of Cys533 in SK2 is

sterically precluded. The suggested binding mode for ligand **9** would also avoid encroachment on the Leu547 heel compression point in SK2 that we propose biases inhibitor selectivity towards SK1. Binding of compound **9** to SK1 would require much more extensive perturbation to the protein structure and packing of the LBL-3 return leg.

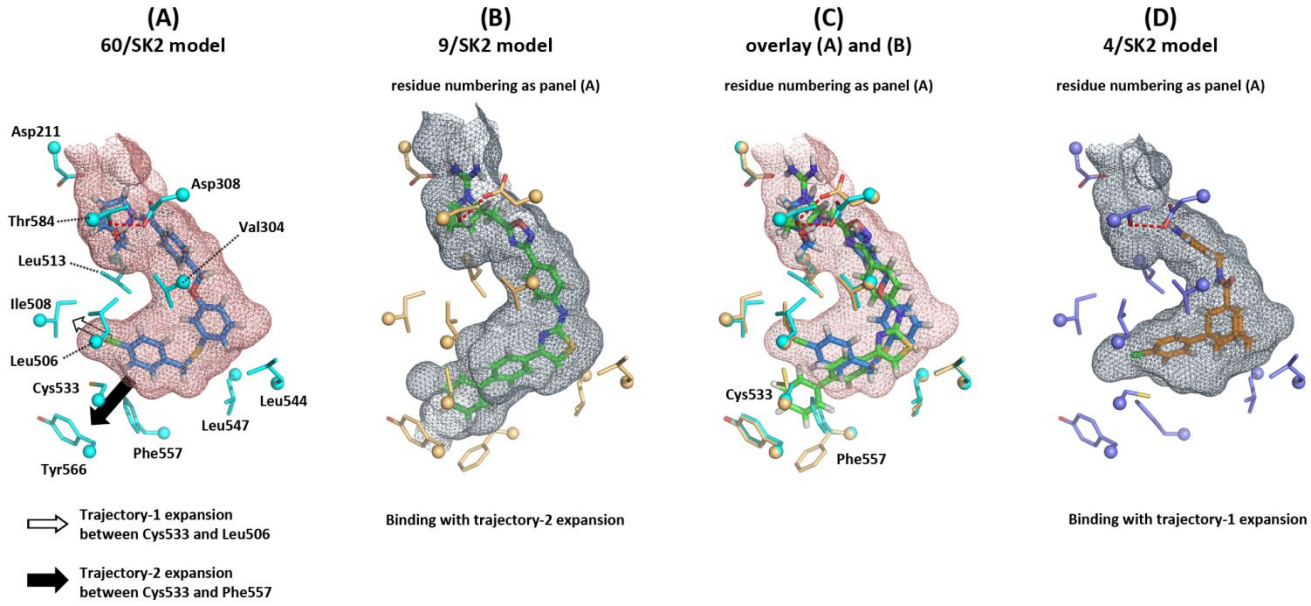

Figure 8. Plasticity in the J-channel toe of SK2 may be exploited to develop SK2-selective inhibitors. *Panel (A):* Compound **60** (blue stick) docked into the SK2 model (red mesh), highlighting key contact residues (cyan stick) and two predicted trajectories for possible toe expansion (arrows). Small groups may be accommodated between Cys533 and Leu506 (Trajectory-1, hollow arrow). This is the predicted expansion for binding of **55**/**60**, where the fit of the Cl atom is likely made possible largely by rotation in Leu506. Larger groups may be accommodated between Cys533 and Phe557 (Trajectory-2, filled arrow) upon rotation of these side chains. *Panel (B):* VT-20dd (**9**, green stick) docked into the SK2 model (grey mesh), highlighting key contact residues (orange stick). Here the ligand is predicted to exploit the second toe expansion trajectory. *Panel (C):* Overlay of (A) and (B) showing the SK2 J-channel surface

for docked **60** (red mesh) and illustrating the two key residue rotations in Cys533 and Phe557 required for Trajectory-2 expansion (cyan stick → orange stick positions). *Panel (D):* ABC294640 (**4**, orange stick) docked into SK2 (grey mesh). In this model, the Trajectory-1 expansion is made possible chiefly by rotation of Cys533 rather than Leu506, but the space generated by the expansion is underused by the Cl atom.

Although our analysis suggests that outward rotation of Phe557 might allow tunnelling of substantially extended ligand tail groups in SK2 (Figure 8C), the preferred orientation of the Phe557 side chain (in the absence of such ligand extensions) is predicted to lie inwards towards Cys533 to maximise surface contact with adjacent hydrophobic residues. In this tightly packed inward orientation, the end of the Phe557 side chain is predicted to come into close contact with the *meta*-position of the terminal phenyl ring of our PF-543-derived ligands series. This might contribute to the poor tolerance by SK2 of *meta*-halogenation, as seen with **51** and **54** (*vide supra*). In SK1 the cognate residue (Met312, Figure 2) is more flexible and exhibits less reach compared to Phe557 in SK2, which is consistent with the greater tolerance towards *meta*-halogenation in **51** and **54**. A suitable tail extension to enable tunnelling in SK2 ('Trajectory-2' in Figure 8) may require a large group to provoke the necessary rotation in Phe557 and compensate for the loss of packing interactions between this residue and adjacent side chains. Whilst potentially interesting for future investigation, our objective here was to achieve selectivity control with conservative changes in the parent ligand structure, thereby keeping molecular weight within druglike bounds.

We also docked ABC294640 (**4**) into our SK2 model for comparison (Figure 8D). In this case we found that the pyridyl group closely overlays the *p*-xylylene subunit of our ligands whilst the adamantyl group sits well in the J-channel bend—partly overlaying the middle arene of our

compounds but also the tail linker (and again without encroaching severely on the Leu547 heel compression point). The plane of the terminal chlorophenyl group was slightly rotated relative to **55**/**60**, but the chlorine atom occupied a similar position to that proposed for the chlorine in our SK2-selective compound, **55**.

CONCLUSIONS

Growing interest in the therapeutic potential of targets within the sphingolipid signalling pathway is fueling efforts to develop isoform-selective SK inhibitors across a range of chemotypes.[51-53] PF-543 has attracted significant attention as a nanomolar-potent SK1-selective inhibitor. However, a structural basis for the compound's SK1-over-SK2 selectivity has not been described until now, despite the recent disclosure of activity data for additional analogues.[35] Moreover, a lack of discriminating nanomolar-potent SK2-selective inhibitors as signalling pathway probes has hindered thorough exploration of the pharmacological potential of SK2 as a distinct target to date. From a clinical perspective, the most advanced compound remains the micromolar-potent, SK2-selective inhibitor, ABC294640 (**4**). However, the biological activity of this compound is complicated because it is a modulator of dihydroceramide desaturase and induces the proteasomal degradation of SK1.[31-33]

In order to develop a qualitative structural rationale for the design of isoform-selective inhibitors, we mapped SK2 sequence differences onto our recently determined[38] SK1/PF-543 co-crystal structure. That analysis (Figure 2) suggested a focus on the heel and toe of the J-channel, which we then probed with a concise set of PF-543 analogues modified in the tail linker and terminal phenyl ring (Chart 2). Our studies indicate that the phenyl group of PF-543, which is tightly fitted to the toe of the ligand-binding J-channel, constrains placement of the sulfonyl

oxygens of the ligand into a region of surface encroachment in the J-channel heel of SK2. Deleting the sulfonyl oxygens by installation of replacement linkers for the PF-543 sulfonylmethylene group endows the ligand with dual SK1/SK2-inhibitory activity (**23**, **49**, **58**). In contrast to the heel, our work suggests that the surface of the J-channel toe in SK2 may be expanded and exhibit greater plasticity compared to SK1. We have shown that this difference may be exploited with a suitably positioned halogenated terminal arene in the ligand to undermine inhibition of SK1. Coupled with replacement of the PF-543 sulfonylmethylene linker, this strategy allows full reversal in the SK isoform selectivity profile to be engineered, with up to 100-fold selectivity for SK2 over SK1 achieved in our series with *p*-chlorophenyl terminal ligand subunits. Comparative analysis of another recently disclosed SK2-selective inhibitor (**9**)[36] suggests an additional tail trajectory where ligand extensions may be accommodated through plasticity in SK2 that does not exist in SK1. Taken together, we suggest that these studies now provide a blueprint for rational design of isoform-selective SK inhibitors and the development of suitable tool compounds for further exploring the pharmacological potential of SK2 as a therapeutic target.

EXPERIMENTAL SECTION

SK1 and SK2 assays. Sphingosine kinase assays employed purified SK1 or purified SK2 (40-180 ng/ml) and were performed using the K_m concentrations of Sph (3 and 10 μM, respectively) and 250 μM [γ-^{32}P]ATP (0.75 kBq/nmol) for 30 min at 30 °C in a buffer containing 20 mM Tris (pH 7.4), 1 mM EDTA, 1 mM Na_3VO_4, 40 mM β-glycerophosphate, 1 mM NaF, 0.007% (v/v) β-mercaptoethanol, 20% (v/v) glycerol, 10 μg/mL aprotinin, 10 μg/mL soybean trypsin inhibitor, 1 mM PMSF, 0.5 mM 4-deoxypyridoxine (and 400 mM KCl in the case of SK2 assays). Sph was presented in Triton X-100 (final concentration, 0.063% w/v) for SK1 whereas

fatty acid free bovine serum albumin (final concentration, 0.2 mg/mL) was used in SK2 assays. Inhibitors were dissolved and diluted in DMSO (5% v/v final in assay). ^{32}P-sphingosine 1-phosphate was extracted with 500 μL of 1-butanol, followed by a phase-split using 1 mL of 2 M KCl and two washes of the lower (aqueous) phase, using 2 M KCl, to remove unreacted [γ-^{32}P]ATP before harvesting the upper (organic) phase and quantification by Cerenkov counting.

Synthetic chemistry general methods. Solvents and reagents were procured from commercial suppliers (Acros, Geel, Belgium; Alfa Aesar, Heysham, United Kingdom; Apollo Scientific, Stockport, United Kingdom; Fisher Scientific, Loughborough, United Kingdom; Fluorochem, Hadfield, United Kingdom; Sigma-Aldrich, Gillingham, United Kingdom) and used as supplied without further purification unless otherwise stated. "Light petroleum" refers to the fraction boiling between 40 and 60 °C. Analytical thin layer chromatography was carried out using aluminum backed plates coated with Merck Kieselgel 60 GF254 (No. 05554). Developed plates were visualized under ultraviolet light (254 nm and 366 nm) and/or by alkaline potassium permanganate dip. Preparative chromatography was performed (a) in conventional glass columns under flash column chromatography conditions (silica gel of 40–63 μm particle size from Fisher Scientific); or (b) using SP4 Biotage MPLC apparatus with silica gel of 40–63 μm particle size (Fisher Scientific) in 10 g or 50 g cartridges depending on the scale of material to be processed; or (c) using Strata® SI-1 cartridges (Phenomenex). Fully characterized compounds were chromatographically homogeneous. ^{1}H NMR spectra were recorded at 400 MHz on JEOL Lambda Delta 400, Bruker AMX-400 and Bruker AVIII-400 spectrometers; ^{13}C NMR spectra were recorded at 101 MHz on the same instruments. Chemical shifts are recorded in parts per million (δ in ppm) and are referenced against solvent signals (δ_C 77.16 for chloroform and δ_C 39.52 for methyl sulfoxide) for ^{13}C spectra and solvent residual resonances (δ_H 7.26 for chloroform and δ_H

2.50 methyl sulfoxide) for ^{1}H spectra.[54] ^{1}H and ^{13}C chemical shift values are accurate to ±0.01 ppm and ±0.1 ppm respectively. *J* values are given in Hz. Multiplicity designations used are as follows: s, d, t, q, sept, and m for singlet, doublet, triplet, quartet, septet, and multiplet (respectively); br denotes an exchange-broadened signal. ^{13}C signal assignments, taken from distortionless enhancement by polarization transfer (DEPT) experiments, are listed in parenthesis. High-resolution mass spectroscopy (HRMS) was carried out under electrospray ionisation (ESI), in a Fourier transform analyser by Exactive® ThermoFisher Scientific instrument. All compounds subjected to enzyme assay evaluation were ≥95% pure as determined by HPLC analysis. HPLC Method (A): YMC hydrosphere C_{18} 5 μm / 12 nm (150 × 4.5 mm) column under isocratic elution [0.1% CF_3CO_2H in 35/65 water/MeCN] at 0.7 mL/min and 40 °C with detection at λ 230 nm. HPLC Method (B): Poroshell 120 C_{18} 2.7 μm (75 x 4.6 mm) column under gradient elution from 95% water (5 mM NH_4OAc) and 5% MeCN (5 mM NH_4OAc) to 100% MeCN (5 mM NH_4OAc) at 1 mL/min and 40 °C with detection at λ 214 nm.

1-Methoxy-3-((phenylsulfonyl)methyl)benzene (12). A mixture of **11** (7.58 g, 37.7 mmol), sodium benzene sulfinate ($NaSO_2Ph$, 6.75 g, 41.1 mmol) and Aliquat® 336 (0.28 g, 0.70 mmol) was stirred at 85 °C for 18 h. The reaction mixture was diluted with hot EtOAc (120 mL), stirred at ambient temperature for 1 h and the resulting slurry filtered through Celite® to afford a filtrate that was concentrated *in vacuo*. The residue was subjected to flash column chromatography (light petroleum/EtOAc gradient 4:1 to 1:1) to afford **12** (4.61 g, 47%) as a white powder. ^{1}H NMR (400 MHz, $CDCl_3$) δ 3.71 (s, 3H), 4.28 (s, 2H), 6.61 (t, J = 2.2 Hz, 1H), 6.64 (ddd, J = 7.4, 1.6, 1.0 Hz, 1H), 6.85 (ddd, J = 8.3, 2.6, 1.0 Hz, 1H), 7.16 (t, J = 7.9 Hz, 1H), 7.44–7.48 (m, 2H), 7.58–7.63 (m, 1H), 7.64–7.67 (m, 2H).

3-((Phenylsulfonyl)methyl)phenol (14). To a solution of **12** (1.31 g, 5.00 mmol) in anhydrous CH_2Cl_2 (30 mL) at –78 °C under N_2 was added dropwise BBr_3 (1 M in CH_2Cl_2; 5.50 mL, 5.50 mmol). The mixture was allowed to come to ambient temperature over 2 h and then cooled to 0°C and quenched with saturated $NaHCO_3$ (40 mL). The separated aq. phase was back extracted with CH_2Cl_2 (2×30 mL). The combined organics were washed with brine (2×15 mL), dried (Na_2SO_4) and filtered. The filtrate was evaporated and the resulting residue subjected to flash column chromatography (CH_2Cl_2/MeOH gradient 99.5:0.5 to 99:1) to afford **14** (958 mg, 77%) as a white powder. ^{1}H NMR (400 MHz, $CDCl_3$) δ 4.26 (s, 2H), 4.88 (s, 1H), 6.58 (ddd, J = 7.6, 1.6, 0.9 Hz, 1H), 6.66 (1 H, app. t, J 2.0), 6.79 (ddd, J = 8.2, 2.6, 0.9 Hz, 1H), 7.10 (t, J = 7.9 Hz, 1H), 7.44–7.49 (m, 2H), 7.59–7.63 (m, 1H), 7.65–7.68 (m, 2H).

3-Hydroxyphenyl benzenesulfonate (15). A mixture of resorcinol (500 mg, 4.54 mmol), K_2CO_3 (1.88 g, 13.6 mmol) and phenylsulfonyl chloride (637 µL, 4.99 mmol) in MeCN (6 mL) was stirred at ambient temperature for 16 h. The mixture was partitioned between Et_2O and water, and the separated organic phase then washed with saturated K_2CO_3 solution and extracted with 1 M NaOH (aq). The aqueous extract was acidified with 3 M HCl (aq) and back extracted with Et_2O. The organic phase was dried ($MgSO_4$) and evaporated to afford **15** (244 mg, 21%) as a beige solid. ^{1}H NMR (400 MHz, DMSO-d_6) δ 6.37–6.47 (m, 2H), 6.69 (dd, J = 8.1, 1.5 Hz, 1H), 7.11–7.15 (m, 1H), 7.65–7.69 (m, 2H), 7.81 (t, J = 7.5 Hz, 1H), 7.86 (d, J = 7.6 Hz, 2H), 9.87 (br s, 1H). ^{13}C NMR (101 MHz, DMSO-d_6) δ 106.2, 109.0, 112.1, 114.5, 128.1, 128.1, 129.7, 134.9, 149.8, 158.5.

4-((3-((Phenylsulfonyl)methyl)phenoxy)methyl)benzaldehyde (16). A stirred mixture of **14** (283 mg, 1.14 mmol), 4-(bromomethyl)benzaldehyde (239 mg, 1.20 mmol) and K_2CO_3 (440 mg, 3.19 mmol) in MeCN (8.0 mL) was heated at 60 °C for 3 h. The mixture was filtered through Celite® to afford a filtrate that was concentrated *in vacuo*. The residue was partitioned between

EtOAc (50 mL) and water (20 mL). The organic phase was washed with brine (15 mL), dried ($MgSO_4$) concentrated and processed by flash column chromatography (CH_2Cl_2 to 0.5% MeOH/CH_2Cl_2 gradient elution) to afford **16** (338 mg, 81%) as a white powder. ^{1}H NMR (400 MHz, $CDCl_3$) δ 4.28 (s, 2H),5.07 (s, 2H), 6.65 (ddd, J = 7.5, 1.6, 0.9 Hz, 1H), 6.78 (dd, J = 2.5, 1.6 Hz, 1H), 6.92 (ddd, J = 8.3, 2.6, 1.0 Hz, 1H), 7.16 (dd, J = 8.3, 7.6 Hz, 1H), 7.43–7.48 (m, 2H), 7.55–7.58 (m, 2H), 7.58–7.63 (m, 1H), 7.63–7.67 (m, 2H), 7.89–7.92 (m, 2H), 10.03 (s, 1H). ^{13}C NMR (101 MHz, $CDCl_3$) δ 62.8 (CH_2), 69.2 (CH_2), 115.6 (CH), 117.0 (CH), 123.9 (CH), 127.5 (2×CH), 128.6 (2×CH), 128.9 (2×CH), 129.6 (C), 129.7 (CH), 133.1 (CH), 130.0 (2×CH), 136.1 (C), 138.0 (C), 143.6 (C), 158.4 (C), 191.8 (CO).

3-((4-Formylbenzyl)oxy)phenyl benzenesulfonate (17). Following the procedure for **16**, phenol **15** (150 mg, 0.568 mmol) afforded **17** (196 mg, 88%) as a colourless solid. ^{1}H NMR (400 MHz, DMSO-d_6) δ 5.16 (s, 2H), 6.62 (ddd, J = 8.1, 2.2, 0.8 Hz, 1H), 6.69–6.70 (m, 1H), 6.99 (ddd, J = 8.4, 2.5, 0.8 Hz, 1H), 7.27–7.31 (m, 1H), 7.60 (d, J = 8.1 Hz, 2H), 7.66 (dd, J = 8.2, 7.5 Hz, 2H), 7.77–7.84 (m, 1H), 7.86 (dd, J = 8.2, 1.3 Hz, 2H), 7.93 (d, J = 8.1 Hz, 2H), 10.02 (s, 1H). ^{13}C NMR (101 MHz, DMSO-d_6) δ 68.9, 108.9, 114.1, 114.3, 127.8, 128.2, 129.7, 129.7, 130.5, 134.2, 135.0, 135.7, 143.3, 149.8, 158.8, 192.8.

(*R*)-(1-(4-((3-((Phenylsulfonyl)methyl)phenoxy)methyl)benzyl)pyrrolidin-2-yl)methanol (18). To a solution of **16** (96 mg, 0.262 mmol) and (*R*)-(–)-2-pyrrolidinemethanol (28 µL, 0.287 mmol) in 1,2-dichloroethane (2 mL) was added $NaBH(OAc)_3$ (83 mg, 0.393 mmol). The mixture was stirred at ambient temperature for 16 h. A further portion of $NaBH(OAc)_3$ (28 mg, 0.13 mmol) was added and stirring continued for 18 h until complete consumption of **16** was observed by TLC analysis (CH_2Cl_2/MeOH 9:1). The mixture was diluted with CH_2Cl_2 (30 mL) and washed with saturated $NaHCO_3$ solution (10 mL). The organic phase was dried ($MgSO_4$),

evaporated and the resulting residue subjected to flash column chromatography (gradient elution, 1% to 5% MeOH in CH_2Cl_2) to afford **18** (84 mg, 71%) as a white powder. ^{1}H NMR (400 MHz, $CDCl_3$) δ 1.65–1.75 (m, 2H), 1.80–1.88 (m, 1H), 1.88–1.99 (m, 1H), 2.30 (q, J = 8.4 Hz, 1H), 2.40–3.00 (br s, 1H), 2.72–2.78 (m, 1H), 2.96–3.01 (m, 1H), 3.38 (d, J = 13.0 Hz, 1H), 3.44 (dd, J = 10.8, 2.2 Hz, 1H), 3.66 (dd, J = 10.8, 3.5 Hz, 1H), 3.98 (d, J = 13.0 Hz, 1H), 4.28 (s, 2H), 4.94 (s, 2H), 6.64 (dt, J = 7.6, 1.2 Hz, 1H), 6.73 (dd, J = 2.5, 1.7 Hz, 1H), 6.92 (ddd, J = 8.3, 2.6, 1.0 Hz, 1H), 7.15 (dd, J = 8.3, 7.6 Hz, 1H), 7.29–7.37 (m, 4H), 7.43–7.48 (m, 2H), 7.58–7.63 (m, 1H), 7.63–7.66 (m, 2H). ^{13}C NMR (101 MHz, $CDCl_3$) δ 23.5 (CH_2), 27.8 (CH_2), 54.5 (CH_2), 58.3 (CH_2), 61.8 (CH_2), 62.9 (CH_2), 64.4 (CH), 69.9 (CH_2), 115.7 (CH), 117.0 (CH), 123.4 (CH), 127.6 (2×CH), 128.7 (2×CH), 128.9 (2×CH), 128.9 (2×CH), 129.5 (C), 129.6 (CH), 133.7 (CH), 135.5 (C), 138.0 (C), 139.3 (C), 158.8 (C). ESI-HRMS $[M + H]^+$ calcd for $C_{26}H_{30}NO_4S^+$, 452.1890; found, 452.1904. HPLC: Method (A) t_R 3.89 min (99.5%).

(*R*)-3-((4-((2-(Hydroxymethyl)pyrrolidin-1-yl)methyl)benzyl)oxy)phenyl benzenesulfonate (19). Following the procedure for **18**, aldehyde **17** (100 mg, 0.271 mmol) afforded **19** (40 mg, 33%) as a colourless oil. ^{1}H NMR (400 MHz, DMSO-d_6) δ 1.52–1.65 (m, 3H), 1.79–1.88 (m, 1H), 2.10–2.16 (m, 1H), 2.52–2.59 (m, 1H), 2.73–2.78 (m, 1H), 3.26–3.31 (br m, 1H), 3.33 (d, J = 13.3 Hz, 1H), 3.45 (br. dd, J = 10.3 and 3.9 Hz, 1H), 4.04 (d, J = 13.3 Hz, 1H), 4.38 (br s, 1H), 4.98 (s, 2H), 6.59 (ddd, J = 8.2, 2.2 and 0.7 Hz, 1H), 6.66 (t, J = 2.3 Hz, 1H), 6.96 (ddd, J = 8.4, 2.4 and 0.7 Hz, 1H), 7.27 (t, J = 8.3 Hz, 1H), 7.31 (app. s, 4H), 7.64–7.69 (m, 2H), 7.80–7.84 (m, 1H), 7.84–7.87 (m, 2H). ^{13}C NMR (101 MHz, DMSO-d_6) δ 22.5, 28.0, 54.0, 58.4, 64.2, 64.8, 69.5, 108.8, 114.0, 127.6, 128.2, 128.6, 129.7, 130.4, 134.3, 134.6, 135.0, 139.9, 148.8, 149.8, 159.2. ESI-HRMS $[M + H]^+$ calcd for $C_{25}H_{28}NO_5S^+$, 454.1683; found, 454.1681. HPLC: Method (B) t_R 6.64 min (96.7%).

3-(Phenylethynyl)phenol (20). A flask was charged under Ar with 3-iodophenol (1.51 g, 6.86 mmol), copper(I) iodide (140 mg, 734 μmol), tetrakis(triphenylphosphine)palladium(0) (382 mg, 332 μmol), anhydrous THF (30 mL), triethylamine (24 mL) and phenylacetylene (2.80 g, 27.4 mmol). The mixture was stirred at ambient temperature for 48 h, concentrated *in vacuo* and the resulting residue partitioned between $CHCl_3$ (100 mL) and 1 M HCl (aq) (200 mL). The organic phase was dried ($MgSO_4$) and evaporated. The residual oil was processed by flash column chromatography (1:2:8 Et_2O/CH_2Cl_2/light petroleum) followed by crystallisation (CH_2Cl_2/light petroleum) to afford **20** (759 mg, 57%) as off-white plates. ^{1}H NMR (400 MHz, $CDCl_3$) δ 4.77 (br. s, 1H), 6.83 (ddd, J = 8.1, 2.6 and 1.0 Hz, 1H), 7.01 (dd, J = 2.4 and 1.4 Hz, 1H), 7.13 (dt, J = 7.6 and 1.2 Hz, 1H), 7.23 (t, J = 7.9 Hz, 1H), 7.31–7.38 (m, 3H), 7.50–7.55 (m, 2H). ^{13}C NMR (101 MHz, $CDCl_3$) δ 89.1 (C), 89.6 (C), 115.9 (CH), 118.4 (CH), 123.3 (C), 124.6 (CH), 124.7 (C), 128.5 (3×CH), 129.8 (CH), 131.8 (2×CH), 155.4 (C).

3-Phenethylphenol (21). A solution of **20** (400 mg, 2.06 mmol) in EtOH (40 mL) was hydrogenated using an H-Cube™ (ThalesNano) fitted with a 10% Pd/C cartridge under full H_2 mode at 30 °C with a flow rate of 0.7 mL/minute. The hydrogenated product solution was evaporated to **21** (390 mg, 95%) as a colourless oil that solidified to a crystalline solid on standing. ^{1}H NMR (400 MHz, $CDCl_3$) δ 2.86–2.95 (m, 4H), 4.68 (br. s, 1H), 6.67–6.69 (m, 2H), 6.78 (app. d, J = 7.5 Hz, 1H), 7.14–7.23 (m, 4H), 7.27–7.32 (m, 2H). ^{13}C NMR (101 MHz, $CDCl_3$) δ 37.75 (CH_2), 37.80 (CH_2), 113.0 (CH), 115.6 (CH), 121.2 (CH), 126.1 (CH), 128.5 (2×CH), 128.6 (2×CH), 129.7 (CH), 141.8 (C), 143.9 (C), 155.5 (C).

4-((3-Phenethylphenoxy)methyl)benzaldehyde (22). A mixture of 4-(bromomethyl)benzaldehyde (301 mg, 1.51 mmol), **21** (337 mg, 1.70 mmol) and K_2CO_3 (707 mg, 5.12 mmol) in MeCN (10 mL) was stirred at ambient temperature for 16 h. The mixture was diluted

with CH_2Cl_2 (25 mL), filtered through Celite® and the filtrate evaporated to dryness. The residual oil was processed chromatographically (20 g Strata® SI-1 cartridge; 1 : 39 : 60 Et_2O/CH_2Cl_2/light petroleum) to afford **22** (417 mg, 87%) as a colourless oil. ^{1}H NMR (400 MHz, $CDCl_3$) δ 2.86–2.96 (m, 4H), 5.12 (s, 2H), 6.79–6.84 (m, 3H), 7.16–7.23 (m, 4H), 7.26–7.31 (m, 2H), 7.59–7.62 (AA'BB' m, 2H), 7.89–7.92 (AA'BB' m, 2H), 10.03 (s, 1H). ^{13}C NMR (101 MHz, $CDCl_3$) δ 37.8 (CH_2), 38.0 (CH_2), 69.2 (CH_2), 112.2 (CH), 115.3 (CH), 121.7 (CH), 126.1 (CH), 127.6 (2×CH), 128.45 (2×CH), 128.55 (2×CH), 129.5 (CH), 130.1 (2×CH), 136.0 (C), 141.7 (C), 143.7 (C), 144.3 (C), 158.5 (C), 192.0 (CH).

(*R*)-(1-(4-((3-Phenethylphenoxy)methyl)benzyl)pyrrolidin-2-yl)methanol (23). Following the procedure for **18**, aldehyde **22** (417 mg, 1.32 mmol) afforded **23** (432 mg, 82%) as a colourless oil. ^{1}H NMR (400 MHz, $CDCl_3$) δ 1.66–1.76 (m, 2H), 1.81–2.00 (m, 2H), 2.30 (td, J = 9.3 and 7.5 Hz, 1H), 2.50–3.00 (br. s, 1H), 2.73–2.78 (m, 1H), 2.88–2.96 (m, 4H), 2.97–3.02 (m, 1H), 3.39 (d, J = 13.1 Hz, 1H), 3.45 (dd, J = 10.8 and 1.9 Hz, 1H), 3.68 (dd, J = 10.8 and 3.5 Hz, 1H), 3.99 (d, J = 13.1 Hz, 1H), 5.02 (s, 2H), 6.80–6.84 (m, 3H), 7.19–7.23 (m, 4H), 7.28–7.41 (m, 6H). ^{13}C NMR (101 MHz, $CDCl_3$) δ 23.6 (CH_2), 27.9 (CH_2), 37.9 (CH_2), 38.1 (CH_2), 54.5 (CH_2), 58.3 (CH_2), 61.9 (CH_2), 64.4 (CH), 69.8 (CH_2), 112.3 (CH), 115.3 (CH), 121.2 (CH), 126.0 (CH), 127.7 (2×CH), 128.4 (2×CH), 128.5 (2×CH), 129.0 (2×CH), 129.4 (CH), 136.0 (C), 139.2 (C), 141.8 (C), 143.5 (C), 159.0 (C). ESI-HRMS $[M + H]^+$ calcd for $C_{27}H_{32}NO_2^+$, 402.2428; found, 402.2434. HPLC: Method (A) t_R 4.73 min (>99%).

3-(Benzyloxy)phenol (25). A heavy-walled sealable reaction flask was charged with resorcinol (2.20 g, 20.0 mmol), K_2CO_3 (2.80 g, 20.3 mmol), acetone (30 mL) and a magnetic stir bar. Benzyl bromide (1.72 g, 10.1 mmol) was added and the flask closed under Argon. The mixture was then heated at 65–70 °C. After 5 h the mixture was returned to ambient temperature and

filtered through Celite®, washing well with acetone. The filtrate was evaporated to afford a residue that was partitioned between $CHCl_3$ (100 mL) and water (100 mL). The organic phase was separated and the aqueous layer extracted with $CHCl_3$ (25 mL). The combined organic phase was dried ($MgSO_4$) and evaporated to give a residue that was processed by flash column chromatography (25% Et_2O/light petroleum). Fractions containing the target material were evaporated to afford **25** (1.11 g, 55%) as a colourless oil that solidified to a crystalline solid on standing. ^{1}H NMR (400 MHz, $CDCl_3$) δ 4.67 (br s, 1H), 5.04 (s, 2H), 6.44 (ddd, J = 8.0, 2.4 and 0.9, 1H), 6.49 (t, J = 2.3, 1H), 6.58 (ddd, J = 8.3, 2.4 and 0.8, 1H), 7.14 (t, J = 8.1, 1H), 7.30–7.45 (m, 5H). ^{13}C NMR (101 MHz, $CDCl_3$) δ 70.2 (CH_2), 102.6 (CH), 107.6 (CH), 108.3 (CH), 127.6 (2×CH), 128.1 (CH), 128.7 (2×CH), 130.3 (CH), 136.9 (C), 156.7 (C), 160.1 (C).

3-((2-Fluorobenzyl)oxy)phenol (26). Following the procedure for **25**, 2-fluorobenzyl bromide (1.91 g, 10.1 mmol) afforded **26** (1.17 g, 53%) as a pale yellow oil. ^{1}H NMR (300 MHz, $CDCl_3$) δ 4.86 (br s, 1H), 5.11 (s, 2H), 6.45 (ddd, J = 8.0, 2.4 and 0.8 Hz, 1H), 6.50 (t, J = 2.3 Hz, 1H), 6.59 (ddd, J = 8.3, 2.4 and 0.8 Hz, 1H), 7.06–7.19 (m, 3H), 7.32 (tdd, J = 7.8, 5.6 and 2.1 Hz, 1H), 7.47–7.53 (m, 1H). ^{13}C NMR (75 MHz, $CDCl_3$) δ 63.9 (d, J = 4.5 Hz, CH_2), 102.6 (CH), 107.5 (CH), 108.5 (CH), 115.4 (d, J = 21.1 Hz, CH), 124.0 (d, J = 14.3 Hz, C), 124.4 (d, J = 3.6 Hz, CH), 129.8 (d, J = 2.9 Hz, CH), 129.9 (d, J = 1.3 Hz, CH), 130.4 (CH), 156.6 (C), 159.9 (C), 160.6 (d, J = 247.1 Hz, C). ^{19}F NMR (282 MHz, $CDCl_3$) δ –118.5.

3-((3-Fluorobenzyl)oxy)phenol (27). Following the procedure for **25**, 3-fluorobenzyl bromide (1.91 g, 10.1 mmol) afforded **27** (1.27 g, 58%) as a pale yellow oil. ^{1}H NMR (300 MHz, $CDCl_3$) δ 5.03 (s, 2H), 5.07 (br s, 1H), 6.44–6.49 (m, 2H), 6.57 (ddd, J = 8.3, 2.3 and 0.9 Hz, 1H), 6.98–7.05 (m, 1H), 7.12–7.20 (m, 3H), 7.34 (td, J = 7.9 and 5.8 Hz, 1H). ^{13}C NMR (75 MHz, $CDCl_3$) δ 69.3 (CH_2), 102.6 (CH), 107.6 (CH), 108.5 (CH), 114.3 (d, J = 22.0 Hz, CH), 114.9 (d,

J = 21.1 Hz, CH), 122.9 (CH), 130.2 (d, J = 8.2 Hz, CH), 130.4 (CH), 139.5 (d, J = 7.3 Hz, C), 159.8 (C), 161.4 (C), 163.1 (d, J = 246.1 Hz, C). ^{19}F NMR (282 MHz, $CDCl_3$) δ –112.6.

3-((4-Fluorobenzyl)oxy)phenol (28). Following the procedure for **25**, 4-fluorobenzyl bromide (1.83 g, 9.67 mmol) afforded **28** (803 mg, 38%) as a colourless crystalline solid. ^{1}H NMR (400 MHz, $CDCl_3$) δ 4.98 (br s, 1H), 4.99 (s, 2H), 6.45 (ddd, J = 7.9, 2.3 and 0.8,1H), 6.48 (t, J = 2.2, 1H), 6.56 (ddd, J = 8.3, 2.3 and 0.9,1H), 7.03–7.11 (m, 2H), 7.14 (t, J = 8.1, 1H), 7.36–7.43 (m, 2H). ^{13}C NMR (75 MHz, $CDCl_3$) δ 69.5 (CH_2), 102.7 (CH), 107.4 (CH), 108.4 (CH), 115.6 (d, J = 21.4, CH), 129.5 (d, J = 8.2, CH), 130.3 (CH), 132.7 (d, J = 3.0, C), 156.9 (C), 160.0 (C), 162.6 (d, J = 246, C). ^{19}F NMR (282 MHz, $CDCl_3$) δ –114.2.

3-((2-Chlorobenzyl)oxy)phenol (29). Following the procedure for **25**, 2-chlorobenzyl bromide (2.01 g, 9.79 mmol) afforded **29** (1.24 g, 54%) as a pale yellow oil. ^{1}H NMR (300 MHz, $CDCl_3$) δ 4.72 (br s, 1H), 5.11 (s, 2H), 6.42 (dd, J = 8.0 and 2.3 Hz, 1H), 6.47 (t, J = 2.3 Hz, 1H), 6.55 (dd, J = 8.2 and 2.3 Hz, 1H), 7.12 (t, J = 8.1, 1H), 7.19–7.29 (m, 2H), 7.32–7.39 (m, 1H), 7.48–7.54 (m, 1H). ^{13}C NMR (75 MHz, $CDCl_3$) δ 67.3 (CH_2), 102.7 (CH), 107.5 (CH), 108.6 (CH), 127.0 (CH), 129.0 (CH), 129.1 (CH), 129.4 (CH), 130.4 (CH), 132.7 (C), 134.5 (C), 156.7 (C), 159.8 (C).

3-((3-Chlorobenzyl)oxy)phenol (30). Following the procedure for **25**, 3-chlorobenzyl bromide (2.01 g, 9.77 mmol) afforded **30** (1.12 g, 49%) as a pale yellow oil. ^{1}H NMR (300 MHz, $CDCl_3$) δ 4.90 (br s, 1H), 5.01 (s, 2H), 6.44–6.48 (m, 2H), 6.55 (ddd, J = 8.3, 2.2 and 1.1 Hz, 1H), 7.11–7.18 (m, 1H), 7.28–7.40 (m, 3H), 7.32–7.39 (m, 1H), 7.42–7.44 (m, 1H). ^{13}C NMR (75 MHz, $CDCl_3$) δ 69.3 (CH_2), 102.6 (CH), 107.5 (CH), 108.6 (CH), 125.5 (CH), 127.5 (CH), 128.2 (CH), 129.9 (CH), 130.4 (CH), 134.5 (C), 138.9 (C), 156.6 (C), 159.8 (C).

3-((4-Chlorobenzyl)oxy)phenol (31). Following the procedure for **25**, 4-chlorobenzyl chloride (1.62 g, 10.1 mmol) afforded **31** (1.14 g, 48%) as a colourless crystalline solid. ^{1}H NMR (400 MHz, $CDCl_3$) δ 4.99 (s, 2H), 5.12 (br s, 1H), 6.43–6.48 (m, 2H), 6.56 (dd, J = 8.1 and 2.2, 1H), 7.14 (t, J = 8.1, 1H), 7.30–7.40 (tight AA'BB' m, 4H). ^{13}C NMR (101 MHz, $CDCl_3$) δ 69.5 (CH_2), 102.8 (CH), 107.6 (CH), 108.5 (CH), 128.9 (4×CH), 130.4 (CH), 133.9 (C), 135.5 (C), 156.8 (C), 160.1 (C).

3-((4-Methoxybenzyl)oxy)phenol (32). Following the procedure for **25**, 4-methoxybenzyl chloride (1.57 g, 10.0 mmol) afforded **32** (736 mg, 32%) as a white powder. ^{1}H NMR (300 MHz, $CDCl_3$) δ 3.82 (s, 3H), 4.67 (br s, 1H), 4.96 (s, 2H), 6.43 (1 H, ddd, J = 8.0, 2.4 and 0.8, 1H), 6.47 (t, J = 2.3, 1H), 6.57 (ddd, J = 8.3, 2.4 and 0.8, 1H), 6.89–6.94 (AA'BB' m, 2H), 7.13 (t, J = 8.2, 1H), 7.33–7.37 (AA'BB' m, 2H). ^{13}C NMR (75 MHz, $CDCl_3$) δ 55.5 (CH_3), 70.0 (CH_2), 102.6 (CH), 107.5 (CH), 108.1 (CH), 114.2 (2×CH), 129.1 (C), 129.4 (2×CH), 130.3 (CH), 156.8 (C), 159.4 (C), 160.3 (C).

4-((3-Hydroxyphenoxy)methyl)benzonitrile (33). Following the procedure for **25**, 4-cyanobenzyl bromide (1.96 g, 9.98 mmol) afforded **33** (1.05 g, 47%) as an off-white powder. ^{1}H NMR (400 MHz, $CDCl_3$) δ 4.90 (br s, 1H), 5.10 (s, 2H), 6.45–6.48 (m, 2H), 6.53 (ddd, J = 8.3, 2.3 and 1.0, 1H), 7.12–7.17 (m, 1H), 7.52–7.55 (AA'BB' m, 2H), 7.66–7.69 (AA'BB' m, 2H). ^{13}C NMR (101 MHz, $CDCl_3$) δ 69.1 (CH_2), 102.7 (CH), 107.4 (CH), 108.8 (CH), 111.9 (C), 118.8 (C), 127.7 (2×CH), 130.5 (CH), 132.6 (2×CH), 142.7 (C), 157.1 (C), 159.8 (C).

3-(Benzylthio)phenol (34). A mixture of 3-mercaptophenol (621 mg, 4.92 mmol), benzyl bromide (888 mg, 5.19 mmol) and K_2CO_3 (2.05 g, 14.8 mmol) in acetonitrile (10 mL) was stirred under Ar at ambient temperature. After 2 d the reaction mixture was diluted with CH_2Cl_2 (25 mL) and filtered through Celite®, washing well with CH_2Cl_2. The filtrate was evaporated and the

residue processed chromatographically (20 g Strata® SI-1 cartridge; 1:3:8 Et_2O/CH_2Cl_2/light petroleum) to afford **34** (720 mg, 68%) as a colourless solid. ^{1}H NMR (400 MHz, $CDCl_3$) δ 4.12 (s, 2H), 4.90 (br. s, 1H), 6.64 (ddd, J = 8.1, 2.5 and 0.9 Hz, 1H), 6.78 (t, J = 2.1 Hz, 1H), 6.88 (ddd, J = 7.8, 1.7 and 0.9 Hz, 1H), 7.13 (t, J = 7.9 Hz, 1H), 7.22–7.33 (m, 5H). ^{13}C NMR (101 MHz, $CDCl_3$) δ 38.6 (CH_2), 113.5 (CH), 116.1 (CH), 121.7 (CH), 127.4 (CH), 128.6 (2×CH), 128.9 (2×CH), 130.0 (CH), 137.2 (C), 138.1 (C), 155.8 (C)

3-((4-Fluorobenzyl)thio)phenol (35). Following the procedure for **34**, 3-mercaptophenol (500 µL, 4.91 mmol) was alkylated with 4-fluorobenzyl bromide (930 mg, 4.92 mmol) to afford **35** (818 mg, 71%) as a colourless solid. ^{1}H NMR (400 MHz, $CDCl_3$) δ 4.08 (s, 2H), 4.68 (br. s, 1H), 6.65 (ddd, J 8.1, 2.5 and 0.9 Hz, 1H), 6.77 (ddd, J = 2.5, 1.7 and 0.3 Hz, 1H), 6.86 (ddd, J = 7.8, 1.7 and 0.9 Hz, 1H), 6.94–7.00 (m, 2H), 7.13 (td, J = 7.9 and 0.3 Hz, 1H), 7.23–7.28 (m, 2H). ^{13}C NMR (101 MHz, $CDCl_3$) δ 38.1 (CH_2), 113.7 (CH), 115.5 (d, J = 21.5 Hz, 2×CH), 116.4 (CH), 122.1 (CH), 130.1 (CH), 130.5 (d, J = 8.1 Hz, 2×CH), 133.1 (d, J = 3.2 Hz, C), 137.8 (C), 155.7 (C), 162.1 (d, J = 245.7 Hz, C). ^{19}F NMR (376 MHz, $CDCl_3$) δ –115.3.

3-((4-Chlorobenzyl)thio)phenol (36). Following the procedure for **34**, 3-mercaptophenol (500 µL, 4.91 mmol) was alkylated with 4-chlorobenzyl chloride (823 mg, 5.11 mmol) to afford **36** (969 mg, 79%) as a colourless solid. ^{1}H NMR (400 MHz, $CDCl_3$) δ 4.06 (s, 2H), 4.72 (br. s, 1H), 6.65 (ddd, J = 8.1, 2.5 and 0.9 Hz, 1H), 6.76 (app. t, J = 2.1 Hz, 1H), 6.86 (ddd, J = 7.8, 1.7 and 0.9 Hz, 1H), 7.13 (app. t, J = 7.9 Hz, 1H), 7.21–7.27 (m, 4H). ^{13}C NMR (101 MHz, $CDCl_3$) δ 38.2 (CH_2), 113.8 (CH), 116.4 (CH), 122.2 (CH), 128.8 (2×CH), 130.1 (CH), 130.2 (2×CH), 133.1 (C), 135.9 (C), 137.5 (C), 155.7 (C).

4-((3-(Benzyloxy)phenoxy)methyl)benzaldehyde (37). To a solution of **25** (328 mg, 1.64 mmol) in anhydrous DMF (6 mL) under argon was added NaH (60% w/w in mineral oil; 83.0 mg,

2.08 mmol). The mixture was sonicated for 2 min to aid dispersal of the hydride reagent and then stirred at ambient temperature for 15 min prior to addition of 4-(bromomethyl)benzaldehyde (365 mg, 1.83 mmol). After a further 16 h the mixture was evaporated to dryness (65 °C / 15 mbar). The resulting residue was taken up in CH_2Cl_2 (20 mL) and filtered through Celite®, washing well with $CHCl_3$. The filtrate was evaporated to dryness and pumped to remove residual DMF. Chromatographic processing of the residue (20 g Strata® SI-1 cartridge; 1 : 49.5 : 49.5 Et_2O/CH_2Cl_2/light petroleum) afford **37** (461 mg, 88%) as a colourless solid. ^{1}H NMR (300 MHz, $CDCl_3$) δ 5.06 (s, 2H), 5.13 (s, 2H), 6.59–6.66 (m, 3H), 7.19–7.24 (m, 1H), 7.31–7.46 (m, 5H), 7.57–7.62 (AA'BB' m, 2H), 7.89–7.92 (AA'BB' m, 2H), 10.03 (s, 1H). ^{13}C NMR (75 MHz, $CDCl_3$) δ 69.0 (CH_2), 69.9 (CH_2), 102.2 (CH), 107.3 (CH), 107.5 (CH), 127.3 (2×CH), 127.4 (2×CH), 127.9 (CH), 128.5 (2×CH), 129.8 (2×CH), 130.0 (CH), 135.8 (C), 136.8 (C), 143.8 (C), 159.5 (C), 160.0 (C), 191.7 (CH).

4-((3-((2-Fluorobenzyl)oxy)phenoxy)methyl)benzaldehyde (38). Following the procedure for **37**, phenol **26** (333 mg, 1.53 mmol) was alkylated to give **38** (317 mg, 62%) as a colourless solid. ^{1}H NMR (300 MHz, $CDCl_3$) δ 5.12 (s, 2H), 5.14 (s, 2H), 6.58–6.66 (m, 3H), 7.08 (ddd, J = 9.9, 8.4 and 1.3 Hz, 1H), 7.16 (td, J = 7.5 and 1.2, 1H), 7.18–7.24 (m, 1H), 7.28–7.36 (m, 1H), 7.47–7.52 (m, 1H), 7.57–7.61 (AA'BB' m, 2H), 7.88–7.92 (AA'BB' m, 2H), 10.03 (s, 1H). ^{13}C NMR (75 MHz, $CDCl_3$) δ 63.8 (d, J = 4.5 Hz, CH_2), 69.3 (CH_2), 102.3 (CH), 107.6 (CH), 107.7 (CH), 115.4 (d, J = 21.0 Hz, CH), 124.1 (d, J = 14.3 Hz, C), 124.3 (d, J = 3.7 Hz, CH), 127.5 (2×CH), 129.77 (CH), 129.84 (d, J = 4.1, CH), 130.1 (2×CH), 130.2 (CH), 136.0 (C), 144.0 (C), 159.7 (C), 159.9 (C), 160.5 (d, J = 246.9 Hz, C), 191.9 (CH). ^{19}F NMR (282 MHz, $CDCl_3$) δ –118.6.

4-((3-((3-Fluorobenzyl)oxy)phenoxy)methyl)benzaldehyde (39). Following the procedure for **37**, phenol **27** (325 mg, 1.49 mmol) was alkylated to give **39** (322 mg, 64%) as a colourless solid. ^{1}H NMR (400 MHz, $CDCl_3$) δ 5.04 (s, 2H), 5.13 (s, 2H), 6.59–6.62 (m, 3H), 7.99–7.04 (m, 1H), 7.13–7.23 (m, 3H), 7.34 (td, J = 7.9 and 5.8 Hz, 1H), 7.57–7.61 (AA'BB' m, 2H), 7.89–7.92 (AA'BB' m, 2H), 10.03 (s, 1H). ^{13}C NMR (101 MHz, $CDCl_3$) δ 69.3 (d, J = 2.0 Hz, CH_2), 69.4 (CH_2), 102.6 (CH), 107.7 (CH), 107.8 (CH), 114.3 (d, J = 22.1 Hz, CH), 114.9 (d, J = 21.2 Hz, CH), 122.8 (d, J = 2.9 Hz, CH), 127.5 (2×CH), 130.1 (2×CH), 130.20 (d, J = 8.1, CH), 130.1 (CH), 136.1 (C), 139.7 (d, J = 7.3 Hz, C), 144.0 (C), 159.8 (C), 159.9 (C), 163.1 (d, J = 246.2 Hz, C), 191.8 (CH). ^{19}F NMR (376 MHz, $CDCl_3$) δ –112.6.

4-((3-((4-Fluorobenzyl)oxy)phenoxy)methyl)benzaldehyde (40). Following the procedure for **37**, phenol **28** (325 mg, 1.49 mmol) was alkylated to give **40** (388 mg, 77%) as a colourless solid. ^{1}H NMR (300 MHz, $CDCl_3$) δ 5.00 (s, 2H), 5.13 (s, 2H), 6.58–6.63 (m, 3H), 7.03–7.11 (m, 2H), 7.17–7.24 (m, 1H), 7.36–7.43 (m, 2H), 7.56–7.62 (AA'BB' m, 2H), 7.88–7.92 (AA'BB' m, 2H), 10.02 (s, 1H). ^{13}C NMR (75 MHz, $CDCl_3$) δ 69.1 (CH_2), 69.2 (CH_2), 102.3 (CH), 107.4 (CH), 107.6 (CH), 115.4 (d, J = 21.0 Hz, 2×CH), 127.4 (2×CH), 129.3 (d, J = 7.7 Hz, 2×CH), 129.9 (2×CH), 130.1 (CH), 132.6 (d, J = 3.3 Hz, C), 135.9 (C), 143.8 (C), 159.6 (C), 159.9 (C), 162.4 (d, J = 247 Hz, C), 191.7 (CH). ^{19}F NMR (282 MHz, $CDCl_3$) δ –113.9.

4-((3-((2-Chlorobenzyl)oxy)phenoxy)methyl)benzaldehyde (41). Following the procedure for **37**, phenol **29** (352 mg, 1.50 mmol) was alkylated to give **41** (374 mg, 71%) as a colourless solid. ^{1}H NMR (300 MHz, $CDCl_3$) δ 5.14 (s, 2H), 5.15 (s, 2H), 6.59–6.66 (m, 3H), 7.19–7.32 (m, 3H), 7.31–7.43 (m, 1H), 7.53–7.56 (m, 1H), 7.57–7.61 (AA'BB' m, 2H), 7.88–7.92 (AA'BB' m, 2H), 10.03 (s, 1H). ^{13}C NMR (75 MHz, $CDCl_3$) δ 67.2 (CH_2), 69.3 (CH_2), 102.3 (CH),

107.6 (CH), 107.8 (CH), 127.0 (CH), 127.5 (2×CH), 128.9 (CH), 129.1 (CH), 129.4 (CH), 130.1 (2×CH), 130.2 (CH), 132.6 (C), 134.6 (C), 136.0 (C), 144.0 (C), 159.7 (C), 159.9 (C), 191.9 (CH).

4-((3-((3-Chlorobenzyl)oxy)phenoxy)methyl)benzaldehyde (42). Following the procedure for **37**, phenol **30** (348 mg, 1.48 mmol) was alkylated to give **42** (286 mg, 55%) as a colourless solid. ^{1}H NMR (300 MHz, $CDCl_3$) δ 5.02 (s, 2H), 5.13 (s, 2H), 6.58–6.62 (m, 3H), 7.17–7.23 (m, 1H), 7.27–7.34 (m, 3H), 7.41–7.44 (m, 1H), 7.57–7.61 (AA'BB' m, 2H), 7.88–7.92 (AA'BB' m, 2H), 10.03 (s, 1H). ^{13}C NMR (75 MHz, $CDCl_3$) δ 69.1 (CH_2), 69.2 (CH_2), 102.3 (CH), 107.6 (2×CH), 125.4 (CH), 127.39 (CH), 127.44 (2×CH), 128.1 (CH), 129.9 (CH), 130.0 (2×CH), 130.2 (CH), 134.5 (C), 136.0 (C), 139.0 (C), 143.9 (C), 159.6 (C), 159.8 (C), 191.8 (CH).

4-((3-((4-Chlorobenzyl)oxy)phenoxy)methyl)benzaldehyde (43). Following the procedure for **37**, phenol **31** (331 mg, 1.41 mmol) was alkylated to give **43** (476 mg, 96%) as a colourless solid. ^{1}H NMR (300 MHz, $CDCl_3$) δ 5.01 (s, 2H), 5.13 (s, 2H), 6.58–6.61 (m, 3H), 7.17–7.23 (m, 1H), 7.35 (app. s, 4H), 7.56–7.61 (AA'BB' m, 2H), 7.88–7.92 (AA'BB' m, 2H), 10.03 (s, 1H). ^{13}C NMR (75 MHz, $CDCl_3$) δ 69.18 (CH_2), 69.20 (CH_2), 102.3 (CH), 107.5 (CH), 107.6 (CH), 127.4 (2×CH), 128.74 (2×CH), 128.78 (2×CH), 130.0 (2×CH), 130.1 (CH), 133.7 (C), 135.4 (C), 135.9 (C), 143.9 (C), 159.6 (C), 159.8 (C), 191.8 (CH).

4-((3-((4-Methoxybenzyl)oxy)phenoxy)methyl)benzaldehyde (44). Following the procedure for **37**, phenol **32** (250 mg, 1.09 mmol) was alkylated to give **44** (256 mg, 68%) as a colourless solid. ^{1}H NMR (300 MHz, $CDCl_3$) δ 3.82 (s, 3H), 4.97 (s, 2H), 5.13 (s, 2H), 6.56–6.64 (m, 3H), 6.89–6.94 (AA'BB' m, 2H), 7.17–7.22 (m, 1H), 7.31–7.37 (AA'BB' m, 2H), 7.56–7.61 (AA'BB' m, 2H), 7.88–7.92 (AA'BB' m, 2H), 10.02 (s, 1H). ^{13}C NMR (75 MHz, $CDCl_3$) δ 55.4 (CH_3), 69.3 (CH_2), 70 (CH_2), 102.4 (CH), 107.4 (CH), 107.8 (CH), 114.2 (2×CH), 127.6 (2×CH),

129.0 (C), 129.4 (2×CH), 130.2 (3×CH), 136.1 (C), 144.1 (C), 159.6 (C), 159.7 (C), 160.3 (C), 192.0 (CH).

4-((3-((4-Formylbenzyl)oxy)phenoxy)methyl)benzonitrile (45). Following the procedure for **37**, phenol **33** (357 mg, 1.59 mmol) was alkylated to give **45** (520 mg, 95%) as a colourless solid. ^{1}H NMR (300 MHz, $CDCl_3$) δ 5.01 (s, 2H), 5.13 (s, 2H), 6.57–6.30 (m, 3H), 7.17–7.25 (m, 1H), 7.51–7.55 (AA'BB' m, 2H), 7.56–7.61 (AA'BB' m, 2H), 7.65–7.69 (AA'BB' m, 2H), 7.88–7.92 (AA'BB' m, 2H), 10.02 (s, 1H). ^{13}C NMR (75 MHz, $CDCl_3$) δ 68.9 (CH_2), 69.2 (CH_2), 102.3 (CH), 107.5 (CH), 107.7 (CH), 111.6 (C), 118.7 (C), 127.4 (2×CH), 127.5 (2×CH), 130.0 (2×CH), 130.2 (CH), 132.3 (2×CH), 135.9 (C), 142.3 (C), 143.8 (C), 159.4 (C), 159.6 (C), 191.8 (CH).

4-((3-(Benzylthio)phenoxy)methyl)benzaldehyde (46). Following the procedure for **22**, 4-(bromomethyl)benzaldehyde (301 mg, 1.51 mmol) and phenol **34** (336 mg, 1.55 mmol) gave **46** (401 mg, 79%) as a colourless oil. ^{1}H NMR (400 MHz, $CDCl_3$) δ 4.11 (s, 2H), 5.07 (s, 2H), 6.78 (ddd, J = 8.3, 2.5 and 0.8 Hz, 1H), 6.89 (app. t, J = 2.1 Hz, 1H), 6.94 (ddd, J = 7.7, 1.6 and 0.9 Hz, 1H), 7.18 (t, J = 8.0 Hz, 1H), 7.22–7.31 (m, 5H), 7.55–7.58 (AA'BB' m, 2H), 7.89–7.91 (AA'BB' m, 2H), 10.03 (s, 1H). ^{13}C NMR (101 MHz, $CDCl_3$) δ 38.9 (CH_2), 69.3 (CH_2), 113.1 (CH), 115.8 (CH), 122.4 (CH), 127.4 (CH), 127.6 (2×CH), 128.7 (2×CH), 129.0 (2×CH), 129.9 (CH), 130.2 (2×CH), 136.1 (C), 137.4 (C), 138.2 (C), 143.9 (C), 158.6 (C), 191.9 (CH).

4-((3-((4-Fluorobenzyl)thio)phenoxy)methyl)benzaldehyde (47). Following the procedure for **22**, 4-(bromomethyl)benzaldehyde (301 mg, 1.51 mmol) and phenol **35** (398 mg, 1.70 mmol) gave **47** (495 mg, 93%) as a colourless oil. ^{1}H NMR (400 MHz, $CDCl_3$) δ 4.07 (s, 2H), 5.09 (s, 2H), 6.79 (ddd, J = 8.3, 2.5 and 0.8 Hz, 1H), 6.88 (app. t, J = 2.1 Hz, 1H), 6.92 (ddd, J = 7.7, 1.7 and 0.9 Hz, 1H), 6.93–6.99 (m, 2H), 7.19 (t, J = 8.0 Hz, 1H), 7.21–7.26 (m, 2H), 7.55–

7.58 (AA'BB' m, 2H), 7.89–7.92 (AA'BB' m, 2H), 10.03 (s, 1H). ^{13}C NMR (101 MHz, $CDCl_3$) δ 38.1 (CH_2), 69.3 (CH_2), 113.1 (CH), 115.4 (d, J = 21.5 Hz, 2×CH), 116.0 (CH), 122.6 (CH), 127.5 (2×CH), 129.9 (CH), 130.1 (2×CH), 130.4 (d, J = 8.1 Hz, 2×CH), 133.1 (d, J = 3.2 Hz, C), 136.1 (C), 137.7 (C), 158.6 (C), 162.1 (d, J = 245.8 Hz, C), 191.9 (CH). ^{19}F NMR (376 MHz, $CDCl_3$) δ –115.2.

4-((3-((4-Chlorobenzyl)thio)phenoxy)methyl)benzaldehyde (48). Following the procedure for **22**, 4-(bromomethyl)benzaldehyde (300 mg, 1.51 mmol) and phenol **36** (423 mg, 1.69 mmol) gave **48** (468 mg, 84%) as a colourless oil. ^{1}H NMR (400 MHz, $CDCl_3$) δ 4.05 (s, 2H), 5.07 (s, 2H), 6.79 (ddd, J = 8.3, 2.5 and 0.8 Hz, 1H), 6.86 (app. t, J = 2.1 Hz, 1H), 6.92 (ddd, J = 7.7, 1.6 and 0.9 Hz, 1H), 7.15–7.26 (m, 5H), 7.55–7.58 (AA'BB' m, 2H), 7.89–7.91 (AA'BB' m, 2H), 10.03 (s, 1H).. ^{13}C NMR (101 MHz, $CDCl_3$) δ 38.1 (CH_2), 69.2 (CH_2), 113.2 (CH), 116.1 (CH), 122.7 (CH), 127.5 (2×CH), 128.7 (2×CH), 129.9 (CH), 130.0 (2×CH), 130.2 (2×CH), 133.0 (C), 136.0 (C), 136.1 (C), 137.4 (C), 143.7 (C), 158.6 (C), 191.8 (CH).

(*R*)-(1-(4-((3-(Benzyloxy)phenoxy)methyl)benzyl)pyrrolidin-2-yl)methanol (49). To a stirred solution of **37** (254 mg, 797 μmol) and (*R*)-prolinol (170 mg, 1.68 mmol) in anhydrous THF (15 mL) under argon was added $NaBH(OAc)_3$ (347 mg, 1.64 mol). The mixture was sonicated, at ambient temperature for 3 h. A further portion of $NaBH(OAc)_3$ (214 mg, 1.01 mmol) was then added and sonication of the turbid mixture continued for 40 min. The mixture was stirred for 12 h, then diluted with 2 M NaOH (aq) (40 mL), vortexing thoroughly, and extracted with $CHCl_3$ (250 mL). The extract was dried ($MgSO_4$), evaporated and the residue processed chromatographically (20 g Strata® SI-1 cartridge; 2.5% MeOH/$CHCl_3$). Target material eluted first, with *N*-acetylprolinol[55] overlapping in tail fractions. Fractions containing clean target material were combined and evaporated to afford **49** (225 mg, 70%) as a colourless oil that became

an amorphous solid on standing. ^{1}H NMR (400 MHz, $CDCl_3$) δ 1.66–1.75 (m, 2H), 1.83–2.00 (m, 2H), 2.30 (td, J = 9.3 and 7.5 Hz, 1H), 2.50–3.00 (br. s, 1H), 2.72–2.77 (m, 1H), 2.97–3.01 (m, 1H), 3.38 (d, J = 13.1 Hz, 1H), 3.44 (dd, J = 10.8 and 2.1 Hz, 1H), 3.67 (dd, J = 10.7 and 3.5 Hz, 1H), 3.98 (d, J = 13.1 Hz, 1H), 5.02 (s, 2H), 5.05 (s, 2H), 6.59–6.62 (m, 2H), 6.64 (t, J = 2.2 Hz, 1H), 7.17–7.21 (m, 1H), 7.31–7.35 (m, 3H), 7.37–7.45 (m, 6H). ^{13}C NMR (101 MHz, $CDCl_3$) δ 23.5 (CH_2), 27.9 (CH_2), 54.5 (CH_2), 58.4 (CH_2), 62.1 (CH_2), 64.5 (CH), 69.9 (CH_2), 70.1 (CH_2), 102.4 (CH), 107.5 (2×CH), 127.5 (2×CH), 127.6 (2×CH), 128.0 (CH), 128.6 (2×CH), 128.9 (2×CH), 130.0 (CH), 135.8 (C), 137.1 (C), 139.2 (C), 160.2 (2×C). ESI-HRMS $[M + H]^+$ calcd for $C_{26}H_{30}NO_3^+$, 404.2220; found, 404.2203. HPLC: Method (A) t_R 4.56 min (97.7%). [Tail fractions from the chromatographic isolation of the product were combined separately to afford a second batch (76.5 mg) of **53** contaminated with 12 mol% *N*-acetylprolinol, giving a total target material recovery of 93%.]

(*R*)-(1-(4-((3-((2-Fluorobenzyl)oxy)phenoxy)methyl)benzyl)pyrrolidin-2-yl)methanol (50). Following the procedure for **49**, aldehyde **38** (261 mg, 776 μmol) afforded **50** (226 mg, 69%) as a colourless oil that became an amorphous solid on standing. ^{1}H NMR (400 MHz, $CDCl_3$) δ 1.65–1.76 (m, 2H), 1.80–1.99 (m, 2H), 2.30 (td, J = 9.2 and 7.6 Hz, 1H), 2.50–3.00 (br. s, 1H), 2.72–2.77 (m, 1H), 2.96–3.01 (m, 1H), 3.38 (d, J = 13.1 Hz, 1H), 3.44 (dd, J = 10.8 and 2.1 Hz, 1H), 3.67 (dd, J = 10.8 and 3.5 Hz, 1H), 3.98 (d, J = 13.1 Hz, 1H), 5.03 (s, 2H), 5.12 (s, 2H), 6.60–6.63 (m, 2H), 6.65 (t, J = 2.3 Hz, 1H), 7.09 (ddd, J = 9.9, 8.4 and 1.3 Hz, 1H), 7.16 (td, J = 7.5 and 1.2, 1H), 7.20 (t, J = 8.2, 1H), 7.21–7.23 (m, 3H), 7.37–7.40 (AA'BB' m, 2H), 7.48–7.53 (m, 1H). ^{13}C NMR (101 MHz, $CDCl_3$) δ 23.5 (CH_2), 27.9 (CH_2), 54.5 (CH_2), 58.4 (CH_2), 62.0 (CH_2), 63.8 (d, J = 4.4 Hz, CH_2), 64.5 (CH), 70.0 (CH_2), 102.4 (CH), 107.5 (CH), 107.8 (CH), 115.4 (d, J = 21.2 Hz, CH), 124.27 (d, J = ca.14 Hz, C), 124.30 (d, J = 3.6 Hz, CH), 127.7 (2×CH), 129.0

(2×CH), 129.7 (d, J = 8.7 Hz, CH), 129.8 (d, J = 4.1 Hz, CH), 130.0 (CH), 135.8 (C), 139.3 (C), 159.9 (C), 160.2 (C), 160.5 (d, J = 246.9 Hz, C). ^{19}F NMR (376 MHz, $CDCl_3$) δ −118.6. ESI-HRMS $[M + H]^+$ calcd for $C_{26}H_{29}FNO_3^+$, 422.2126 found, 422.2106. HPLC: Method (A) t_R 4.62 min (97.0%).

(*R*)-(1-(4-((3-((3-Fluorobenzyl)oxy)phenoxy)methyl)benzyl)pyrrolidin-2-yl)methanol (51). Following the procedure for **49**, aldehyde **39** (258 mg, 768 μmol) afforded **51** (185 mg, 57%) as a colourless oil. ^{1}H NMR (400 MHz, $CDCl_3$) δ 1.64–1.76 (m, 2H), 1.80–1.99 (m, 2H), 2.30 (td, J = 9.3 and 7.5 Hz, 1H), 2.40–2.90 (br. s, 1H), 2.72–2.77 (m, 1H), 2.96–3.01 (m, 1H), 3.38 (d, J = 13.1 Hz, 1H), 3.44 (dd, J = 10.7 and 1.8 Hz, 1H), 3.67 (dd, J = 10.8 and 3.5 Hz, 1H), 3.98 (d, J = 13.1 Hz, 1H), 5.02 (s, 2H), 5.04 (s, 2H), 6.57–6.63 (m, 3H), 6.98–7.04 (m, 1H), 7.13–7.21 (m, 3H), 7.30–7.40 (m, 5H). ^{13}C NMR (101 MHz, $CDCl_3$) δ 23.5 (CH_2), 27.9 (CH_2), 54.6 (CH_2), 58.4 (CH_2), 62.1 (CH_2), 64.5 (CH), 69.3 (CH_2), 70.0 (CH_2), 102.5 (CH), 107.5 (CH), 107.8 (CH), 114.3 (d, J = 21.9 Hz, CH), 114.8 (d, J = 21.2 Hz, CH), 122.8 (d, J = 2.9 Hz, CH), 127.7 (2×CH), 129.0 (2×CH), 130.1 (CH), 130.2 (d, J = 8.2 Hz, CH), 135.8 (C), 139.3 (C), 139.8 (d, J = 7.3 Hz, C), 159.9 (C), 160.2 (C), 163.1 (d, J = 246.1 Hz, C). ^{19}F NMR (376 MHz, $CDCl_3$) δ −112.7. ESI-HRMS $[M + H]^+$ calcd for $C_{26}H_{29}FNO_3^+$, 422.2126 found, 422.2106. HPLC: Method (A) t_R 4.67 min (> 99%).

(*R*)-(1-(4-((3-((4-Fluorobenzyl)oxy)phenoxy)methyl)benzyl)pyrrolidin-2-yl)methanol (52). Following the procedure for **49**, aldehyde **40** (263 mg, 783 μmol) afforded **52** (239 mg, 73%) as a colourless oil. ^{1}H NMR (400 MHz, $CDCl_3$) δ 1.66–1.75 (m, 2H), 1.80–1.99 (m, 2H), 2.30 (td, J = 9.3 and 7.5 Hz, 1H), 2.50–3.00 (br. s, 1H), 2.72–2.77 (m, 1H), 2.96–3.01 (m, 1H), 3.38 (d, J = 13.1 Hz, 1H), 3.44 (dd, J = 10.8 and 2.1 Hz, 1H), 3.67 (dd, J = 10.8 and 3.5 Hz, 1H), 3.98 (d, J = 13.1 Hz, 1H), 5.00 (s, 2H), 5.02 (s, 2H), 6.57–6.62 (m, 3H), 7.04–7.10 (m, 2H), 7.17–7.22 (m,

1H), 7.30–7.34 (AA'BB' m, 2H), 7.37–7.42 (m, 4H). ^{13}C NMR (101 MHz, $CDCl_3$) δ 23.5 (CH_2), 27.9 (CH_2), 54.5 (CH_2), 58.4 (CH_2), 62.1 (CH_2), 64.5 (CH), 69.4 (CH_2), 70 (CH_2), 102.5 (CH), 107.5 (CH), 107.6 (CH), 115.5 (d, J = 21.5 Hz, 2×CH), 127.6 (2×CH), 129.0 (2×CH), 129.3 (d, J = 8.2 Hz, 2×CH), 130.0 (CH), 132.9 (d, J = 2.9 Hz, C), 135.8 (C), 139.3 (C), 160.0 (C), 160.2 (C), 162.5 (d, J = 246.1 Hz, C). ^{19}F NMR (376 MHz, $CDCl_3$) δ –114.27. ESI-HRMS $[M + H]^+$ calcd for $C_{26}H_{29}FNO_3^+$, 422.2126; found, 422.2105. HPLC: Method (A) t_R 4.56 min (> 99%).

(*R*)-(1-(4-((3-((2-Chlorobenzyl)oxy)phenoxy)methyl)benzyl)pyrrolidin-2-yl)methanol (53). Following the procedure for **49**, aldehyde **41** (270 mg, 765 μmol) afforded **53** (196 mg, 58%) as a colourless oil. ^{1}H NMR (400 MHz, $CDCl_3$) δ 1.64–1.76 (m, 2H), 1.80–1.99 (m, 2H), 2.29 (td, J = 9.3 and 7.6 Hz, 1H), 2.50–3.00 (br. s, 1H), 2.72–2.77 (m, 1H), 2.96–3.01 (m, 1H), 3.37 (d, J = 13.1 Hz, 1H), 3.44 (dd, J = 10.7 and 1.7 Hz, 1H), 3.67 (dd, J = 10.7 and 3.5 Hz, 1H), 3.98 (d, J = 13.1 Hz, 1H), 5.03 (s, 2H), 5.15 (s, 2H), 6.60–6.32 (m, 2H), 6.65 (t, J = 2.2 Hz, 1H), 7.18–7.22 (m, 1H), 7.24–7.29 (m, 2H), 7.30–7.33 (AA'BB' m, 2H), 7.37–7.41 (m overlapping AA'BB' m, 3H), 7.54–7.57 (m, 1H). ^{13}C NMR (101 MHz, $CDCl_3$) δ 23.5 (CH_2), 27.9 (CH_2), 54.5 (CH_2), 58.4 (CH_2), 62.0 (CH_2), 64.5 (CH), 67.3 (CH_2), 70.0 (CH_2), 102.5 (CH), 107.6 (CH), 107.7 (CH), 127.0 (CH), 127.7 (2×CH), 128.9 (CH), 128.96 (2×CH), 128.99 (CH), 129.4 (CH), 130.0 (CH), 132.6 (C), 134.8 (C), 135.8 (C), 139.3 (C), 159.9 (C), 160.2 (C). ESI-HRMS $[M + H]^+$ calcd for $C_{26}H_{29}ClNO_3^+$, 438.1831 found, 438.1830. HPLC: Method (A) t_R 5.00 min (> 99%).

(*R*)-(1-(4-((3-((3-Chlorobenzyl)oxy)phenoxy)methyl)benzyl)pyrrolidin-2-yl)methanol (54). Following the procedure for **49**, aldehyde **42** (253 mg, 718 μmol) afforded **54** (158 mg, 50%) as a colourless oil. ^{1}H NMR (400 MHz, $CDCl_3$) δ 1.63–1.77 (m, 2H), 1.79–2.01 (m, 2H), 2.30 (td, J = 9.2 and 7.5 Hz, 1H), 2.50–3.00 (br. s, 1H), 2.71–2.78 (m, 1H), 2.95–3.02 (m, 1H), 3.38 (d, J = 13.1 Hz, 1H), 3.44 (dd, J = 10.8 and 1.9 Hz, 1H), 3.67 (dd, J = 10.7 and 3.5 Hz, 1H), 3.98 (d, J =

13.1 Hz, 1H), 5.01 (s, 2H), 5.02 (s, 2H), 6.56–6.63 (m, 3H), 7.17–7.22 (m, 1H), 7.28–7.34 (m, 5H), 7.36–7.40 (AA'BB' m, 2H), 7.42–7.44 (m, 1H). ^{13}C NMR (101 MHz, $CDCl_3$) δ 23.6 (CH_2), 27.9 (CH_2), 54.6 (CH_2), 58.4 (CH_2), 62.0 (CH_2), 64.5 (CH), 69.3 (CH_2), 70.0 (CH_2), 102.5 (CH), 107.5 (CH), 107.8 (CH), 125.4 (CH), 127.5 (CH), 127.7 (2×CH), 128.2 (CH), 129.0 (2×CH), 129.9 (CH), 130.1 (CH), 134.6 (C), 135.8 (C), 139.2 (C), 139.4 (C), 159.9 (C), 160.2 (C). ESI-HRMS $[M + H]^+$ calcd for $C_{26}H_{29}ClNO_3^+$, 438.1831 found, 438.1808. HPLC: Method (A) t_R 5.03 min (> 99%).

(*R*)-(1-(4-((3-((4-Chlorobenzyl)oxy)phenoxy)methyl)benzyl)pyrrolidin-2-yl)methanol (55). Following the procedure for **49**, aldehyde **43** (267 mg, 757 μmol) afforded **55** (286 mg, 86%) as a colourless oil that became an amorphous solid on standing. ^{1}H NMR (400 MHz, $CDCl_3$) δ 1.66–1.74 (m, 2H), 1.81–2.00 (m, 2H), 2.30 (td, J = 9.3 and 7.5 Hz, 1H), 2.60–2.95 (br. s, 1H), 2.72–2.77 (m, 1H), 2.97–3.01 (m, 1H), 3.38 (d, J = 13.1 Hz, 1H), 3.45 (dd, J = 10.8 and 2.0 Hz, 1H), 3.67 (dd, J = 10.7 and 3.5 Hz, 1H), 3.98 (d, J = 13.1 Hz, 1H), 5.00 (s, 2H), 5.02 (s, 2H), 6.58 (dd, J = 8.2, 2.3 and 0.9 Hz, 1H), 6.60–6.63 (m, 2H), 7.17–7.22 (m, 1H), 7.30–7.41 (m, 8H). ^{13}C NMR (75 MHz, $CDCl_3$) δ 23.5 (CH_2), 27.8 (CH_2), 54.5 (CH_2), 58.3 (CH_2), 61.9 (CH_2), 64.4 (CH), 69.2 (CH_2), 69.9 (CH_2), 102.3 (CH), 107.4 (CH), 107.6 (CH), 127.7 (2×CH), 128.78 (2×CH), 128.82 (2×CH), 129.0 (2×CH), 130.0 (CH), 133.8 (C), 135.5 (C), 135.7 (C), 139.3 (C), 159.8 (C), 160.1 (C). ESI-HRMS $[M + H]^+$ calcd for $C_{26}H_{29}ClNO_3^+$, 438.1831; found, 438.1808. HPLC: Method (A) t_R 5.15 min (97.8%).

(*R*)-(1-(4-((3-((4-methoxybenzyl)oxy)phenoxy)methyl)benzyl)pyrrolidin-2-yl)methanol (56). Following the procedure for **49**, aldehyde **44** (256 mg, 735 μmol) afforded **56** (266 mg, 84%) as a colourless oil that became an amorphous solid on standing. ^{1}H NMR (300 MHz, $CDCl_3$) δ 1.65–1.75 (m, 2H), 1.79–2.01 (m, 2H), 2.30 (td, J = 9.2 and 7.6 Hz, 1H), 2.50–

3.00 (br. s, 1H), 2.71–2.77 (m, 1H), 2.95–3.02 (m, 1H), 3.38 (d, J = 13.1 Hz, 1H), 3.44 (dd, J = 10.8 and 2.1 Hz, 1H), 3.67 (dd, J = 10.8 and 3.5 Hz, 1H), 3.82 (s, 3H), 3.98 (d, J = 13.1 Hz, 1H), 4.96 (s, 2H), 5.02 (s, 2H), 6.58–6.64 (m, 3H), 6.90–6.94 (AA'BB' m, 2H), 7.19 (t, J = 8.2 Hz, 1H), 7.31–7.40 (m, 6H). ^{13}C NMR (75 MHz, $CDCl_3$) δ 23.5 (CH_2), 27.8 (CH_2), 54.5 (CH_2), 55.4 (CH_3), 58.3 (CH_2), 61.9 (CH_2), 64.4 (CH), 69.86 (CH_2), 69.88 (CH_2), 102.3 (CH), 107.4 (CH), 107.5 (CH), 114.1 (2×CH), 127.7 (2×CH), 128.97 (2×CH), 129.01 (C), 129.3 (2×CH), 130.0 (CH), 135.8 (C), 139.2 (C), 159.5 (C), 160.1 (C), 160.2 (C). ESI-HRMS $[M + H]^+$ calcd for $C_{27}H_{32}NO_4^+$, 434.2326; found, 434.2304. HPLC: Method (A) t_R 4.61 min (97.5%).

(*R*)-4-((3-((4-((2-(hydroxymethyl)pyrrolidin-1-yl)methyl)benzyl)oxy)phenoxy)methyl)benzonitrile (57). Following the procedure for **49**, aldehyde **45** (264 mg, 768 μmol) afforded **57** (124 mg, 38%) as a colourless oil that became an amorphous solid on standing. ^{1}H NMR (400 MHz, $CDCl_3$) δ 1.65–1.76 (m, 2H), 1.80–1.99 (m, 2H), 2.30 (td, J = 9.3 and 7.5 Hz, 1H), 2.50–3.00 (br. s, 1H), 2.72–2.77 (m, 1H), 2.96–3.01 (m, 1H), 3.38 (d, J = 13.1 Hz, 1H), 3.43 (dd, J = 10.8 and 2.0 Hz, 1H), 3.66 (dd, J = 10.8 and 3.5 Hz, 1H), 3.97 (d, J = 13.1 Hz, 1H), 5.02 (s, 2H), 5.10 (s, 2H), 6.56 (ddd, J = 8.2, 2.4 and 0.8 Hz, 1H), 6.60 (t, J = 2.2 Hz, 1H), 6.62 (ddd, J = 8.2, 2.4 and 0.8 Hz, 1H), 7.18–7.22 (m, 1H), 7.31–7.39 (tight AA'BB' m, 4H), 7.52–7.54 (AA'BB' m, 2H), 7.66–7.69 (AA'BB' m, 2H). ^{13}C NMR (101 MHz, $CDCl_3$) δ 23.5 (CH_2), 27.8 (CH_2), 54.5 (CH_2), 58.4 (CH_2), 62.0 (CH_2), 64.4 (CH), 69.0 (CH_2), 70.0 (CH_2), 102.5 (CH), 107.4 (CH), 107.9 (CH), 111.7 (C), 118.6 (C), 127.55 (2×CH), 127.58 (2×CH), 128.9 (2×CH), 130.1 (CH), 132.4 (2×CH), 135.6 (C), 139.4 (C), 142.5 (C), 159.5 (C), 160.2 (C). ESI-HRMS $[M + H]^+$ calcd for $C_{27}H_{29}N_2O_3^+$, 429.2173 found, 429.2152. HPLC: Method (A) t_R 4.25 min (99.8%).

(*R*)-(1-(4-((3-(Benzylthio)phenoxy)methyl)benzyl)pyrrolidin-2-yl)methanol (58). Following the procedure for **18**, aldehyde **46** (401 mg, 1.20 mmol) afforded **58** (477 mg, 95%) as a colourless oil that solidified on standing. ^{1}H NMR (400 MHz, $CDCl_3$) δ 1.65–1.76 (m, 2H), 1.81–2.00 (m, 2H), 2.30 (td, J = 9.3 and 7.5 Hz, 1H), 2.50–3.00 (br. s, 1H), 2.72–2.77 (m, 1H), 2.96–3.01 (m, 1H), 3.38 (d, J = 13.1 Hz, 1H), 3.45 (dd, J = 10.8 and 1.8 Hz, 1H), 3.67 (dd, J = 10.7 and 3.5 Hz, 1H), 3.98 (d, J = 13.1 Hz, 1H), 4.11 (s, 2H), 4.97 (s, 2H), 6.80 (dd, J = 8.3, 2.3 and 0.7 Hz, 1H), 6.91–6.93 (m, 2H), 7.17 (app. t, J = 8.2 Hz, 1H), 7.22–7.38 (m, 9H). ^{13}C NMR (101 MHz, $CDCl_3$) δ 23.6 (CH_2), 27.9 (CH_2), 38.9 (CH_2), 54.6 (CH_2), 58.3 (CH_2), 61.9 (CH_2), 64.4 (CH), 69.9 (CH_2), 113.1 (CH), 115.8 (CH), 122.1 (CH), 127.3 (CH), 127.7 (2×CH), 128.6 (2×CH), 128.9 (2×CH), 129.0 (2×CH), 129.8 (CH), 135.6 (C), 137.4 (C), 137.9 (C), 139.4 (C), 159.0 (C). ESI-HRMS $[M + H]^+$ calcd for $C_{26}H_{30}NO_2S^+$, 420.1992; found, 420.1995. HPLC: Method (A) t_R 4.61 min (>99%).

(*R*)-(1-(4-((3-((4-Fluorobenzyl)thio)phenoxy)methyl)benzyl)pyrrolidin-2-yl)methanol (59). Following the procedure for **18**, aldehyde **47** (487 mg, 1.38 mmol) afforded **59** (471 mg, 78%) as a colourless oil. ^{1}H NMR (400 MHz, $CDCl_3$) δ 1.65–1.73 (m, 2H), 1.80–1.99 (m, 2H), 2.29 (td, J = 9.3 and 7.5 Hz, 1H), 2.60–2.85 (br m, 1H), 2.71–2.77 (m, 1H), 2.95–3.01 (m, 1H), 3.37 (d, J = 13.1 Hz, 1H), 3.44 (dd, J = 10.8 and 1.8 Hz, 1H), 3.66 (dd, J = 10.7 and 3.5 Hz, 1H), 3.97 (d, J = 13.1 Hz, 1H), 4.07 (s, 2H), 4.98 (s, 2H), 6.80 (ddd, J = 8.3, 2.3 and 1.1 Hz, 1H), 6.88–6.91 (m, 2H), 6.93–6.99 (m, 2H), 7.15–7.19 (m, 1H), 7.21–7.25 (m, 2H), 7.31–7.37 (tight AA'BB' m, 4H). ^{13}C NMR (101 MHz, $CDCl_3$) δ 23.6 (CH_2), 27.9 (CH_2), 38.3 (CH_2), 54.6 (CH_2), 58.4 (CH_2), 62.0 (CH_2), 64.5 (CH), 70.0 (CH_2), 113.4 (CH), 115.4 (d, J = 21.5 Hz, 2×CH), 116.3 (CH), 122.5 (CH), 127.7 (2×CH), 129.0 (2×CH), 129.8 (CH), 130.5 (d, J = 8.1 Hz, 2×CH), 133.3 (d, J = 2.9 Hz, C), 135.7 (C), 137.5 (C), 139.5 (C), 159.1 (C), 162.2 (d, J = 245.5 Hz, C). ^{19}F NMR (282

MHz, $CDCl_3$) δ –115.2. ESI-HRMS $[M + H]^+$ calcd for $C_{26}H_{29}FNO_2S^+$, 438.1898; found, 438.1891. HPLC: Method (A) t_R 4.94 min (95.4%).

(*R*)-(1-(4-((3-((4-Chlorobenzyl)thio)phenoxy)methyl)benzyl)pyrrolidin-2-yl)methanol (60). Following the procedure for **18**, aldehyde **48** (100 mg, 0.260 mmol) afforded **60** (62 mg, 53%) as a colourless oil. ^{1}H NMR (400 MHz, $CDCl_3$) δ 1.66–1.74 (m, 2H), 1.80–1.99 (m, 2H), 2.29 (td, J = 9.3 and 7.5 Hz, 1H), 2.50–2.85 (br m, 1H), 2.72–2.77 (m, 1H), 2.95–3.00 (m, 1H), 3.38 (d, J = 13.1 Hz, 1H), 3.44 (dd, J = 10.8 and 2.2 Hz, 1H), 3.67 (dd, J = 10.8 and 3.5 Hz, 1H), 3.98 (d, J = 13.1 Hz, 1H), 4.05 (s, 2H), 4.98 (s, 2H), 6.81 (ddd, J = 8.3, 2.4 and 1.1 Hz, 1H), 6.88–6.91 (m, 2H), 7.15–7.22 (m, 3H), 7.23–7.26 (m, 2H), 7.31–7.37 (tight AA'BB' m, 4H). ^{13}C NMR (101 MHz, $CDCl_3$) δ 23.6 (CH_2), 27.9 (CH_2), 38.4 (CH_2), 54.6 (CH_2), 58.4 (CH_2), 62.0 (CH_2), 64.51 (CH), 70.0 (CH_2), 113.5 (CH), 116.4 (CH), 122.6 (CH), 127.7 (2×CH), 128.7 (2×CH), 129.0 (2×CH), 129.9 (CH), 130.2 (2×CH), 133.1 (C), 135.7 (C), 136.2 (C), 137.2 (C), 139.5 (C), 159.2 (C). ESI-HRMS $[M + H]^+$ calcd for $C_{26}H_{29}ClNO_2S^+$, 454.1602; found, 454.1603. HPLC: Method (A) t_R 5.27 min (98.8%).

Molecular modeling. An SK2 homology model was constructed in order to provide a qualitative understanding of ligand selectivity determinants. The preliminary model was generated through the SWISS-MODEL server[47-50] by submission of the SK2 sequence and specification of the SK1/PF-543 co-crystal structure (4V24 chain A, 1.8 Å resolution)[38] as a template. In SK1 a regulatory 'R-loop' (41 residues) is interposed between strands β9/β10 of the CTD and makes no contact with the 3 lipid binding loops that pack to form the J-channel on the opposite face of the CTD core β-sandwich. (See supplementary Figure S1 in Adams *et al*[39] for SK1/SK2 sequence alignment and definition of loops.) The R-loop in SK2 is substantially longer (156 residues) and, in the absence of a suitable template, no attempt was made to model it. Thus, the core of this loop

sequence (SK2 residues 345–488 inclusive) was deleted. The implicit assumption, that the R-loop does not directly impact on the structure of the J-channel heel and toe regions, was deemed reasonable based on the known disposition of the R-loop in SK1 crystal structures. The length of the lipid binding loops is identical for SK1 and SK2 and the loops exhibit a high degree of sequence conservation: LBL-1 (34 residues), 62% identity; LBL-2 (21 residues), 43% identity; LBL-3 (28 residues), 61% identity. Very close structural homology observed between the SK2 model output from the SWISS-MODEL server and the SK1 template was therefore fully reasonable.

The model was refined using the protein preparation and refinement tools in the Small Molecule Drug Discovery (SMDD) software suite from Schrödinger, LLC. Ramachandran plot analysis of the crude model (lacking the R-loop) identified 4 residues (Ser209, Ala523, Thr578, Pro579) with outlier φ and ψ angle combinations. These were considered sufficiently remote from the J-channel to have little bearing on the quality of the model as starting point for refinement. Hydration from the template protein (4V24) was merged into the model together with a J-channel ligand, SKi (**10**), from its co-crystal structure (3VZC, chain A) aligned to the crude model. The latter was selected as a suitable J-channel ligand for refinement work because it inhibits both SK1 and SK2 with little discrimination and because the structure of the SK1 J-channel is conserved when bound by PF-543 or SKi. The hydroxymethyl group of PF-543 mimics the 3-OH of Sph substrate in engaging Asp308 on helix-α7. In its absence, as with bound SKi, the position of the hydroxyl is occupied by a surrogate water, defined as W2 in Figure S3 of Adams *et al*[39]. A water was therefore inserted into the W2 position of the crude model with SKi. The model was manually inspected and waters imported from the 4V24 template that were sterically interdicted were deleted or moved to take account of side chain conformations.

The C-terminal end of the less strongly conserved LBL-2 was remodelled with a template taken from residues 209-PEAQVDDGKLHL-220 in the crystal structure (4WER) of a prokaryotic diacylglycerol kinase family protein. These residues correspond to 521-PHARFDDGLVHL-532 in SK2 and 276-PMGRCAAGVMHL-287 in SK1. In the 4WER structure, the residues in this sequence form a well-defined lariat which is highly conserved across related crystal structures (2BON, 2JGR, 2P1R, 2QV7, 2QVL, 3S40, 3T5P, 4WRR). In several of these the lariat hosts a non-catalytic metal ion by coordination to an aspartate in a DG motif that is conserved in all the structures and also in SK2 but not in SK1. Where present, the metal ion is also coordinated by a conserved aspartate on one of two long crossed β-strands that form the key interdomain connection. This latter residue (Asp281) is also conserved in SK2 but not conserved in SK1, where the cognate residue is Asn151. When the metal ion is absent, a structural water molecule acts as a surrogate through hydrogen bonded interactions, as is the case in the 4WER crystal structure. The metal ion may have a regulatory role in the prokaryotic enzymes.[56,57] At present there is no evidence to support a role for non-catalytic metal ion regulatory control over SK2, and we therefore modelled the SK2 lariat on the metal-free structure of 4WER.

To refine the model, preparation was undertaken with the SMDD protein preparation wizard using default optimisation and restrained minimisation routines. Full OPLS3 force field protein minimisation was then undertaken in iterations, initially with SK1-templated Cartesian constraints on selected residues lining the interdomain cleft, at the interdomain tip interface of LBL-1 and at the hinge of LBL-3. The constraints were defined to restrain interdomain movement and to mimic a helix-capping interaction seen in SK1 crystal structures from Arg291 on LBL-3/helix-α9 (conserved as Arg541 in SK2) to the backbone at the C-terminal end of LBL-1/helix-α8. The constraints were progressively removed following the initial minimisation with the

remodelled LBL-2 loop structure and omitted altogether in the final minimisation. Ramachandran plot analysis of the minimsed model identified no residues with outlier φ and ψ angle combinations. Standard precision (Glide SP) docking routines within SMDD were employed for ligand docking using grids generated with SKi as the binding site identifier. Docked structures were then processed with the SMDD Prime refine protein−ligand complex utility using local optimisation settings within an 8 Å radius of the ligand. In the case of VT20dd (**9**), initial ligand docking was undertaken with the smaller analogue, (protonated) (*S*)-2-((3-(4-((4-(3-(trifluoromethyl)phenyl)thiazol-2-yl)amino)phenyl)-1,2,4-oxadiazol-5-yl)methyl)pyrrolidine-1-carboximidamide (compound **20l** in Childress *et al*),[36] to define a binding mode for the core and polar head group of this SK inhibitor chemotype. The ligand in the resulting model was then rebuilt using the SMDD build tools and subjected to the SMDD Prime refine protein−ligand complex routine.

ASSOCIATED CONTENT

Supporting Information

The Supporting Information is available free of charge on the ACS Publications website at DOI: .

Molecular formula strings with SK1 and SK2 inhibition data (si_01.csv).

Related to Figures 5, 7 and 8, homology model of SK2 with compound **60** (si_02.pdb).

Related to Figure 6, homology model of SK2 with compound **49** (si_03.pdb).

Related to Figure 6, docking model of SK1 (based on crystal structure PDB: 4V24) with compound **49** (si_04.pdb).

Related to Figure 7, docking model of SK1 (based on crystal structure PDB: 4V24) with compound **60** (si_05.pdb).

Related to Figure 8, homology model of SK2 with compound **9** (si_06.pdb).

Related to Figure 8, homology model of SK2 with compound **10** (si_07.pdb).

Reference NMR spectra for key compounds (si_08.pdf)

AUTHOR INFORMATION

Corresponding Author

*E-mail: susan.pyne@strath.ac.uk. Tel: +44(0)141 548 2012

ORCID

Susan Pyne: 0000-0002-6608-9584

Author Contributions

The manuscript was written through contributions of all authors. All authors have given approval to the final version of the manuscript.

Funding Sources

This research is part funded by the MSD Scottish Life Sciences fund. As part of an on-going contribution to Scottish life sciences, Merck Sharp & Dohme Limited (MSD), a global healthcare leader, has given substantial monetary funding to the Scottish Funding Council (SFC) for distribution via the Scottish Universities Life Science Alliance (SULSA) to develop and deliver a high-quality drug discovery research and training programme. All aspects of the programme have been geared towards attaining the highest value in terms of scientific discovery, training and impact. The opinions expressed in this research are those of the authors and do not represent those of MSD, nor its Affiliates. ST also thanks the Libyan Government for a sponsored PhD studentship.

Notes

The authors declare no competing financial interests.

ABBREVIATIONS

Cer, ceramide; CTD, C-terminal domain; HDAC1/2, histone deacetylases 1/2; LBL, lipid binding loop; NTD, N-terminal domain; R-loop, regulatory loop; S1P, sphingosine 1-phosphate; SK1, sphingosine kinase 1; SK2, sphingosine kinase 2; Sph, sphingosine.

REFERENCES

(1) Garris, C. S.; Blaho, V. A.; Hla, T.; Han, M. H. Sphingosine-1-phosphate receptor 1 signalling in T cells: trafficking and beyond. *Immunology* **2014**, *142*, 347–353.

(2) Hait, N. C.; Allegood, J.; Maceyka, M.; Strub, G. M.; Harikumar, K. B.; Singh, S. K.; Luo, C.; Marmorstein, R.; Kordula, T.; Milstien, S.; Spiegel, S. Regulation of histone acetylation in the nucleus by sphingosine-1-phosphate. *Science* **2009**, *325*, 1254–1257.

(3) Degagne, E.; Pandurangan, A.; Bandhuvula, P.; Kumar, A.; Eltanawy, A.; Zhang, M.; Yoshinaga, Y.; Nefedov, M.; de Jong, P. J.; Fong, L. G.; Young, S. G.; Bittman, R.; Ahmedi, Y.; Saba, J. D. Sphingosine-1-phosphate lyase downregulation promotes colon carcinogenesis through STAT3-activated microRNAs. *J. Clin. Invest.* **2014**, *124*, 5368–5384.

(4) Mandala, S. M.; Thornton, R.; Galve-Roperh, I.; Poulton, S.; Peterson, C.; Olivera, A.; Bergstrom, J.; Kurtz, M. B.; Spiegel, S. Molecular cloning and characterization of a lipid phosphohydrolase that degrades sphingosine-1-phosphate and induces cell death. *Proc. Natl. Acad. Sci. USA* **2000**, *97*, 7859–7864.

(5) Mandala, S. M. Sphingosine-1-phosphate phosphatases. *Prostaglandins* **2001**, *64*, 143–156.

(6) Ogawa, C.; Kihara, A.; Gokoh, M.; Igarashi, Y. Identification and characterization of a novel human sphingosine-1-phosphate phosphohydrolase, hSPP2. *J. Biol. Chem.* **2003**, *278*, 1268–1272.

(7) Siow, D.; Wattenberg, B. The compartmentalization and translocation of the sphingosine kinases: mechanisms and functions in cell signaling and sphingolipid metabolism. *Crit. Rev. Biochem. Mol. Biol.* **2011**, *46*, 365–375.

(8) Hannun, Y. A.; Obeid, L. M. Principles of bioactive lipid signalling: lessons from sphingolipids. *Nat. Rev. Mol. Cell Biol.* **2008**, *9*, 139–150.

(9) Zheng, W.; Kollmeyer, J.; Symolon, H.; Momin, A.; Munter, E.; Wang, E.; Kelly, S.; Allegood, J. C.; Liu, Y.; Peng, Q.; Ramaraju, H.; Sullards, M. C.; Cabot, M.; Merrill, A. H., Jr. Ceramides and other bioactive sphingolipid backbones in health and disease: lipidomic analysis, metabolism and roles in membrane structure, dynamics, signaling and autophagy. *Biochim. Biophys. Acta* **2006**, *1758*, 1864–1884.

(10) Pyne, S.; Chapman, J.; Steele, L.; Pyne, N. J. Sphingomyelin-derived lipids differentially regulate the extracellular signal-regulated kinase 2 (ERK-2) and c-Jun N-terminal kinase (JNK) signal cascades in airway smooth muscle. *Eur. J. Biochem.* **1996**, *237*, 819–826.

(11) Cuvillier, O.; Pirianov, G.; Kleuser, B.; Vanek, P. G.; Coso, O. A.; Gutkind, S.; Spiegel, S. Suppression of ceramide-mediated programmed cell death by sphingosine-1-phosphate. *Nature* **1996**, *381*, 800–803.

(12) Newton, J.; Lima, S.; Maceyka, M.; Spiegel, S. Revisiting the sphingolipid rheostat: Evolving concepts in cancer therapy. *Exp. Cell Res.* **2015**, *333*, 195–200.

(13) Pyne, S.; Adams, D. R.; Pyne, N. J. Sphingosine kinases as druggable targets. In *Handb. Exp. Pharmacol.*, Springer, Berlin, Heidelberg: 2018.

(14) Pyne, S.; Adams, D. R.; Pyne, N. J. Sphingosine 1-phosphate and sphingosine kinases in health and disease: recent advances. *Prog. Lipid Res.* **2016**, *62*, 93–106.

(15) Neubauer, H. A.; Pitson, S. M. Roles, regulation and inhibitors of sphingosine kinase 2. *FEBS J.* **2013**, *280*, 5317–5336.

(16) Baker, D. L.; Pham, T. C.; Sparks, M. A. Structure and catalytic function of sphingosine kinases: analysis by site-directed mutagenesis and enzyme kinetics. *Biochim. Biophys. Acta* **2013**, *1831*, 139–146.

(17) Pitman, M. R.; Powell, J. A.; Coolen, C.; Moretti, P. A.; Zebol, J. R.; Pham, D. H.; Finnie, J. W.; Don, A. S.; Ebert, L. M.; Bonder, C. S.; Gliddon, B. L.; Pitson, S. M. A selective ATP-competitive sphingosine kinase inhibitor demonstrates anti-cancer properties. *Oncotarget* **2015**, *6*, 7065–7083.

(18) Schnute, M. E.; McReynolds, M. D.; Kasten, T.; Yates, M.; Jerome, G.; Rains, J. W.; Hall, T.; Chrencik, J.; Kraus, M.; Cronin, C. N.; Saabye, M.; Highkin, M. K.; Broadus, R.; Ogawa, S.; Cukyne, K.; Zawadzke, L. E.; Peterkin, V.; Iyanar, K.; Scholten, J. A.; Wendling, J.; Fujiwara, H.; Nemirovskiy, O.; Wittwer, A. J.; Nagiec, M. M. Modulation of cellular S1P levels with a novel, potent and specific inhibitor of sphingosine kinase-1. *Biochem. J.* **2012**, *444*, 79–88.

(19) Xiang, Y.; Hirth, B.; Kane, J. L., Jr.; Liao, J.; Noson, K. D.; Yee, C.; Asmussen, G.; Fitzgerald, M.; Klaus, C.; Booker, M. Discovery of novel sphingosine kinase-1 inhibitors. Part 2. *Bioorg. Med. Chem. Lett.* **2010**, *20*, 4550–4554.

(20) Gustin, D. J.; Li, Y.; Brown, M. L.; Min, X.; Schmitt, M. J.; Wanska, M.; Wang, X.; Connors, R.; Johnstone, S.; Cardozo, M.; Cheng, A. C.; Jeffries, S.; Franks, B.; Li, S.; Shen, S.; Wong, M.; Wesche, H.; Xu, G.; Carlson, T. J.; Plant, M.; Morgenstern, K.; Rex, K.; Schmitt, J.; Coxon, A.; Walker, N.; Kayser, F.; Wang, Z. Structure guided design of a series of sphingosine kinase (SphK) inhibitors. *Bioorg. Med. Chem. Lett.* **2013**, *23*, 4608–4616.

(21) Zhang, Y.; Berka, V.; Song, A.; Sun, K.; Wang, W.; Zhang, W.; Ning, C.; Li, C.; Zhang, Q.; Bogdanov, M.; Alexander, D. C.; Milburn, M. V.; Ahmed, M. H.; Lin, H.; Idowu, M.; Zhang, J.; Kato, G. J.; Abdulmalik, O. Y.; Zhang, W.; Dowhan, W.; Kellems, R. E.; Zhang, P.; Jin, J.; Safo, M.; Tsai, A. L.; Juneja, H. S.; Xia, Y. Elevated sphingosine-1-phosphate promotes sickling and sickle cell disease progression. *J. Clin. Invest.* **2014**, *124*, 2750–2761.

(22) Zhang, F.; Xia, Y.; Yan, W.; Zhang, H.; Zhou, F.; Zhao, S.; Wang, W.; Zhu, D.; Xin, C.; Lee, Y.; Zhang, L.; He, Y.; Gao, E.; Tao, L. Sphingosine 1-phosphate signaling contributes to cardiac inflammation, dysfunction, and remodeling following myocardial infarction. *Am. J. Physiol. Heart Circ. Physiol.* **2016**, *310*, H250–H261.

(23) MacRitchie, N.; Volpert, G.; Al Washih, M.; Watson, D. G.; Futerman, A. H.; Kennedy, S.; Pyne, S.; Pyne, N. J. Effect of the sphingosine kinase 1 selective inhibitor, PF-543 on arterial and cardiac remodelling in a hypoxic model of pulmonary arterial hypertension. *Cell. Signal.* **2016**, *28*, 946–955.

(24) French, K. J.; Zhuang, Y.; Maines, L. W.; Gao, P.; Wang, W.; Beljanski, V.; Upson, J. J.; Green, C. L.; Keller, S. N.; Smith, C. D. Pharmacology and antitumor activity of ABC294640, a selective inhibitor of sphingosine kinase-2. *J. Pharmacol. Exp. Ther.* **2010**, *333*, 129–139.

(25) Liu, K.; Guo, T. L.; Hait, N. C.; Allegood, J.; Parikh, H. I.; Xu, W.; Kellogg, G. E.; Grant, S.; Spiegel, S.; Zhang, S. Biological characterization of 3-(2-aminoethyl)-5-[3-(4-butoxylphenyl)propylidene]thiazolidine-2,4-dione (K145) as a selective sphingosine kinase-2 inhibitor and anticancer agent. *PLoS One* **2013**, *8*, e56471.

(26) Kharel, Y.; Raje, M.; Gao, M.; Gellett, A. M.; Tomsig, J. L.; Lynch, K. R.; Santos, W. L. Sphingosine kinase type 2 inhibition elevates circulating sphingosine 1-phosphate. *Biochem. J.* **2012**, *447*, 149–157.

(27) Lim, K. G.; Sun, C.; Bittman, R.; Pyne, N. J.; Pyne, S. (*R*)-FTY720 methyl ether is a specific sphingosine kinase 2 inhibitor: effect on sphingosine kinase 2 expression in HEK 293 cells and actin rearrangement and survival of MCF-7 breast cancer cells. *Cell. Signal.* **2011**, *23*, 1590–1595.

(28) Beljanski, V.; Knaak, C.; Smith, C. D. A novel sphingosine kinase inhibitor induces autophagy in tumor cells. *J. Pharmacol. Exp. Ther.* **2010**, *333*, 454–464.

(29) Fitzpatrick, L. R.; Green, C.; Frauenhoffer, E. E.; French, K. J.; Zhuang, Y.; Maines, L. W.; Upson, J. J.; Paul, E.; Donahue, H.; Mosher, T. J.; Smith, C. D. Attenuation of arthritis in rodents by a novel orally-available inhibitor of sphingosine kinase. *Inflammopharmacology* **2011**, *19*, 75–87.

(30) Maines, L. W.; Fitzpatrick, L. R.; Green, C. L.; Zhuang, Y.; Smith, C. D. Efficacy of a novel sphingosine kinase inhibitor in experimental Crohn's disease. *Inflammopharmacology* **2010**, *18*, 73–85.

(31) Venant, H.; Rahmaniyan, M.; Jones, E. E.; Lu, P.; Lilly, M. B.; Garrett-Mayer, E.; Drake, R. R.; Kraveka, J. M.; Smith, C. D.; Voelkel-Johnson, C. The sphingosine kinase 2 inhibitor ABC294640 reduces the growth of prostate cancer cells and results in accumulation of dihydroceramides *in vitro* and *in vivo*. *Mol. Cancer Ther.* **2015**, *14*, 2744–2752.

(32) McNaughton, M.; Pitman, M.; Pitson, S. M.; Pyne, N. J.; Pyne, S. Proteasomal degradation of sphingosine kinase 1 and inhibition of dihydroceramide desaturase by the sphingosine kinase inhibitors, SKi or ABC294640, induces growth arrest in androgen-independent LNCaP-AI prostate cancer cells. *Oncotarget* **2016**, *7*, 16663–16675.

(33) Alsanafi, M.; Kelly, S. L.; Jubair, K.; McNaughton, M.; Tate, R. J.; Merrill, A. H., Jr.; Pyne, S.; Pyne, N. J. Native and polyubiquitinated forms of dihydroceramide desaturase are

differentially linked to human embryonic kidney cell survival. *Mol. Cell. Biol.* **2018**, *38*, e00222-18.

(34) Evangelisti, C.; Evangelisti, C.; Teti, G.; Chiarini, F.; Falconi, M.; Melchionda, F.; Pession, A.; Bertaina, A.; Locatelli, F.; McCubrey, J. A.; Beak, D. J.; Bittman, R.; Pyne, S.; Pyne, N. J.; Martelli, A. M. Assessment of the effect of sphingosine kinase inhibitors on apoptosis, unfolded protein response and autophagy of T-cell acute lymphoblastic leukemia cells; indications for novel therapeutics. *Oncotarget* **2014**, *5*, 7886–7901.

(35) Schnute, M. E.; McReynolds, M. D.; Carroll, J.; Chrencik, J. E.; Highkin, M. K.; Iyanar, K.; Jerome, G.; Rains, J. W.; Saabye, M.; Scholten, J. A.; Yates, M.; Nagiec, M. M. Discovery of a potent and selective sphingosine kinase 1 inhibitor through the molecular combination of chemotype distinct screening hits. *J. Med. Chem.* **2017**, *60*, 2562–2572.

(36) Childress, E. S.; Kharel, Y.; Brown, A. M.; Bevan, D. R.; Lynch, K. R.; Santos, W. L. Transforming sphingosine kinase 1 inhibitors into dual and sphingosine kinase 2 selective inhibitors: design, synthesis, and *in vivo* activity. *J. Med. Chem.* **2017**, *60*, 3933–3957.

(37) Wang, Z.; Min, X.; Xiao, S. H.; Johnstone, S.; Romanow, W.; Meininger, D.; Xu, H.; Liu, J.; Dai, J.; An, S.; Thibault, S.; Walker, N. Molecular basis of sphingosine kinase 1 substrate recognition and catalysis. *Structure* **2013**, *21*, 798–809.

(38) Wang, J.; Knapp, S.; Pyne, N. J.; Pyne, S.; Elkins, J. M. Crystal Structure of sphingosine kinase 1 with PF-543. *ACS Med. Chem. Lett.* **2014**, *5*, 1329–1333.

(39) Adams, D. R.; Pyne, S.; Pyne, N. J. Sphingosine kinases: emerging structure-function insights. *Trends Biochem. Sci.* **2016**, *41*, 395–409.

(40) Cinelli, M. A.; Li, H.; Pensa, A. V.; Kang, S.; Roman, L. J.; Martasek, P.; Poulos, T. L.; Silverman, R. B. Phenyl ether- and aniline-containing 2-aminoquinolines as potent and selective inhibitors of neuronal nitric oxide synthase. *J. Med. Chem.* **2015**, *58*, 8694–8712.

(41) Byun, H.-S.; Pyne, S.; MacRitchie, N.; Pyne, N. J.; Bittman, R. Novel sphingosine-containing analogues selectively inhibit sphingosine kinase (SK) isozymes, induce SK1 proteasomal degradation and reduce DNA synthesis in human pulmonary arterial smooth muscle cells. *MedChemComm* **2013**, *4*, 1394–1399.

(42) Edsall, L. C.; Van Brocklyn, J. R.; Cuvillier, O.; Kleuser, B.; Spiegel, S. N,N-Dimethylsphingosine is a potent competitive inhibitor of sphingosine kinase but not of protein kinase C: modulation of cellular levels of sphingosine 1-phosphate and ceramide. *Biochemistry* **1998**, *37*, 12892–12898.

(43) Hengst, J. A.; Guilford, J. M.; Conroy, E. J.; Wang, X.; Yun, J. K. Enhancement of sphingosine kinase 1 catalytic activity by deletion of 21 amino acids from the COOH-terminus. *Arch. Biochem. Biophys.* **2010**, *494*, 23–31.

(44) Lim, K. G.; Tonelli, F.; Li, Z.; Lu, X.; Bittman, R.; Pyne, S.; Pyne, N. J. FTY720 analogues as sphingosine kinase 1 inhibitors: enzyme inhibition kinetics, allosterism, proteasomal degradation, and actin rearrangement in MCF-7 breast cancer cells. *J. Biol. Chem.* **2011**, *286*, 18633–18640.

(45) Jones, L. H.; Summerhill, N. W.; Swain, N. A.; Mills, J. E. Aromatic chloride to nitrile transformation: medicinal and synthetic chemistry. *Med. Chem. Commun.* **2010**, *1*, 309–318.

(46) Fleming, F. F.; Yao, L.; Ravikumar, P. C.; Funk, L.; Shook, B. C. Nitrile-containing pharmaceuticals: efficacious roles of the nitrile pharmacophore. *J. Med. Chem.* **2010**, *53*, 7902–7917.

(47) Arnold, K.; Bordoli, L.; Kopp, J.; Schwede, T. The SWISS-MODEL workspace: a web-based environment for protein structure homology modelling. *Bioinformatics* **2006**, *22*, 195–201.

(48) Kiefer, F.; Arnold, K.; Kunzli, M.; Bordoli, L.; Schwede, T. The SWISS-MODEL Repository and associated resources. *Nucleic Acids Res.* **2009**, *37*, D387–D392.

(49) Guex, N.; Peitsch, M. C.; Schwede, T. Automated comparative protein structure modeling with SWISS-MODEL and Swiss-PdbViewer: a historical perspective. *Electrophoresis* **2009**, *30 Suppl 1*, S162–S173.

(50) Biasini, M.; Bienert, S.; Waterhouse, A.; Arnold, K.; Studer, G.; Schmidt, T.; Kiefer, F.; Gallo Cassarino, T.; Bertoni, M.; Bordoli, L.; Schwede, T. SWISS-MODEL: modelling protein tertiary and quaternary structure using evolutionary information. *Nucleic Acids Res.* **2014**, *42*, W252–W258.

(51) Congdon, M. D.; Kharel, Y.; Brown, A. M.; Lewis, S. N.; Bevan, D. R.; Lynch, K. R.; Santos, W. L. Structure-activity relationship studies and molecular modeling of naphthalene-based sphingosine kinase 2 Inhibitors. *ACS Med. Chem. Lett.* **2016**, *7*, 229–234.

(52) Houck, J. D.; Dawson, T. K.; Kennedy, A. J.; Kharel, Y.; Naimon, N. D.; Field, S. D.; Lynch, K. R.; Macdonald, T. L. Structural requirements and docking analysis of amidine-based sphingosine kinase 1 inhibitors containing oxadiazoles. *ACS Med. Chem. Lett.* **2016**, *7*, 487–492.

(53) Fang, L.; Wang, X.; Xi, M.; Liu, T.; Yin, D. Assessing the ligand selectivity of sphingosine kinases using molecular dynamics and MM-PBSA binding free energy calculations. *Mol. Biosyst.* **2016**, *12*, 1174–1182.

(54) Gottlieb, H. E.; Kotlyar, V.; Nudelman, A. NMR chemical shifts of common laboratory solvents as trace impurities. *J. Org. Chem.* **1997**, *62*, 7512–7515.

(55) Bishop, J. E.; Mathis, C. A.; Gerdes, J. M.; Whitney, J. M.; Eaton, A. M.; Mailman, R. B. Synthesis and in vitro evaluation of 2,3-dimethoxy-5-(fluoroalkyl)-substituted benzamides: high-affinity ligands for CNS dopamine D2 receptors. *J. Med. Chem.* **1991**, *34*, 1612–1624.

(56) Bakali, H. M.; Herman, M. D.; Johnson, K. A.; Kelly, A. A.; Wieslander, A.; Hallberg, B. M.; Nordlund, P. Crystal structure of YegS, a homologue to the mammalian diacylglycerol kinases, reveals a novel regulatory metal binding site. *J. Biol. Chem.* **2007**, *282*, 19644–19652.

(57) Abe, T.; Lu, X.; Jiang, Y.; Boccone, C. E.; Qian, S.; Vattem, K. M.; Wek, R. C.; Walsh, J. P. Site-directed mutagenesis of the active site of diacylglycerol kinase alpha: calcium and phosphatidylserine stimulate enzyme activity via distinct mechanisms. *Biochem. J.* **2003**, *375*, 673–680.

Table of Contents graphic

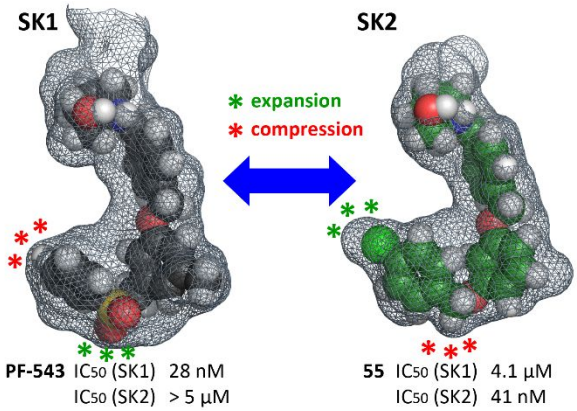

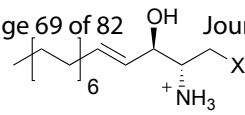

		K_i (IC_{50}) / nM [a]	
		SK1	SK2
SK1-selective inhibitors			
1 PF-543 [d]	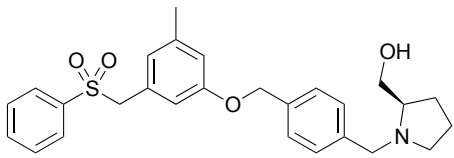	(28) [b]	(>5,000) [b]
2 Genzyme-51	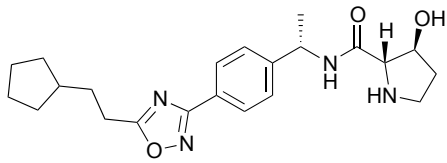	(58)	ND [c]
3 Amgen-23 [d]	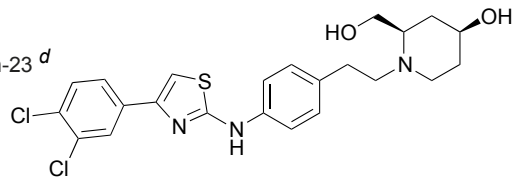	(20)	(1,600)
SK2-selective inhibitors			
4 ABC294640	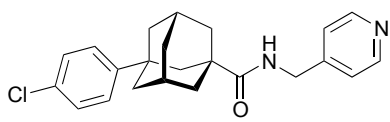	no inhibition at 100 μM	9,800
5 K145	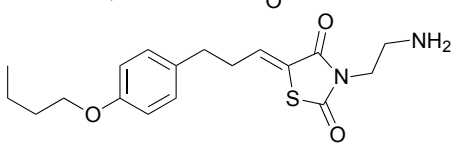	no inhibition at 10 μM	6,400
6 SLR080811	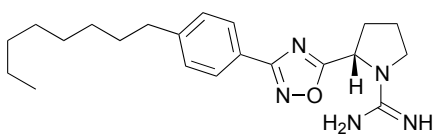	12,000	1,300
7 ROMe	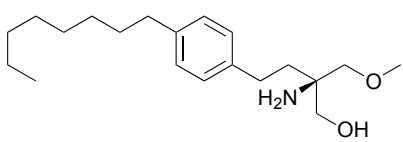	no inhibition at 100 μM	16,000
8 Pfizer-27c	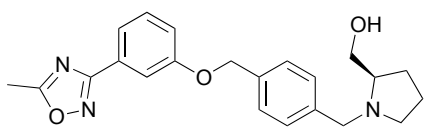	(25)	(2.4)
9 VT-20dd	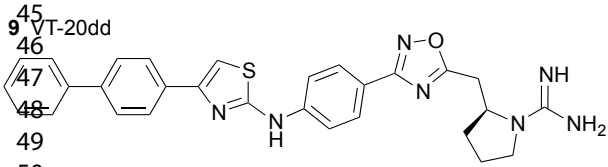	9,000	90
Other inhibitors			
10 SKi [d]	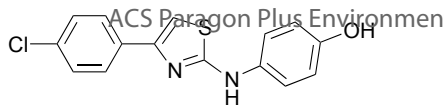	16,000	6,700

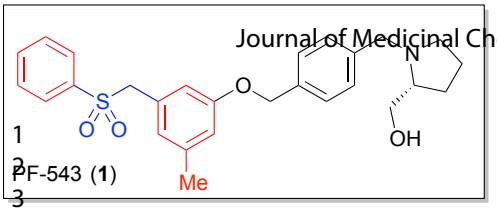

methyl deletion

			SK1 IC_{50}/nM	SK2 IC_{50}/nM	SI
PF-543 (**1**)			28	(33%)*	
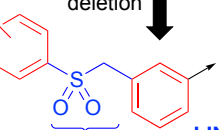 sulfonylmethylene **LINKER TYPE**	**18**	X = H	144	(16%)†	<0.048
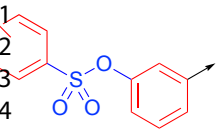 sulfonate	**19**	X = H	11	902	0.012
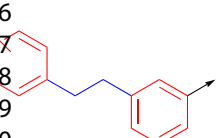 ethylene	**23**	X = H	26	35	0.74
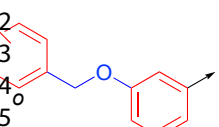 methyleneoxy	**49**	X = H	14	16	0.88
	50	X = *o*-F	41	55	0.75
	51	X = *m*-F	9	143	0.063
	52	X = *p*-F	170	49	3.5
	53	X = *o*-Cl	39	151	0.26
	54	X = *m*-Cl	44	412	0.11
	55	X = *p*-Cl	4,130‡	41	101
	56	X = *p*-OMe	>3,000	119	>25
	57	X = *p*-CN	>3,000	1,120‡	>2.7
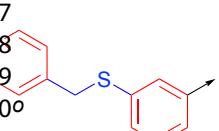 methylenesulfanyl	**58**	X = H	137	26	5.3
	59	X = *p*-F	765	17	45
	60	X = *p*-Cl	2,360‡	31	76

*% enzyme inhibition at 5 μM test concentration

†% enzyme inhibition at 3 μM test concentration

‡Estimated IC_{50} from partial concentration response curve (1 nM – 3 μM range)

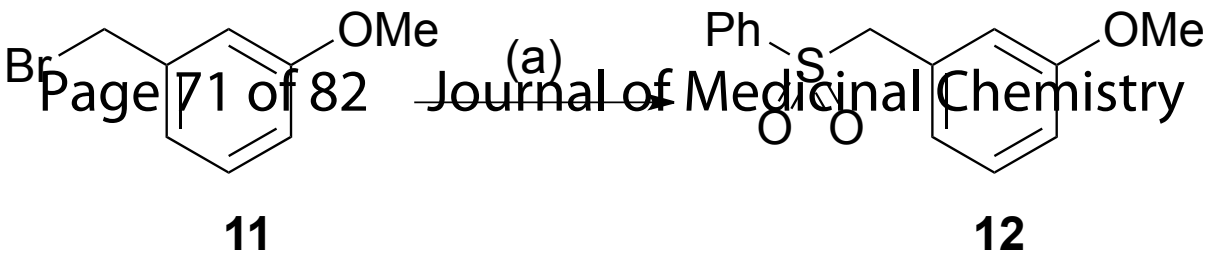

11 **12**

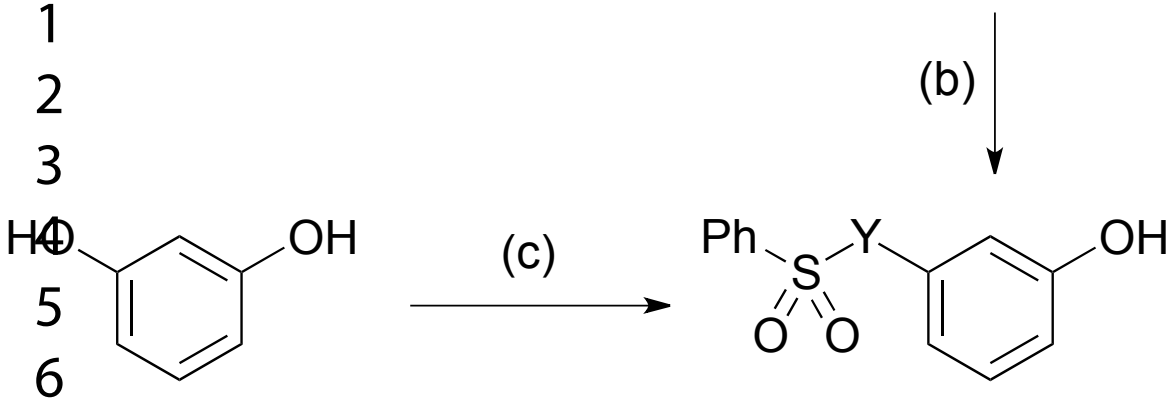

13

14 Y = CH_2 (77% from **12**)
15 Y = O (21% from **13**)

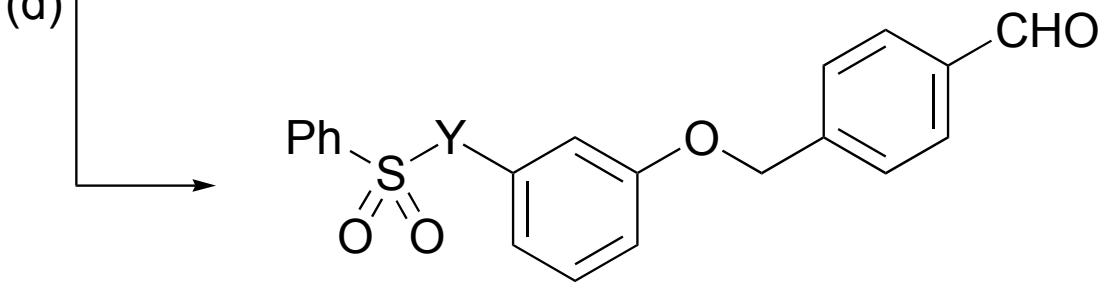

16 Y = CH_2 (81% from **14**)
17 Y = O (88% from **15**)

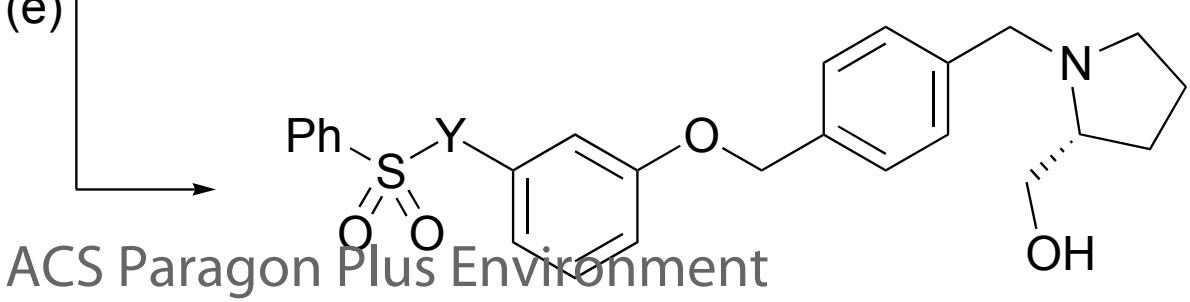

18 Y = CH_2 (71% from **16**)
19 Y = O (33% from **17**)

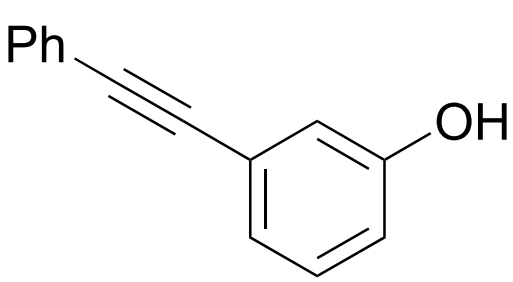

20

(a)

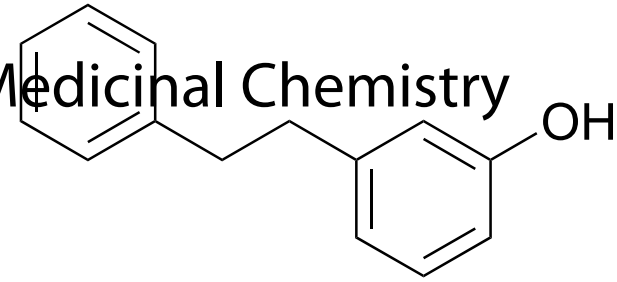

21

(b)

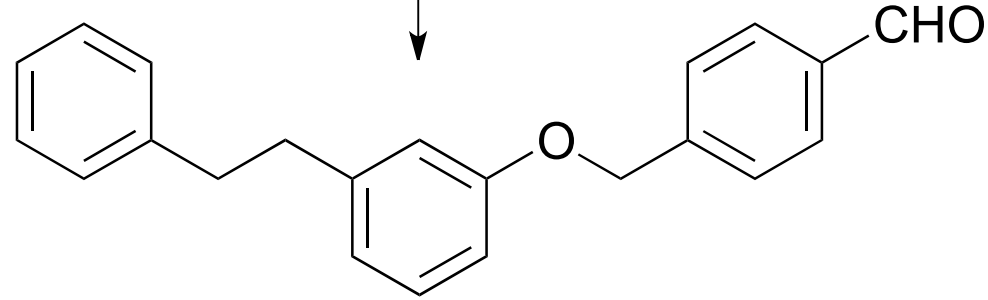

22

(c)

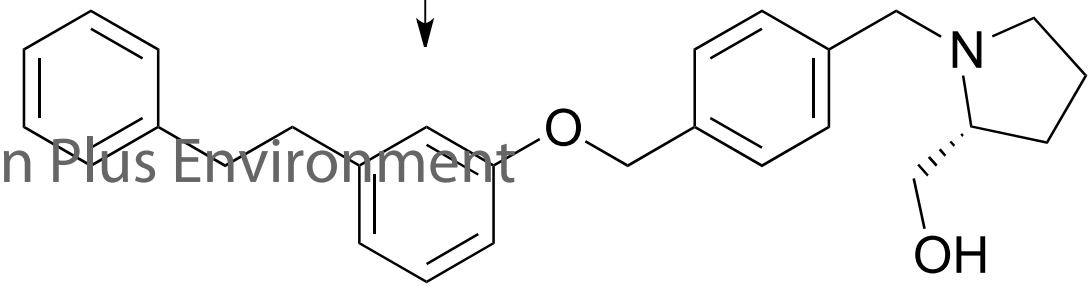

23

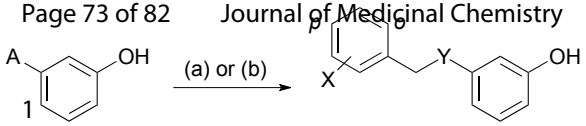

43 A = OH
44 A = SH

25	Y = O	X = H	(55% from **13**)
26	Y = O	X = *o*-F	(53% from **13**)
27	Y = O	X = *m*-F	(58% from **13**)
28	Y = O	X = *p*-F	(38% from **13**)
29	Y = O	X = *o*-Cl	(54% from **13**)
30	Y = O	X = *m*-Cl	(49% from **13**)
31	Y = O	X = *p*-Cl	(48% from **13**)
32	Y = O	X = *p*-OMe	(32% from **13**)
33	Y = O	X = *p*-CN	(47% from **13**)
34	Y = S	X = H	(68% from **24**)
35	Y = S	X = *p*-F	(71% from **24**)
36	Y = S	X = *p*-Cl	(79% from **24**)

(c) or (d)

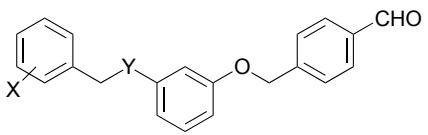

37	Y = O	X = H	(88% from **25**)
38	Y = O	X = *o*-F	(62% from **26**)
39	Y = O	X = *m*-F	(64% from **27**)
40	Y = O	X = *p*-F	(77% from **28**)
41	Y = O	X = *o*-Cl	(71% from **29**)
42	Y = O	X = *m*-Cl	(55% from **30**)
43	Y = O	X = *p*-Cl	(96% from **31**)
44	Y = O	X = *p*-OMe	(68% from **32**)
45	Y = O	X = *p*-CN	(95% from **33**)
46	Y = S	X = H	(79% from **34**)
47	Y = S	X = *p*-F	(93% from **35**)
48	Y = S	X = *p*-Cl	(84% from **36**)

(e)

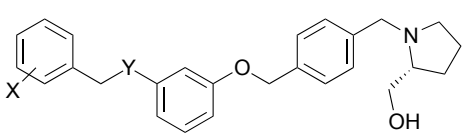

49	Y = O	X = H	(70% from **37**)
50	Y = O	X = *o*-F	(69% from **38**)
51	Y = O	X = *m*-F	(57% from **39**)
52	Y = O	X = *p*-F	(73% from **40**)
53	Y = O	X = *o*-Cl	(58% from **41**)
54	Y = O	X = *m*-Cl	(50% from **42**)
55	Y = O	X = *p*-Cl	(86% from **43**)
56	Y = O	X = *p*-OMe	(84% from **44**)
57	Y = O	X = *p*-CN	(38% from **45**)
58	Y = S	X = H	(95% from **46**)
59	Y = S	X = *p*-F	(78% from **47**)
60	Y = S	X = *p*-Cl	(53% from **48**)

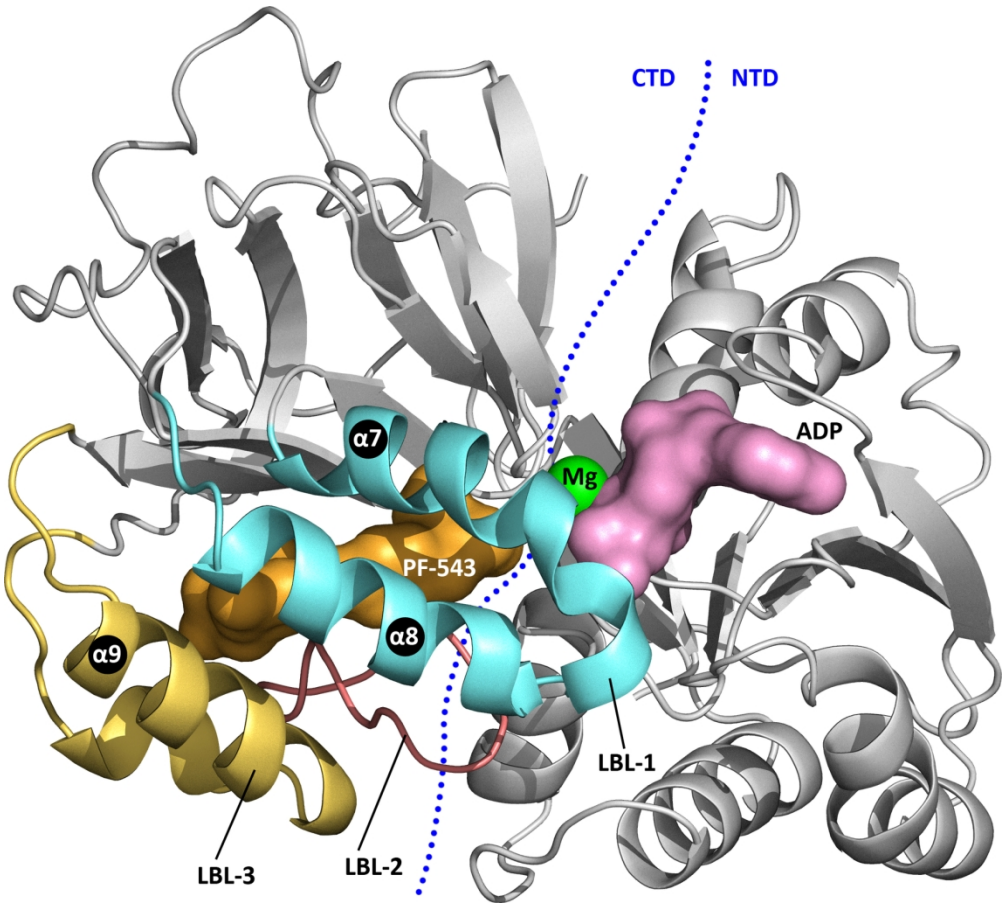

Figure 1. The structure of SK1 is shown with bound PF-543 (1; orange surface) (PDB: 4V24). PF-543 occupies the substrate Sph binding site, formed by the packing of three lipid binding loops (LBL-1 to LBL-3) against a β-sandwich core. The nucleotide binding site is shown by superimposition of Mg-ADP (green sphere/rose surface) from its separate co-crystal structure (3VZD) with SK1.

80x71mm (600 x 600 DPI)

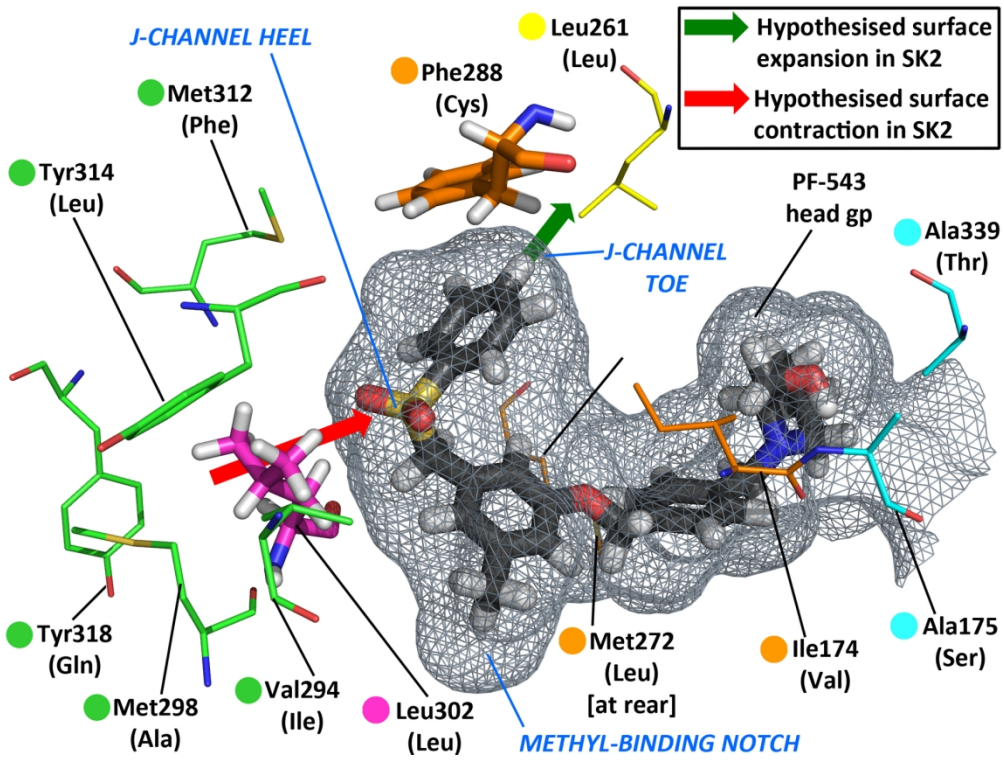

Figure 2. J-channel surface detail (mesh) from the PF-543/SK1 co-crystal (PDB: 4V24), highlighting key isoform residue differences that likely impact on the J-channel struc-ture of SK2. SK1 residue numbering is shown; cognate SK2 residues, where different, are in parenthesis. (Residue color notation: see text.)

79x59mm (600 x 600 DPI)

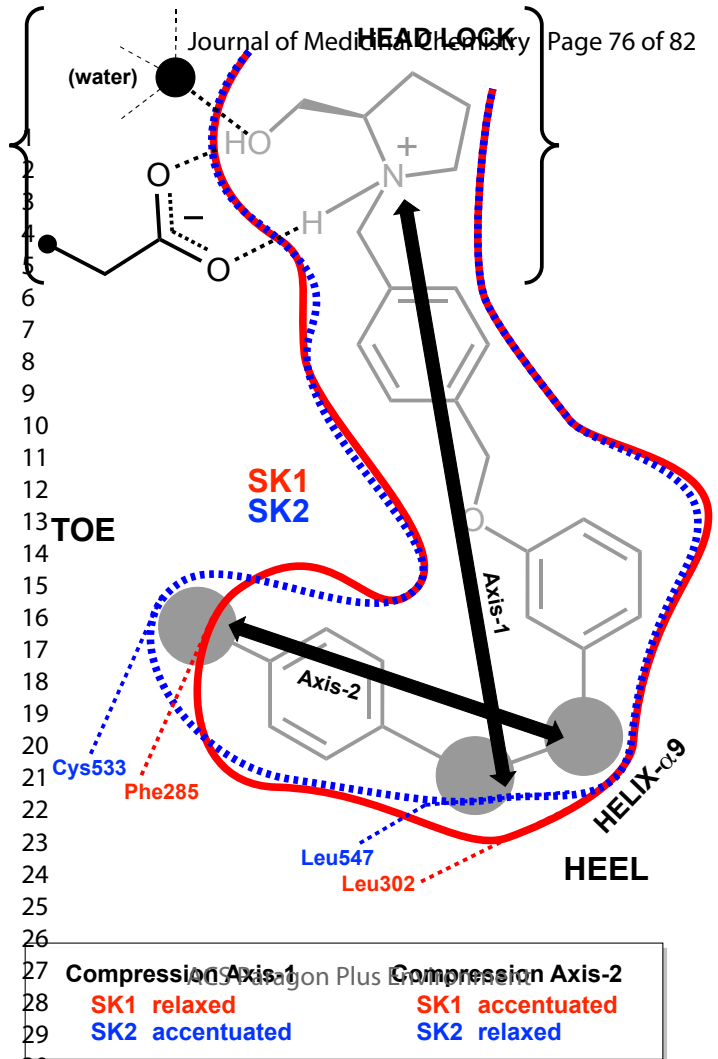

SK1-selective inhibition

equipotent SK1/SK2 inhibition

SK2-selective inhibition

compression along 'Axis-1' (Figure 3)

compression along 'Axis-2' (Figure 3)

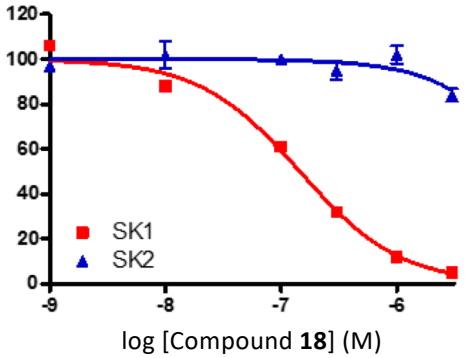

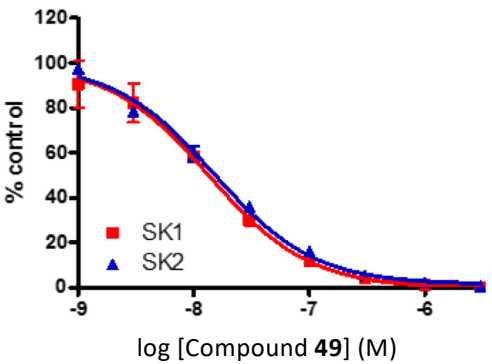

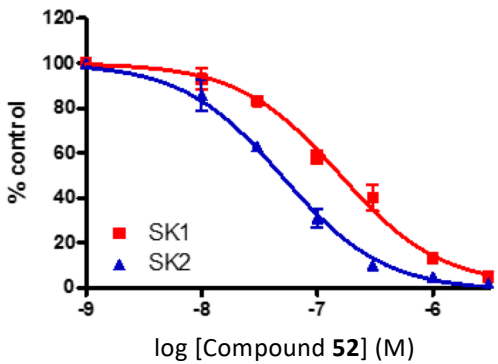

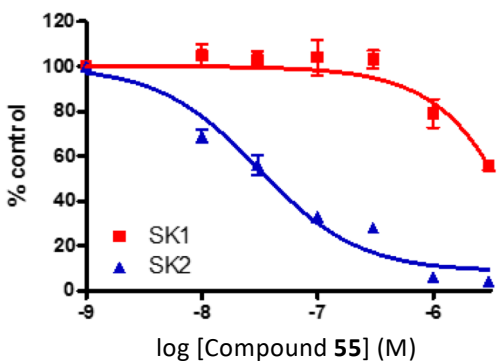

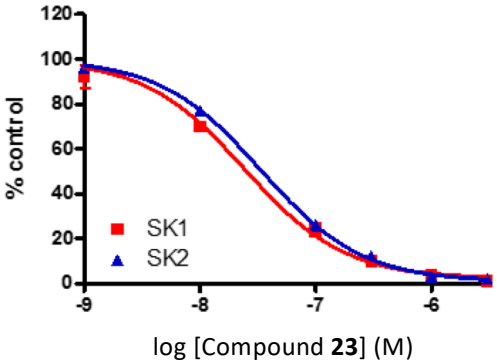

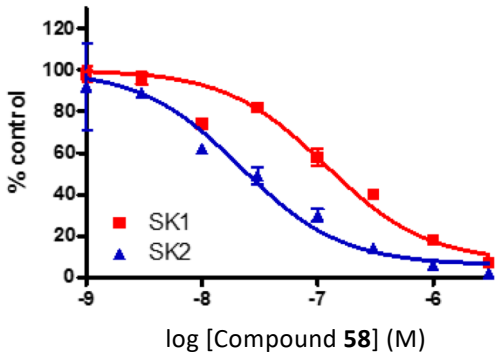

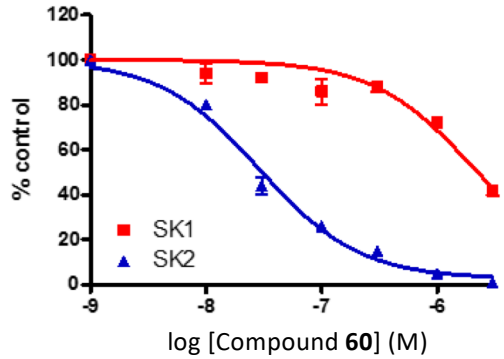

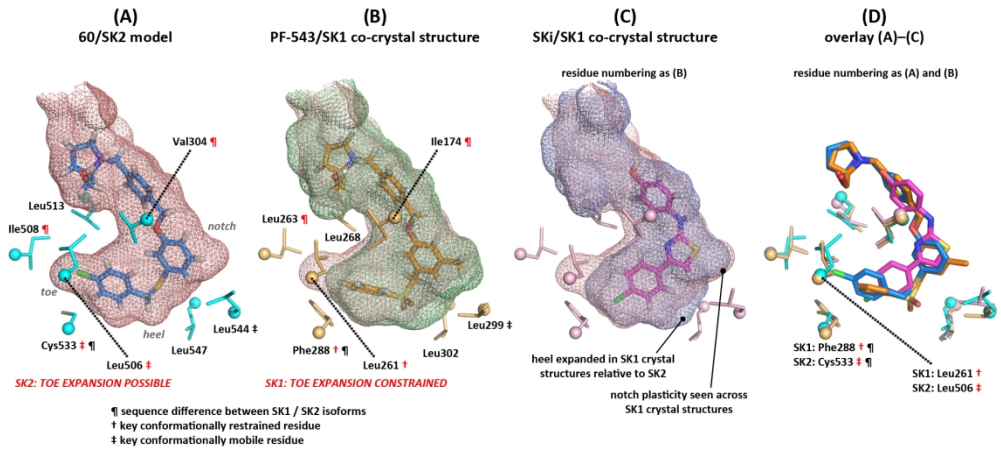

Figure 5. Comparison of modelled binding mode for SK2-selective inhibitor 60 with SK1 co-crystal structures of PF-543 (1) and SKi (10). Panel (A): 60 (blue stick) docked into SK2 model (red mesh), highlighting key contact residues (cyan stick) and ex-panded SK2 J-channel toe surface. Panel (B): PF-543 (1; orange stick) is shown from its co-crystal structure (4V24) with SK1 (green mesh) and the SK2 model surface (red mesh) overlaid from (A); SK1 contact residues are shown (light orange stick) and the constrained SK1 J-channel toe surface is evident. Panel (C): As (B), but showing co-crystal structure (3VZD) of SKi (10, magenta stick) with SK1 (blue mesh and pink stick key contact residues) superimposed onto the SK2 model (red mesh) from panel (A); the heel region adjacent to SK1 Leu302 is consistently less compressed in SK1 structures (relative to the SK2 model), whilst the notch surface exhibits some plasticity. Panel (D): overlay of (A)–(C) minus the J-channel surface; the chlorine atom of 60 is ac-commodated in SK2 between Cys588 and Leu506, with rotation of the latter possible whilst the cognate SK1 residue (Leu261) is constrained by the packing of adjacent residues.

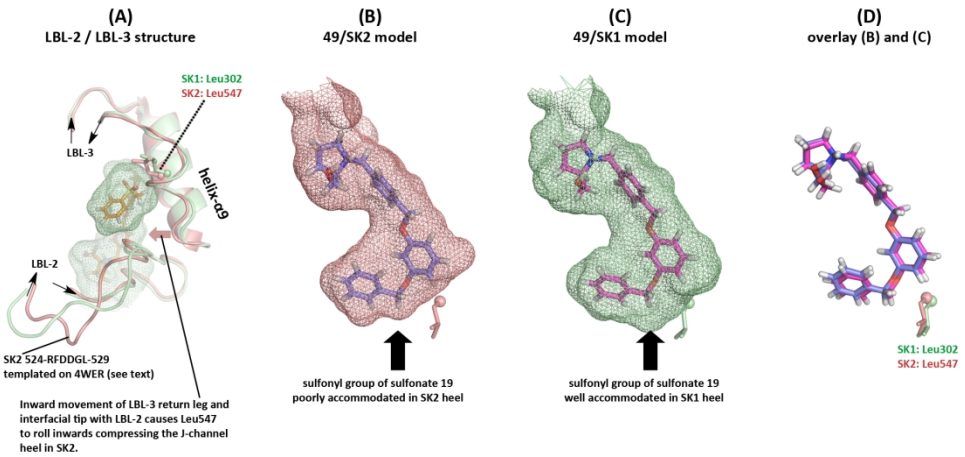

Figure 6. The J-channel heel is a key determinant of isoform discrimination by SK inhibitors. Panel (A): LBL-2 and LBL-3 are shown from the co-crystal structure (4V24) of PF-543 (orange stick) with SK1 (green ribbon); the corresponding elements from our SK2 homology model (red ribbon) are overlaid, illustrating inward movement in LBL-3 leading to heel compression in SK2 by Leu547. Panel (B): Potent unselective inhibitor 49 (blue stick) is shown modelled into the SK2 J-channel (red mesh); the J-channel heel surface is driven significantly inwards relative to SK1 so that the presence of a sulfonyl group in the ligand (49 --> 19, 56-fold activity loss) is poorly tolerated by SK2. Panel (C): Inhibitor 49 (magenta stick) is again shown, here modelled into the SK1 J-channel (green mesh); the SK1 J-channel heel surface exhibits less compression and accommodates a sterically more demanding sulfonyl containing linker more readily (49 --> 19, no activity loss; 23 --> 18, 5-fold activity loss). Panel (D): overlay of (B) and (C) minus the J-channel surface.

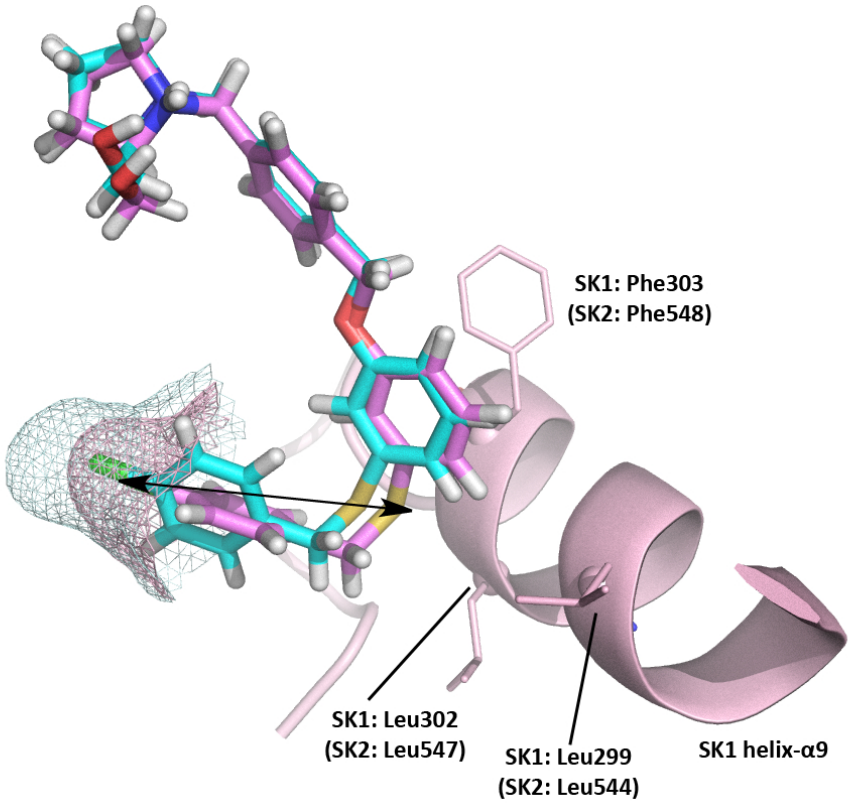

Figure 7. The J-channel toe is a second key determinant for isoform discrimination by SK inhibitors. A comparison of modelled binding modes for the SK2-selective inhibitor (60) is shown here, with the SK2-docked inhibitor (cyan stick) superimposed onto the SK1-docked inhibitor (magenta stick). With reduced plasticity in the SK1 J-channel toe (pink mesh), the sulfur atom of 60 is predicted to be tightly wedged against the backbone of helix-α9 (pink ribbon). This generates an unfavourable compression axis (black arrow, corresponding to 'Axis-2' of Figure 3) that preferentially penalizes binding to SK1. In SK2 the greater plasticity of the J-channel toe (cyan mesh) is predicted to allow accommodation of 60 with less compression.

84x69mm (299 x 299 DPI)

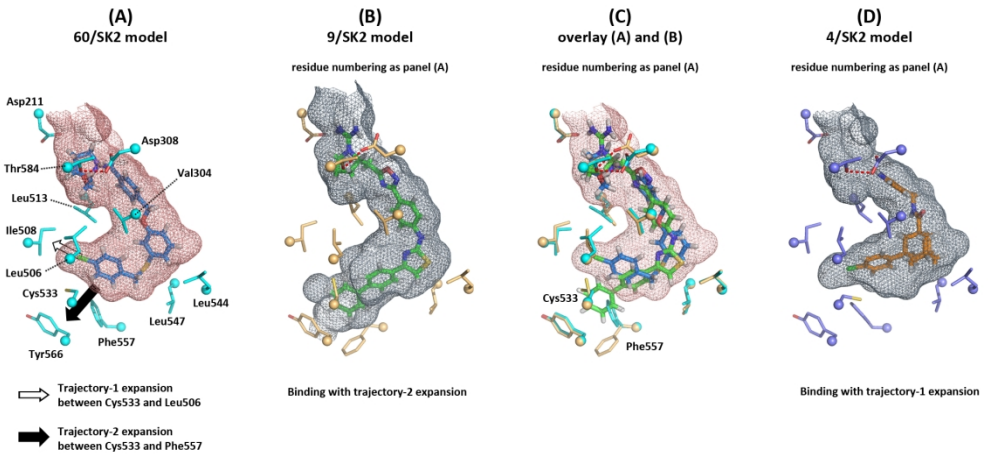

Figure 8. Plasticity in the J-channel toe of SK2 may be exploited to develop SK2-selective inhibitors. Panel (A): Compound 60 (blue stick) docked into the SK2 model (red mesh), highlighting key contact residues (cyan stick) and two predicted trajectories for possible toe expansion (arrows). Small groups may be accommodated between Cys533 and Leu506 (Trajectory-1, hollow ar-row). This is the predicted expansion for binding of 55/60, where the fit of the Cl atom is likely made possible largely by rotation in Leu506. Larger groups may be accommodated between Cys533 and Phe557 (Trajectory-2, filled arrow) upon rotation of these side chains. Panel (B): VT-20dd (9, green stick) docked into the SK2 model (grey mesh), highlighting key contact residues (orange stick). Here the ligand is predicted to exploit the second toe expansion trajectory. Panel (C): Overlay of (A) and (B) showing the SK2 J-channel surface for docked 60 (red mesh) and illustrating the two key residue rotations in Cys533 and Phe557 required for Trajectory-2 expansion (cyan stick --> orange stick positions). Panel (D): ABC294640 (4, orange stick) docked into SK2 (grey mesh). In this model, the Trajectory-1 expansion is made possible chiefly by rotation of Cys533 rather than Leu506, but the space generated by the expansion is underused by the Cl atom.

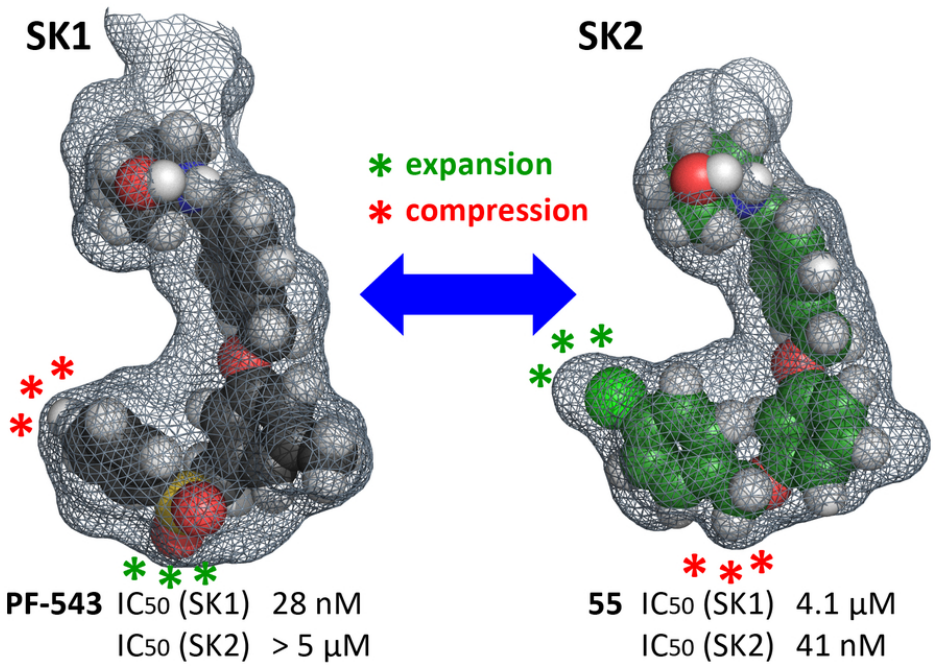

Table of Contents graphic

81x53mm (300 x 300 DPI)